Intruder states and shape coexistence beyond N=50 close to 78Ni studied by neutron knockout at RIBF-RIKEN

Léo Plagnol

Normandie Université

UNIVERSITÉ CAEN NORMANDIE

THÈSE

Pour obtenir le diplôme de doctorat

Spécialité **PHYSIQUE**

Préparée au sein de l'**Université de Caen Normandie**

Intruder states and shape coexistence beyond N=50 close to 78Ni studied by neutron knockout at RIBF-RIKEN

Présentée et soutenue par

LEO PLAGNOL

Thèse soutenue le 23/11/2023

devant le jury composé de :

M. RICCARDO RAABE	Professeur - LEUVEN - KATHOLIEKE UNIVERSITEIT	Rapporteur du jury
MME MAGDA ZIELINSKA	Ingénieur de recherche - CEA Paris-Saclay	Rapporteur du jury
M. WILTON CATFORD	Professeur - Université de Surrey	Membre du jury
MME IOLANDA MATTEA	Maître de conférences - Université Paris Saclay	Membre du jury
M. ETIENNE LIENARD	Professeur des universités - Université de Caen Normandie	Président du jury
M. JULIEN GIBELIN	Maître de conférences - Université de Caen Normandie	Directeur de thèse

Thèse dirigée par **JULIEN GIBELIN** (Laboratoire de physique corpusculaire (Caen))

ED 591 PSIME

lpc caen
laboratoire de physique corpusculaire

Remerciements

C'est après trois ans de navigation sur les mers houleuses du travail de thèse qu'on arrive à bon port. Comment le navire n'a-t-il pas coulé ? Un capitaine malhonnête simplifierait "*complications arose, ensued, were overcome*" [1]. Mais en réalité il y a tout un équipage sur ce bateau, et si la coque n'arrive pas abîmée, c'est bien grâce à l'aide ou le soutien de toutes ces personnes.

C'est évident, ma gratitude va en premier lieu sans réserve à mes deux encadrants Julien et Freddy, que je ne pourrai jamais remercier assez. Comme j'aime bien les citations, en voilà une : "*Deux choses sont infinies : l'Univers et la bienveillance de Julien et Freddy. Mais en ce qui concerne l'Univers, je n'en ai pas encore acquis la certitude absolue*" [2]. Merci donc à Freddy qui, le compas dans l'œil, m'a orienté avec patience pendant trois ans quelque soit l'épaisseur de la brume. Merci pour les débuts vibrants au GANIL (thèse : J-3, jour mémorable). Merci ensuite pour tous ces échanges à l'issue desquels chaque problème finissait toujours par obtenir sa piste de résolution. Merci pour ton soutien dans les moments stressants et pour ta compréhensivité. Merci pour ton aide généreuse qui a été précieuse quand le temps commençait à manquer.

Merci aussi à Julien qui, la longue vue à la main, voit venir les icebergs et sait manœuvrer autour en marin expérimenté. Merci de tes conseils, de tes efforts pour être disponible malgré l'emploi du temps d'enseignant-chercheur (pire que ministre), de ne m'avoir jamais joué du pipeau (à défaut de la flûte) quand il fallait discuter, et d'avoir tout fait pour que cette thèse aboutisse.

Trêve de métaphore, je voudrais remercier aussi tous les membres de mon jury qui, grâce à leurs commentaires m'ont permis d'améliorer significativement ce manuscrit, et m'ont donné des pistes pour le futur. Merci aussi aux scientifiques avec qui j'ai pu collaborer (et le travail continue avec certains) : toute la collaboration HiCARI avec qui les échanges sont réguliers et constructifs, David et Frederic dont les calculs sont venus enrichir ce manuscrit et qui ont répondus à nos questions quand il y en avait, les équipes à Orsay qui m'ont

1. Pas d'un membre du jury
2. Vous apprécierez l'argument d'autorité

accueillis pour que je vienne manipuler un peu du Germanium, et enfin les équipes au japon sans qui le montage du mur à RIKEN aurait été impossible. Merci aussi à Jean Colin et Jean-Charles Thomas dont les conseils bienveillants m'ont accompagnés ces trois ans.

Plus indirectement, au laboratoire beaucoup de gens méritent des remerciements. Merci à Gilles (GB) de s'être préoccupé du bon déroulement de chaque thèse, et d'avoir créé des exceptions pendant la période de pandémie pour que les non-permanents aient un espace de travail au laboratoire malgré les restrictions. Merci au service info qui, affairé par l'utilisation de l'espace disque de mes simus, reste diplomate. Merci en particulier à Yoann qui a résolu **100%** des soucis liés à mon PC que je lui ai apportés (quelle heure est-il ?). Merci aussi de m'avoir appris à servir au bad, même si ça ne t'as pas empêché de me détruire juste après. Tout le groupe structure au LPC est à remercier aussi pour l'aide apportées sur mes présentations (renversantes), les messages à l'humour infatigable, et les remarques constructives. Merci en particulier à Miguel avec qui la lourde$^{\text{PM}}$ tâche de monter NEBULA-PLUS a été partagée avec plaisir entre deux bols de soba. Je ne voudrais pas oublier les (ex-)autochtones de ce coin bruyant (brillant ?) de laboratoire : Manu avec qui j'ai partagé un bureau et de nombreuses discussions, Jean-Luc qui a rythmé ces trois ans, Greg dont les blagues sur l'avancement du manuscrit on commencées le 1er Octobre 2020 mais se sont muées en conseils bienveillants pendant la troisième année (merci). Et puis globalement toutes les personnes du labo avec qui j'ai pu avoir des discussions.

Il ne me viendrait pas à l'idée, évidemment, d'omettre de remercier tous mes camarades de route les doctorants du LPC. On m'a très fortement déconseillé de faire une liste exhaustive, et je me retrouve à faire peut-être pire : une liste quasi-exhaustive ! À commencer par le commencement, Joël le guide suprême, vrai roi des doctorants merci de m'avoir fait régent. La lignée des intendants attendra le retour du vrai héritier. Cyril, merci pour les petits repas chez toi dans la totale légalité du couvre-feu, mais à cause de toi tout le monde pense que j'ai travaillé sur NEBULA, grr... Savitri, mon binôme, que d'aventures et que d'anecdotes. Merci pour les cafés COVID presque à la turque tellement ils étaient forts, pour les anchoïade et autres petits plats chez toi, les moments musicaux au jardin ou ailleurs, et les sorties (parfois farfelues). Alex-en-Provence désormais, vimeur acharné (ah !), tacticien en chef de la bataille entre le xubuntu et le windows sur feu mon vieux PC (on ne dira pas qui a gagné), gardien de l'ancien temple des thés et tisanes, empereur des sables quand il a le temps entre deux gratouillis timides de musique **médiévale**... Merci pour les gâteaux du vendredi (Ô traditions perdues), de continuer à nous proposer des activités malgré notre évidente mauvaise foi quand tu gagnes (je ne le redirai plus), et de t'être laissé entraîner dans des bourbiers par Savitri et moi. Merci William, merci Chloé (ça rappelle quelque chose) pour les petites sorties, pour votre calme, vous cotoyer a été apaisant. Bien sûr un énorme big-up aux futurs docteurs, les extrême-matter. Nathan, toi qui m'as donné un chaud repas quand dans ma vie il faisait froid, merci pour les discussions du

soir, le soutien, et l'oreille attentive. Ta thèse numéro une trônera sur mon étagère encore longtemps (jusqu'à ce que tu vienne la reprendre en fait). Merci Alex, le serial-voleur de kleenex (repenti, ne dérangez pas la police), dorénavant collectionneur de tout instrument de musique (je t'en envie quelques uns) et rare détenteur d'une plaque chauffante, bonne chance pour tous tes projets. Merci Aurel, j'attends toujours ce 1v1_d2_no_scope_no_blabla. Bon courage pour cette dernière année qui commence fort. Merci Louis, si tu prévois un retour à Djibouti, n'oublie pas de passer à Orsay, on fera un ROOT je te jure que c'est bien. Raïssa la sista tu es la championne incontestée (j'ai trop peur de dire l'inverse) du décathlon du LPC. Nouvelle leader culturelle du groupe (l'influence do Brasil crève les yeux), merci pour toute la vie que tu amène. Étant donné que l'APC est ta deuxième maison, j'espère bien te recroiser en Île-de-France. Vivement la mondialisation (imminente) des café-docs. Merci Emeu pour les biscuits de ta mamie, je te vois transformer Alex en collectionneur de Gin en plus du reste, STOP ! Audrey, j'ai réussi à oublier de te remercier pour avoir géré la visio pendant ma soutenance (merci donc), pouet pour le gâteau et bonne fanf avec la chance. Promis j'essaie de te laisser un peu d'espace disque sur le serveur pour que tu puisse travailler. Narton, où que tu sois, merci pour ton sérieux dans ta recherche et ta bonne humeur (en particulier pendant cette fameuse ballade à vélo) et bon courage pour ce qu'il reste du manuscrit, on en voit le bout. Vous quitter est douloureux, mais si c'est pas moi qui m'en vais en premier, ça aurait été vous d'abord. Voyez donc ça comme de l'égoïsme. J'ai aussi une pensée pour tous les doctorants (la relève) et frais docteurs avec qui j'ai moins eu l'occasion d'échanger (Guille, Hoa, Sacha, Mohammad, Romain, Kaciel, Anthony, Antonin...), bon courage à vous pour la suite. Chiru thank you as well for everything, the unforgettable memories from our first night out, and the nice traditional meals you prepared us.

Bien sûr, la vie ne se résume pas au labo, quoi de mieux pour oublier tous les codes d'analyse qui ne fonctionnent pas que d'aller discuter musique (entre autre) avec des gens formidables. Mille mercis à toute la mazel-famille, je ne referai pas l'erreur d'essayer de citer des noms, ça n'aurait pas de sens de toute façon : on ne choisit pas entre papa ou maman. Ces deux ans passés à faire vibrer de l'acier à vos côtés sont inoubliables, et je ne doute pas que cette institution caennaise existera toujours pour mes futurs passages à Caen.

En parlant de Mazel, merci aussi Cesare, trois ans à Caen ont suffit à t'y rendre légendaire. Tu m'a réconcilié avec le limoncello et fâché avec tous les ronfleurs. En parlant de légende cette fois-ci, Seb merci de me sortir un peu de chez moi (quand je donne des nouvelles), et de rester un bon pote alors que j'ai failli t'assécher en t'amenant dans le Sud. Merci aussi tonton Raph pour t'inquiéter de mon bien-être, je n'ai pas eu l'occasion de te dire au revoir mais les chances sont minces que je ne te recroise pas.

C'est bien sûr dans l'émotion que je quitte tout ce beau monde, mais Caen reverrai-je ?

Oui, bientôt je le crois.

Il y a environ 10 ans, j'ai réalisé que la physique, c'était ça que je voulais faire. Merci donc aussi à M. Lucbert qui a grandement participé à transformer une matière dans laquelle j'avais simplement quelques bonnes notes en une passion, et à tous les enseignants qui m'ont encouragés par la suite.

Et puis il y a ceux que l'on connait depuis longtemps dont on ne s'éloigne jamais vraiment. Merci à tout le groupe des doctorants délocalisés (o'blady), plus que quelques-uns et on y sera tous passés. Et puis encore il y a ceux que l'on connaît depuis beaucoup plus longtemps. Adi, Elo, merci d'être toujours là pour moi, malgré la distance et parfois les longs silence. Merci pour les efforts que vous faites pour prendre des nouvelles et même venir me voir. Popo, merci de me supporter au quotidien et de m'aider à assumer mes choix, merci pour ta franchise inébranlable. Et puis pour finir dans l'évidence, il y a "*ceux dont c'est la fonction de nous aimer*" (c'est bien réducteur), qui offrent leur soutien les yeux fermés sans poser la moindre question. Merci papa, maman, Clem, et toute la famille étendue (beaucoup de monde) pour votre soutien inconditionnel nécessaire pour tenir le cap aussi longtemps.

Contents

List of Figures

Chapter 1

Motivations

1.1 Nuclear shell structure and evolution

From the observations of binding energy variations [1] across the nuclear chart and relative abundances of stable nuclei [2] in the beginning of the 20^{th} century, came the first evidences of shell structure in nuclei in analogy to the atomic shells. The measurements indicated that nuclei having a number of protons or neutrons of 2, 8, 20, 28, 50, 82, 126 were more likely to be stable and abundant than the others.

Those nuclei have a first excited 2^+ state (written 2_1^+) higher in energy than their neighbours and have lower transition probability $B(E2, 2_1^+ \rightarrow 0_1^+)$. Figure 1.1 shows the increase of the 2_1^+ energy for these specific numbers of neutrons. Another indicator is the variation of the two-neutron/proton separation energy $\delta S_{2n}(N, Z) = S_{2n}(N+1, Z) - S_{2n}(N-1, Z)$ (similarly for S_{2p}) which also presents a drop at the magic numbers [3].

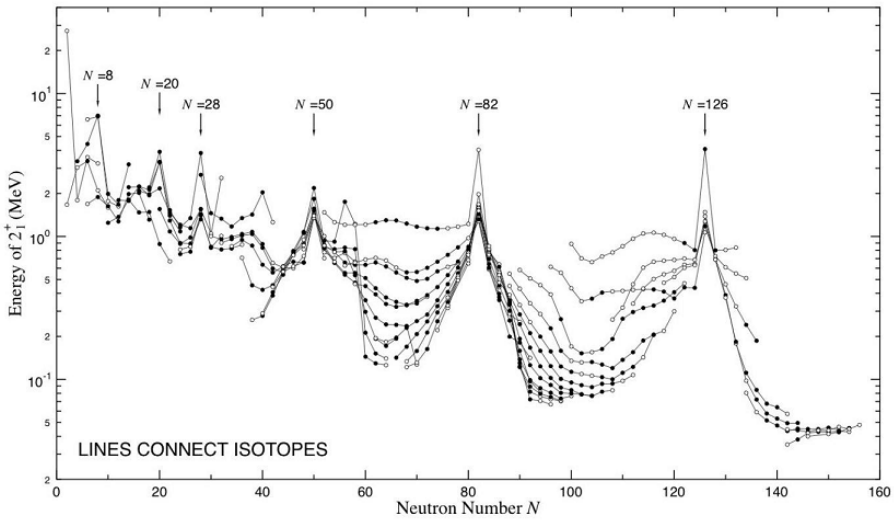

Figure 1.1 – Energy of the 2_1^+ state along several isotopic lines. Data from [4].

In order to reproduce these observations and predict energy levels of nuclei, theoretical models describing the nucleons as individual particles orbiting in a potential well generated by all the other nucleons (the mean-field potential) have been investigated. This approach was motivated by the observation of saturation properties, the short range and the attractiveness of the nucleon-nucleon interaction, and the progressive experimental evidences of a shell structure in nuclei. Depending on the shape of the potential chosen, different "magic" numbers were arising. For a while, this approach could not establish the full list of observed magic numbers. Taking into account spin-orbit coupling in the formulation of the Hamiltonian of the system, first proposed in 1949 by M. Mayer [5], was finally the key to successfully predict the observed magic numbers. Figure 1.2 shows the energy ordering of single-particle orbitals calculated in a spherical shell-model framework using different shapes of the potential and the evolution that the additional spin-orbit term induces. One can indeed observe large energy gaps between some orbitals at specific numbers of protons/neutrons (2, 8, 20...). This approach efficiently reduces the A-body strongly interacting problem to A effective one-body problems.

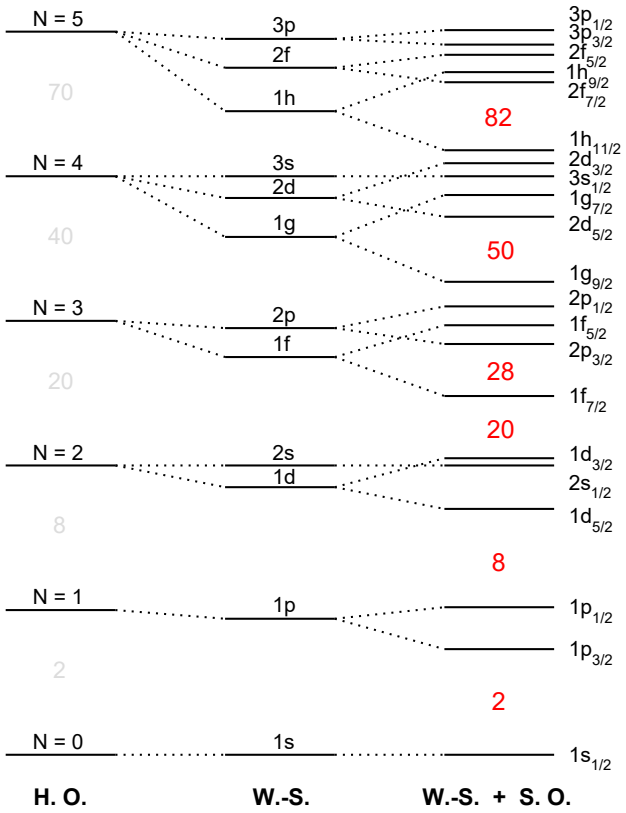

Figure 1.2 – Energy of single-particle orbitals as predicted by the spherical shell-model using (left) a harmonic potential, (middle) a Wood-Saxon potential, and (right) a Wood-Saxon potential with a spin-orbit coupling. Extracted from [6].

The magic numbers established for stable nuclei were believed to be universal until progress in experimental techniques allowed to perform spectroscopy of very exotic nuclei.

In 1984, β-decay data on ^{32}Mg gave one of the first evidences of the breaking of the $N = 20$ magic number at $Z = 12$ far from stability [7, 8]. For about twenty years and with the advances of facilities producing exotic nuclei, studying shell evolution has been at the heart of scientific research in nuclear structure.

An example of structural evolution away from stability is illustrated in figure 1.3 with the breaking of the $N = 28$ shell closure. In figure 1.3a, the energy of the first excited state 2_1^+ is plotted against the neutron number N (similarly to figure 1.1). For the calcium isotopes ($Z = 20$), it shows a large increase at $N = 28$ and $N = 20$, those two isotopes being doubly magic. However the rise of $E(2_1^+)$ is much smaller at $N = 28$ for argon ($Z = 18$) and sulphur ($Z = 16$) isotopes, hinting at progressive vanishing of this shell closure once one goes below calcium. This vanishing is confirmed by the 2_1^+ energies of the silicon isotopes which do not show any rise at $N = 28$. Figure 1.3b presents shell-model predictions of single-particle orbital energies for $N = 28$ isotones. The prediction shows a weakening of the $N = 28$ shell closure as the energy gap between the $0f_{7/2}$ and the $1p_{3/2}$ orbitals is reduced when transiting from $Z = 20$ to $Z = 8$, that is to say when transiting from stable nuclei (^{48}Ca) to exotic ones (high N/Z ratio).

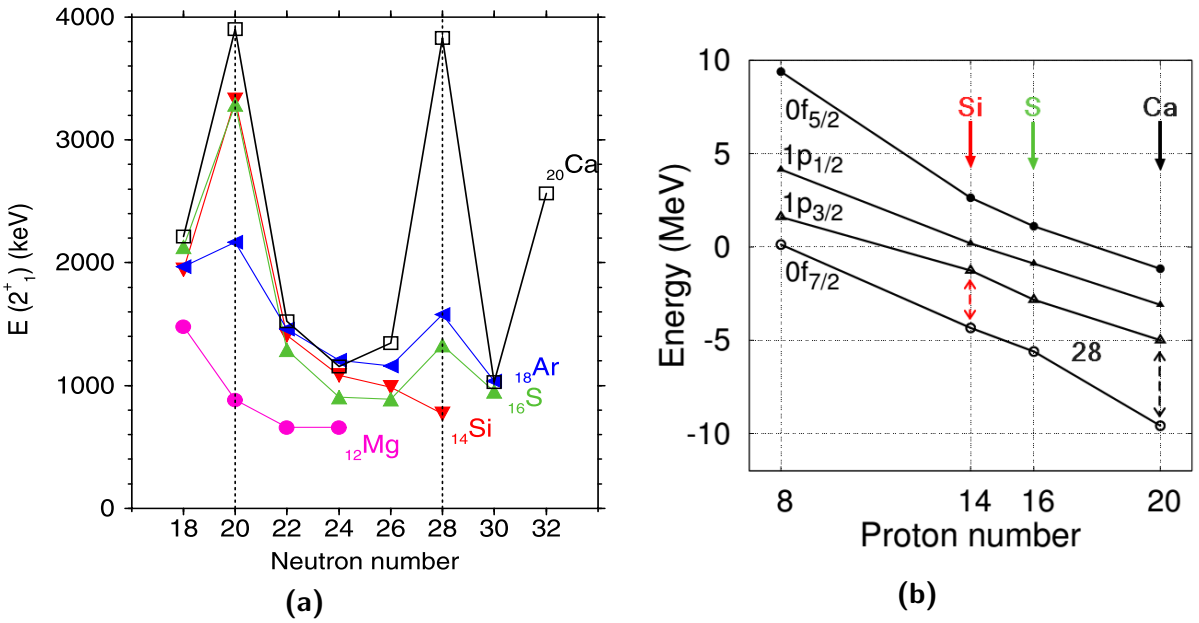

Figure 1.3 – (a) Experimental values of the 2^+ state's energy for the isotopic chains from $_{12}$Mg to $_{20}$Ca. Extracted from [9]. (b) Variation of the neutron single-particle orbital's energies along some $N = 28$ isotones as predicted by shell-model calculations using the interaction described in reference [10]. Adapted from [11].

This weakening reduces the energy cost of exciting nucleons across the gap, and progressively deformed configurations involving this type of particle-hole excitations (called "intruder configurations") may become energetically favourable compared to the closed-

shell spherical configuration (details in section 1.2.1). When this is the case, it leads to vanishing the magic character, like in ^{42}Si (figure 1.3a).

Such evolution of single-particle energies and associated shell gaps originate from certain terms of the underlying nuclear interaction whose magnitude depends on the N/Z ratio. Their study is thus of high importance to constrain nuclear models either based on microscopic forces or effective ones. In the shell-model framework, the Hamiltonian can be separated into a monopole part (governing the spherical nuclear mean field and defining shell gaps) and higher multipole parts (containing particle-particle correlations leading to collectivity and deformation). The mechanism for the creation or disappearance of magic numbers originates from a subtle competition between these two parts and their underlying components (central, spin-orbit, tensor, etc). Among the important terms of the nucleon-nucleon interaction, the tensor force between nucleons was for example interpreted as one of the driving mechanisms of shell evolution in several mass regions [12].

In the case of the vanishing of the $N = 28$ shell gap shown here, decompositions of empiric interactions suggest a subtle competition between central and tensor components [11]. This shell gap being of the "spin-orbit type" (that is to say it is predicted thanks to the addition of the spin-orbit component), it raises the question: are similar effects at work for all spin-orbit gaps? Studying the evolution of the next gap of this kind ($N = 50$) can help us shed some light on the microscopic origin of spin-orbit magic numbers in general.

Moreover, the overall robustness of $N = 50$ has direct consequences on binding energies of nuclei away from the shell closure and thus on the drip-line location. These quantities are crucial for nucleosynthesis r-process calculations aiming at understanding abundances of elements in the universe. The path of the r-process is still in debate, but it is widely thought to pass through such a neutron-rich region towards the neutron drip line where experiments are too challenging at present to have enough data, and theoretical models are not predictive enough [12].

1.2 The $N = 50$ case

The magic numbers arising from the spin-orbit coupling were believed to be more robust and less likely to weaken far from stability than the ones that are predicted by a harmonic potential [8]. Yet, the example given previously showed a weakening of the $N = 28$ shell gap far from stability questioning the robustness $N = 50$ shell closure. In this perspective, characterising the magicity of ^{78}Ni and studying shell closures in this region has been (and remains) one of the major goal of most radioactive ion beam (RIB) facilities in the world. The combination of recent achievements in RIB production and theoretical calculations has allowed to start developing this scientific program and opened interesting questions on the presence of low-lying intruder states and shape coexistence around ^{78}Ni.

1.2.1 Intruder states

The usual shell-model description of a given nucleus around a closed shell separates a core containing filled orbitals, and valence nucleons on orbitals above the core. In general, the core and the valence orbitals are separated by a large energy gap implying a high cost for exciting nucleons from the core above the gap. However, if this gap gets smaller (away from stability for example) the cost of these "particle-hole" excitations can be significantly reduced and even compensated by the correlation energy gained by exciting nucleons above the gap (quadrupole deformation energy, pairing, ...). In such cases, excited states built from "particle-hole" excitations can become energetically favourable and compete with the closed-shell configuration.

Such excited states are called "intruder" configurations. They are usually more deformed than the "normal" configuration. Their lowering in energy in a nucleus or a region of the nuclear chart can indicate a reduction of the shell gap or a large gain of correlations due to the symmetries of the valence orbitals for example [13]. The coexistence of different configurations at low energy having different shapes is called *shape coexistence* (see [14] for a detailed review).

1.2.2 ^{78}Ni as a doubly magic nucleus

The ^{78}Ni nucleus is predicted to be one of the most neutron rich doubly magic nuclei. Being very exotic, it is very challenging to produce and study, nevertheless a few experiments have recently been successfully conducted in the region (see the chart in figure 1.4) to study the evolution of the $N = 50$ and $Z = 28$ shell closures.

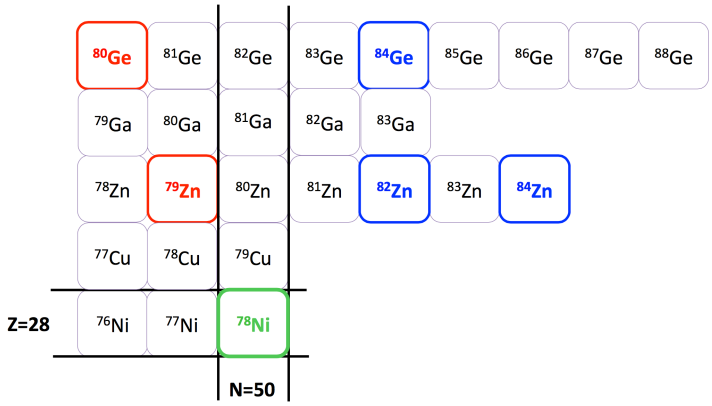

Figure 1.4 – Region of the nuclear chart around ^{78}Ni. Nuclei highlighted in colour indicate results recently obtained revealing the presence of intruder states below $N = 50$ (red), indication of shape coexistence in ^{78}Ni (green), and evolution of collectivity above $N = 50$ (blue).

Until very recently, no spectroscopic information on ^{78}Ni was available and only system-

atics of the $N = 50$ energy gap extracted from mass measurements down to Zn isotopes (Z=30) allowed to speculate that ^{78}Ni should keep its magicity [3, 15]. Only in 2019, the first direct experimental evidence for its magicity was reached with its first spectroscopy at the RIBF-RIKEN and the measurement of the first 2^+ excited state energy [16]. This results shows a clear rise of $E(2_1^+)$ in the systematics along the Ni isotopic chain as shown in figure 1.5 thus implying a well defined shell closure at $N = 50$.

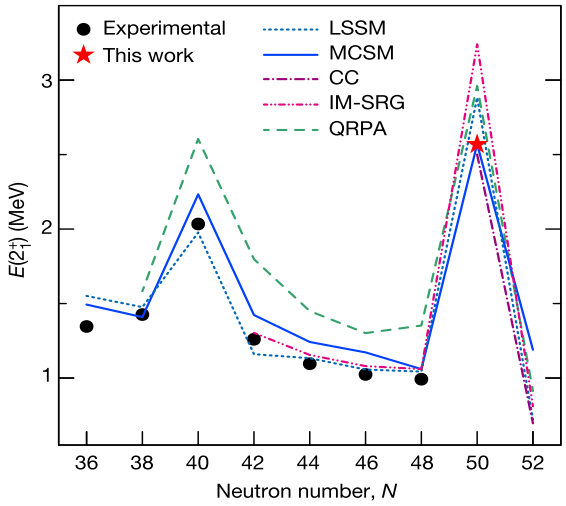

Figure 1.5 – Experimental $E(2^+)$ values for even-even nickel isotopes compared with phenomenological calculations (taken from ref [16]).

On the other hand, spectroscopic studies performed just below the shell closure ($N < 50$) on $^{80}_{32}$Ge and $^{79}_{30}$Zn showed signs of shape coexistence with the presence of deformed configurations at rather low energy. Additionally, the region below $Z = 28$ has also been investigated by measuring the 2^+ energies of $^{66}_{24}$Cr and $^{70,72}_{26}$Fe [17] which were found to be consistently low, signifying the presence of an onset of deformation right below $Z = 28$ that could extend towards the N=50 shell closure below ^{78}Ni and would imply its rapid vanishing. These studies and few others point to the possible importance of intruder configurations in ^{78}Ni and around [18]. The next section will summarise the conclusions and associated open questions.

1.2.3 Hints of intruder states in the region of ^{78}Ni

Mainly, four studies allow to speculate about the lowering in energy of intruder configurations in the region.

In ^{78}Ni

As stated before, the ^{78}Ni nucleus itself has been studied (see figure 1.5) and a first experimental level scheme has been sketched. This level scheme is displayed in figure 1.6

along with theoretical calculations [19].

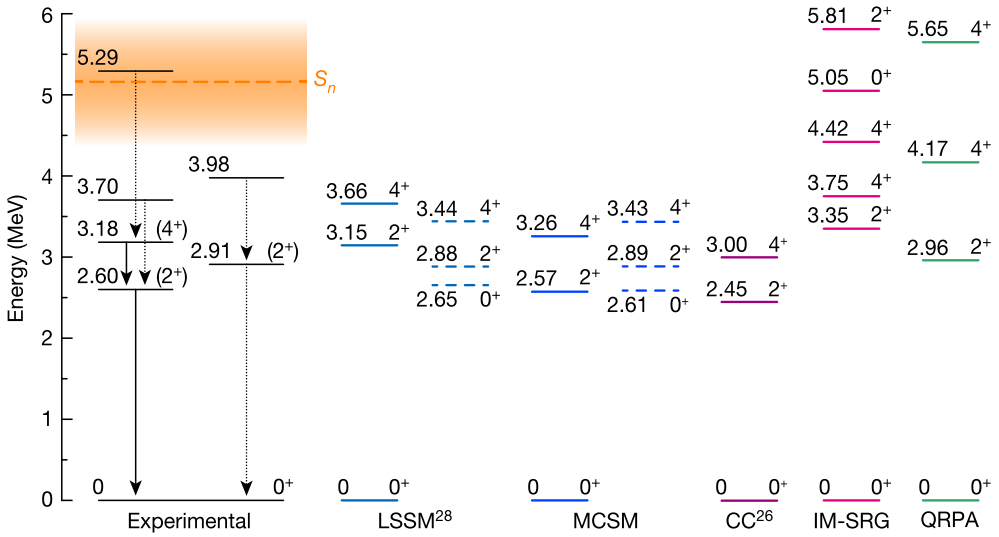

Figure 1.6 – Experimental and predicted level schemes for ^{78}Ni. Dashed arrows represent transitions with significance level inferior to 5σ. S_n is the neutron separation energy (the shading is its error). Extracted from [16].

Coincidences between the 2.6-MeV transition and the 0.58-MeV, 1.1-MeV, 1.5-MeV, and 2.11-MeV transitions allowed to propose the left band of the experimental levels (at 2.6, 3.18, 3.70 and 5.29-MeV). Two other transitions at 2.91-MeV and 1.07-MeV could not be confirmed to be in coincidence, but their intensity appearing correlated, the hypothesis is made that they are in the same energy band. We therefore see the appearance of a second energy band with a 2^+ state of energy slightly higher than the first one. In addition, the authors of this study did not observe the 2.91-MeV transition in the (p, 2p) channel but only *via* the (p, 3p) one which is interpreted as a hint of a dominating multi particle - multi hole configuration. In addition, a low-lying intruder 2^+ state is predicted by LSSM [1] and MCSM [2] models only if the full *sdg* orbitals are included. This supports the idea that there could be a deformed intruder configuration in ^{78}Ni at low excitation energy. However, because of the extreme exoticity of ^{78}Ni the lack of statistics makes the two transitions measured in the deformed energy band not significant enough. No firm conclusion can therefore be drawn on the presence of shape coexistence in ^{78}Ni, and further studies are needed.

Below $N = 50$

Results obtained for $^{79}_{30}$Zn$_{49}$ are shown in figure 1.7. On the right are shown the experimental level schemes of $N = 49$ isotones. The $1/2^+$ and $5/2^+$ states are good candidates for one-particle two-holes (1p-2h) intruder states as $s_{1/2}$ and $d_{5/2}$ are orbitals above $g_{9/2}$.

1. Large-Scale Shell Model
2. Monte-Carlo Shell Model

On the left of the figure, the experimental mean squared radii measured through collinear laser spectroscopy are compared with a spherical shell-model. While the rms charge radius of the ground state of ^{79}Zn follows well the phenomenological predictions, it can be seen that the $1/2^+$ intruder state has a larger radius than the ground state (difference of 0.03 fm of root mean square radius). More recently, in reference [20] a mass spectroscopy study using two different methods further support the argument that the $1/2^+$ and $5/2^+$ states in ^{79}Zn are more deformed than the ground state.

In addition, looking at the right figure where the potential intruder states along the $N = 49$ isotonic line are linked by a dashed line, one can observe the quick rise of the intruder state's energy as we go from ^{83}Se towards higher Z. It indicates a rather robust $N = 50$ shell closure at $Z = 40$. On the other hand, the comparatively slow rise of the intruder state's energy as we get closer to $Z = 28$ raises questions about the relative width of the $N = 50$ gap at $Z = 28$ [21].

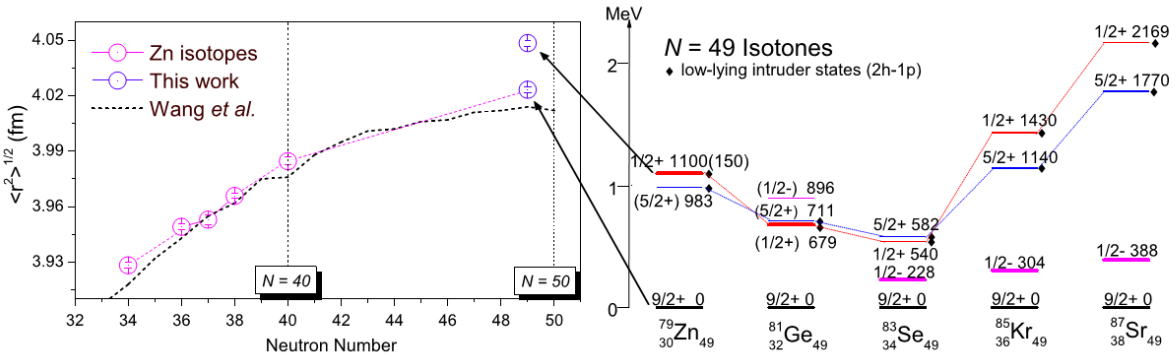

Figure 1.7 – (left) Experimental root mean square charge radii of Zn isotopes compared with a phenomenological model. (right) Energy of the low lying states of $N = 49$ odd-mass isotopes.
The arrows relate the two last points in the left plot to the corresponding states on the right. Extracted from [22, 23].

Another study probed the nuclear structure near ^{78}Ni [24]. The level scheme of ^{80}Ge has been constructed by detecting conversion electrons from the ^{80}Ga β decay. Figure 1.8a presents the spectrum obtained. In this spectrum, a peak can be seen at 628-keV. Using lifetime analysis, it has been attributed to the gallium decay, and therefore should correspond to a transition in ^{80}Ge. This is the very first time this transition has been measured. Extrapolating from previous work on ^{72}Ge, it has been proposed that the transition may originate from a second 0_2^+ state. In addition, studies of coincidences in γ-ray decay could indicate the presence of a third state at 2403-keV, with proposed spin-parity 2^+. A few years later, two other experiments performed the β-decay spectroscopy of ^{80}Ga and were designed to enhance population of low-spin states but found no evidence of this reported

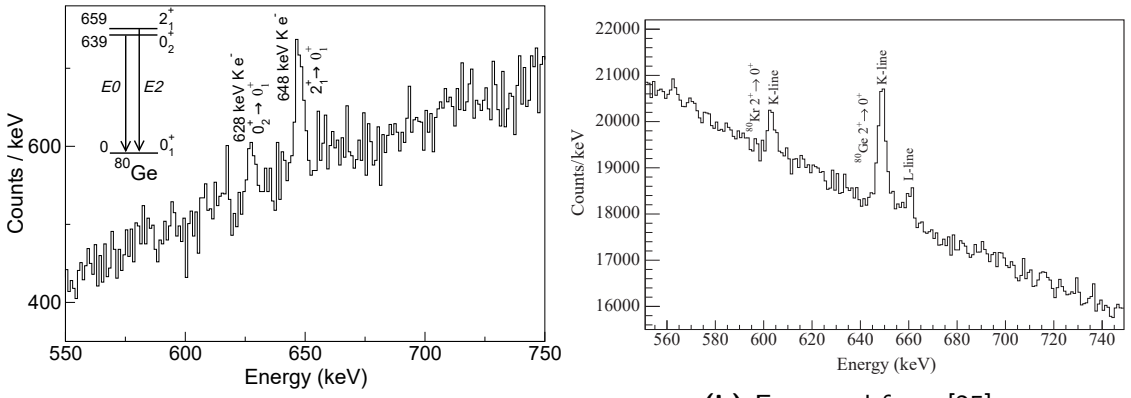

(a) Extracted from [24]

(b) Extracted from [25]

Figure 1.8 – ^{80}Ge energy spectra from the beta delayed conversion electron spectroscopy from ^{80}Ga to ^{80}Ge. In (a) a new transition tentatively assigned to a second 0_2^+ state is measured. In (b) a more recent experiment does not provide any indication for such a state.

low lying 0_2^+ [25, 26]. The electron spectrum from [25] shown in figure 1.8b demonstrates the enhanced statistics and an absence of signal at 628-keV reported previously. These non-observations combined with recent Large-Scale Shell Model calculations predicting such a coexisting 0_2^+ at much higher energy (at 2 MeV) indicate that low-energy shape coexistence is finally not present in ^{80}Ge.

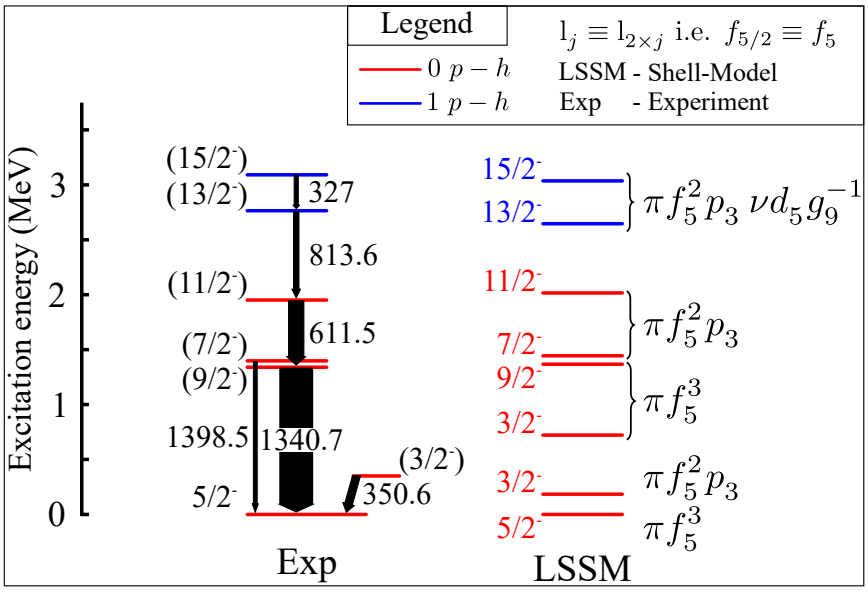

Figure 1.9 – Level schemes for ^{81}Ga obtained from: (left) in-flight γ-ray spectroscopy using the AGATA germanium multidetector in [27], and (right) Large Scale Shell Model calculations using the PFSDG-U interaction. Levels in blue correspond to the new 1 particle - 1 hole intruder candidates. Extracted from [27].

Finally in ^{81}Ga [27], two new high energy states at 2567.8(11)-keV and 3092.8(23)-

keV were measured and seem to correspond well to the two particle-hole configurations predicted by the LSSM calculation using the PFSDG-U interaction [18], indicated in blue for measurements and calculations in figure 1.9. In addition, the energy of those core excitation levels compares very well to the $N = 50$ shell gap in ^{81}Ga obtained from binding energies.

Above $N = 50$

Experimental results above $N = 50$ are (expectedly) rarer. A recent study measured the lifetimes of 2_1^+ states in $^{84}_{32}$Ge, $^{82}_{34}$Se and $^{80}_{36}$Kr. From them, the quadrupole transition probabilities $B(E2; 2^+ \rightarrow 0^+)$ have been deduced, and the results are shown in figure 1.10.

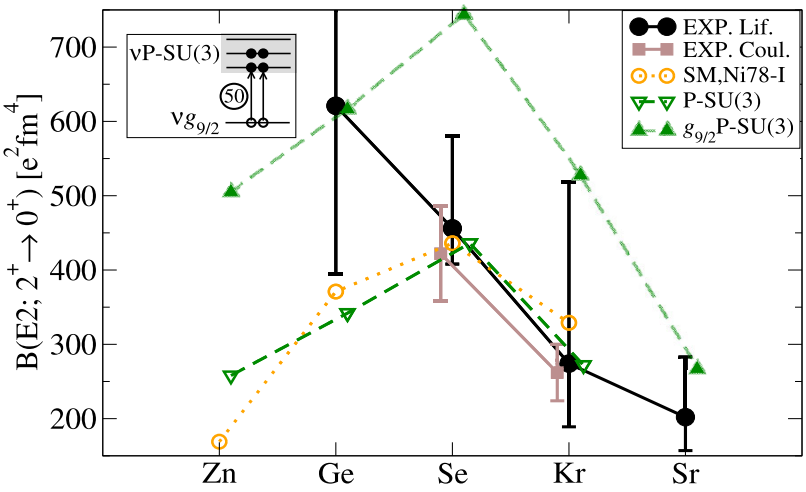

Figure 1.10 – Quadrupole transition probability $B(E2; 2^+ \rightarrow 0^+)$ of the $N = 52$ even-even isotones from $Z = 38$ to $Z = 30$ compared with shell-model calculations and a microscopic model. Extracted from [28].

The very high value measured for $^{84}_{32}\text{Ge}_{52}$ indicates the presence of a large collectivity. This cannot be entirely reproduced by state-of-the-art shell-model calculations (yellow circles on the figure). The only way to explain this result was to include possible 2p-2h excitations in the ground state configuration in the calculations where a pair of neutrons in the $g_{9/2}$ orbital has been promoted across the $N = 50$ gap. If this is true, a shape inversion could happen from $^{86}_{34}\text{Se}_{52}$ to $^{84}_{32}\text{Ge}_{52}$ (that is to say the deformed configuration is more energetically viable than the spherical one). However, because of the very large error bars on this experimental value definite conclusions cannot be made and require further investigations.

Recent in-flight γ-ray spectroscopy of the As chain showed good agreement with theoretical calculations with the full *pf-sdg* valence space. Complementary calculations predict prolate deformations in ground states and excited states of ^{85}As and ^{87}As [29]. This sup-

ports the collective nature of low lying states in the region above $N = 50$.

Because of remaining uncertainties on all the previous experimental results, none of them allows to conclude unambiguously on the presence of an intruder configuration. Though they tend to be explained by the same mechanisms: nucleon-nucleon correlations and particle-hole excitations. Calculations using the Large-Scale Shell Model with the PFSDG-U interaction [18] using an inert core of ^{60}Ca and a valence space comprising the full *sdg* orbitals for neutrons have a great success reproducing newly gathered data in this region. Although we described the intruder mechanism schematically here in terms of simple neutron particle-hole excitations above a gap, LSSM calculations depict a more complex situation since it includes somehow dynamically the effect of these p-h excitations on protons and the additional gain in correlations. This implies a significant reorganisation of valence orbitals due to neutron-proton interaction and also configuration mixing in some cases [27].

More detailed and precise observables are needed to further test such a theoretical interpretation (lifetime, spectroscopic factor, ...). This motivated the experiment described in this manuscript performed with state-of-the-art instruments to identify such intruder states in an unambiguous way and study their properties.

1.3 Experimental goals

1.3.1 Reaction mechanism

In order to study the shell evolution in the ^{78}Ni region at $N > 50$, this PhD experiment was performed at the RIBF facility, with the aim to identify for the first time intruder states above $N = 50$ and measure their energy, lifetime and spectroscopic factor. More precisely, the goal is to search for signs of the presence of 2p-1h intruder states in one of the two last odd-even $N = 51$ isotopes before ^{79}Ni: $^{83}_{32}\mathrm{Ge}_{51}$.

To do so, we illustrate in figure 1.11 the selective nucleon-removal mechanism used to populate the states of interest and the nucleon configuration probed. The example given is the $^{84}\mathrm{Ge}\xrightarrow{-1n}{}^{83}\mathrm{Ge}$ reaction. In order to populate a 2p-1h configuration by introducing a hole in the $g_{9/2}$ orbital, it is necessary to start from $N = 52$ (even more neutron-rich nuclei) and then remove a nucleon from this orbital. This highly challenging approach explains why the experiment was not carried out before. Presently, only RIBF allows to do it (see next chapter) with still low beam intensity (5000 pps for ^{84}Ge).

There are two possible configurations resulting from the knockout reaction:

— The first one is when a neutron is removed above the gap (in the $d_{5/2}$ or $s_{1/2}$ orbital) giving "normal" configurations and populating essentially the $5/2^+$ ground state

(figure 1.11a illustrates the filling of the orbitals for this state) and the $1/2^+$ first excited state (neutrons in ^{84}Ge can partially occupy the $s_{1/2}$ orbital).

— Another possibility is that the nucleon is removed from below the gap, most probably from the $g_{9/2}$ orbital, giving a $9/2^+$ state at a higher energy. These states correspond to the intruder configuration of interest (figure 1.11b).

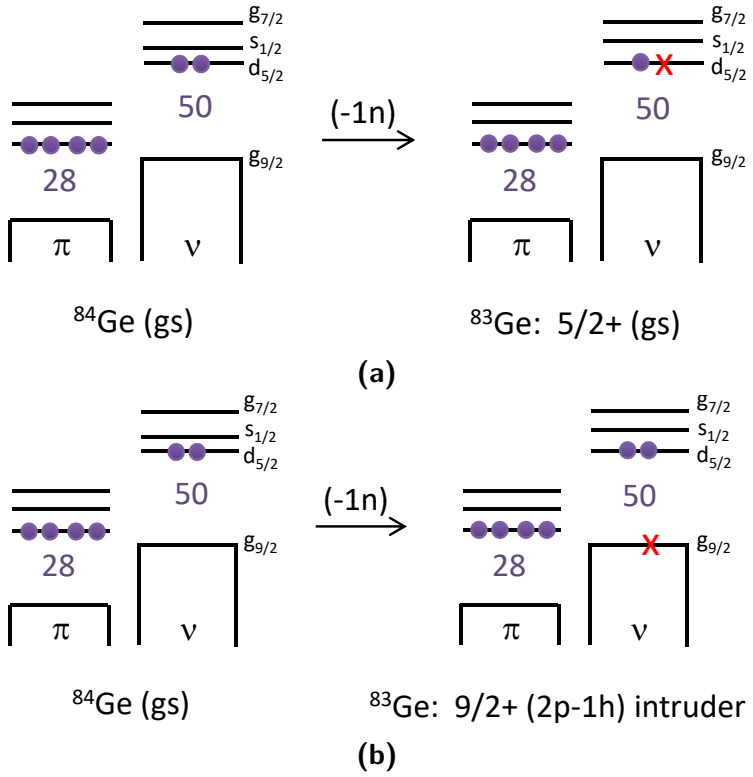

Figure 1.11 – Schematic view of a ^{84}Ge$\rightarrow^{83}$Ge neutron knockout reaction. Adapted from [21]. (a) Normal configuration. (b) Intruder configuration.

This type of reaction is optimal to study single-particle orbitals. Moreover, the kinematic conditions at RIKEN (250 MeV/nucleon, $\beta \approx 0.6$) are adapted to assume that the core is inert (eikonal approximation) and that the mechanism is done in one step (sudden approximation), allowing to consider the reaction direct and selective.

Once a given state is populated at the reaction vertex, the product will decay through γ-ray emission either directly to the ground state, or by a cascade of several transitions. These γ rays, detected event by event, are then used to determine the population of a given state simply from a balance between transition feeding and de-exciting this state.

The odd-even $N = 51$ nuclei have a large density of states of other nature than the 2p-1h intruders with various spin-parities. Therefore a very good energy resolution is needed to be able to distinguish which states was populated. For this purpose, the recently designed

germanium array HiCARI [3] (described in the next chapter in more details) is particularly suited.

1.3.2 Targeted observables for ^{83}Ge

The current knowledge of the ^{83}Ge level scheme obtained by Delafosse *et al* in [3] is reported in figure 1.12 along with Large Scale Shell Model [18] and Core-Particle (CP) [8, 30] calculations.

The main experimental result of this recent work combining β-decay spectroscopy of ^{83}Ga and a plunger measurement is the identification of the 1359-keV state as a good $(9/2^+)$ 2p-1h intruder candidate. More precisely, this identification is based on:

— The large $\log(ft)$ measured (10.1(5)u) to this state. It corresponds to a first-forbidden unique transition and leads to possible spin-parities of $(1/2^+)$ or $(9/2^+)$ under the hypothesis of a $(5/2^-)$ spin assignment for the ground state of ^{83}Ga based on systematics.

— The population of this 1359-keV state in a fusion-fission study at GANIL with ^{238}U(^{9}Be, f). This is more in favour of an Yrast/Yrare $(9/2^+)$ than a $(1/2^+)$ at this energy.

— A larger lifetime $\tau = 74^{+73}_{-67}$ ps for this 1359-keV state compared to neighbouring states with $\tau < 5$ ps. This value remains however quite uncertain due to difficulties in the plunger measurement originating from low statistics and the presence of a low 1346-keV transition exactly where the shifted peak of the 1359-keV transition was expected.

The two theoretical models which results are presented in the figure, predict a state of this nature at slightly different energies: 1336-keV and 1004-keV. Measurements of its angular momentum, spectroscopic factor, and further constraints on its lifetime will allow to characterise the nature of this state and evaluate the importance of intruder configurations.

As previously mentioned, high density of states around this $9/2^+$ state comes from a core excitation (to its 2^+_1 state) coupled with a valence nucleon in the $d_{5/2}$ orbital (spin-parities $1/2^+$, $3/2^+$, ..., $9/2^+$) or in the $s_{1/2}$ orbital (spin-parities $3/2^+$, $5/2^+$). Consequently they are close to the 2^+_1 energy of ^{82}Ge at 1348-keV, which makes them also very close to the potential intruder $9/2^+$ state at 1359-keV. In addition, the strength of the intruder configuration could also be spread among other $9/2^+$ states at higher energy (as predicted by the CP [4] model in figure 1.12) where the density of states is large. Therefore a very selective reaction and a high resolution are needed to identify precisely the populated states.

3. High-resolution Cluster Array at RIBF
4. Core-particle coupling

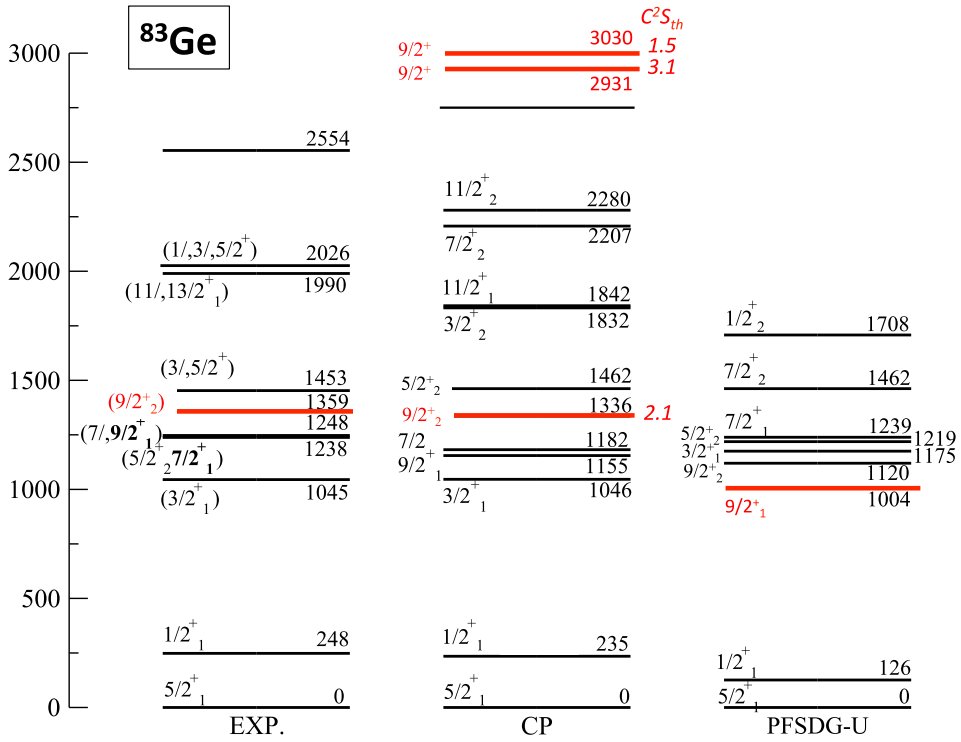

Figure 1.12 – The experimental level scheme of ^{83}Ge obtained through β-decay and γ-ray spectroscopy, compared with two calculations: CP corresponds to a phenomenological core-particle coupling model while PFSDG-U stands for a Large-Scale Shell Model calculation with the PFSDG-U interaction [18] restricted to few states due to its computational cost. Extracted from [3, 31].

In order to demonstrate that a given state corresponds to a neutron removal from the $g_{9/2}$ orbital, the measured parallel momentum of the ^{83}Ge product can be used. Indeed, given that the knockout reaction of a nucleon is direct, the momentum is conserved, and the heavy knockout product keeps the signature of the momentum of the removed nucleon. The identification procedure is shown in figure 1.13 where the effect of the angular momentum of the removed nucleon on the shape of the parallel momentum distribution of ^{83}Ge can be seen. The distribution width for a $L = 4$ is nucleon removal is significantly larger than in the $L = 0, 2$ cases (experimental resolution included). Of course, a $L = 4$ nucleon removal could in principle result from a nucleon knockout either from a $g_{7/2}$ orbital or a $g_{9/2}$ one. The $g_{7/2}$ orbital being far away in energy according to shell-model calculations, it can be reasonably excluded. The same procedure can be applied for the identification of the other states. This also shows that a good resolution is needed in order to distinguish between the different distributions in parallel momentum.

The last observable that will be used is the lifetime, since the lifetime changes according to the single-particle or collective nature of the state. A sizeable lifetime implies that the γ-ray decay vertex can significantly differ from the reaction vertex. This results in a degraded Doppler correction and the peak shape becomes shifted and asymmetric. The obtained peak

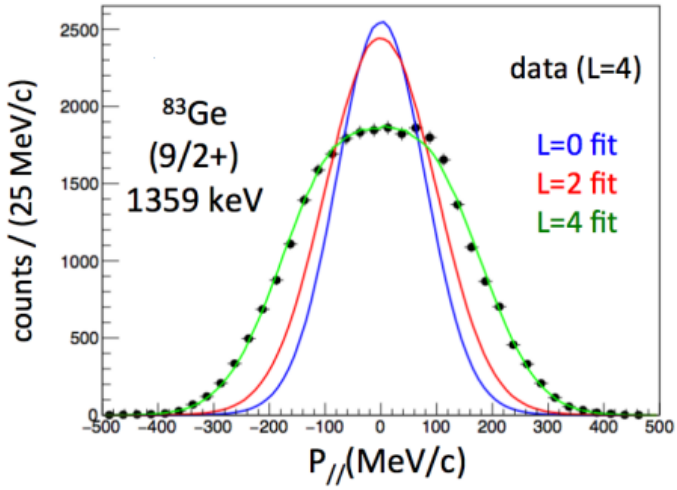

Figure 1.13 – Parallel momentum distributions of the residue for different angular momentum L of the knocked-out neutron. The points show the expected distribution for ^{83}Ge residues from the knockout of a $L = 4$ neutron. Extracted from [31].

shape can thus be fitted to determine the lifetime. More details on this method will be given in section 2.3.2.

The next chapter describes the beam production method at the RIBF-RIKEN facility as well as the identification methods, and discusses the advantage of using the HiCARI array for this experiment.

Chapter 2

Experimental setup

The SUNFLOWER collaboration developed the HiCARI [1] germanium multi-detector to enable high-resolution γ-ray spectroscopy of very exotic radioactive ions produced in-flight at the RIBF [2] facility. To do so, the HiCARI array was placed at the secondary target point, between the BigRIPS fragment separator and ZeroDegree spectrometer, enabling together an unambiguous identification of reaction channels. HiCARI has been used during two campaigns in fall 2020 and spring 2021 to perform primarily nucleon knockout and Coulomb excitation. Most experiments targeted the spectroscopy of intermediate-mass ($N \approx$ 50-82) nuclei with a rather large density of states for which HiCARI had a better resolving power than previous scintillator systems used at the RIBF. This chapter will present the essential components of the experimental setup we used to study the ^{84}Ge(Be, X)^{83}Ge reaction channel during the first experiment (NP1912 -RIBF196) of the campaign. The description of the accelerator and spectrometer layout will be followed by a presentation of the secondary target setup along with the HiCARI γ-ray spectrometer.

2.1 Beam production at RIBF-RIKEN

2.1.1 In-flight radioactive beam production

At the RIBF, the radioactive ion beams are produced in flight. This production technique consists in sending an intermediate/high energy (typically $E > 30$ MeV/u [32]) heavy beam on a relatively light target (beryllium, carbon) to produce rare isotopes by in-flight fragmentation or fission. The produced cocktail beam of radioactive fragments is then separated by a fragment separator to reach the secondary target for experiments.

This method has several key features:

1. High-resolution Cluster Array at RIBF
2. Radioactive Ion Beam Factory

— Due to the light and thin production target used, the energy of the produced beam is close to the primary beam's, allowing high-energy secondary reactions [33].
— The process is fast and no extraction from the target is required.
— Unlike ISOL, the in-flight method is not constrained by physico-chemical properties of the element produced [34].

The fast process along with the high velocity of the secondary beam gives access to probing short lifetimes.

2.1.2 Primary beam acceleration

The overall primary beam acceleration scheme is depicted in figure 2.1. First a ^{238}U primary beam is accelerated using a LINAC [3] (RILAC [4] up to 2.5 AMeV) and the RIKEN Ring Cyclotron (RRC). Two room-temperature ring cyclotrons (fRC [5], IRC [6]) and one superconducting cyclotron (SRC) [35] achieve the main acceleration stage boosting the primary beam energy up to 345 MeV/u for heavy nuclei [36]. Two stripping stages achieve a highly charged state for uranium ions and ensure the primary beam ions have a sufficient charge state for cyclotron accelerations [37]. At the end of the acceleration stage, the ^{238}U intensity is of the order of 60 pnA (3.7×10^{11} pps).

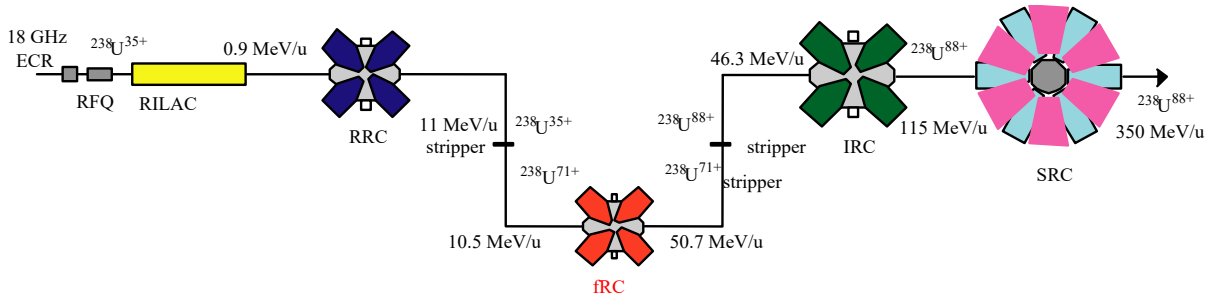

Figure 2.1 – Schematic view of the acceleration procedure at RIBF. Adapted from [38].

This primary beam impinges on a 4-mm thick primary production target made of beryllium at the entrance of the BigRIPS two-stages separator, thus producing a large range of nuclei by in-flight fission and projectile fragmentation.

3. Linear accelerator
4. RIKEN heavy ion LINAC
5. fixed energy Ring Cyclotron
6. Intermediate stage Ring Cyclotron

2.2 BigRIPS and ZeroDegree spectrometers

2.2.1 General layout

The beam line used for our experiment is composed of three main regions:

— The BigRIPS spectrometer: secondary beam purification and event-by-event identification.

— The secondary target area: nucleon knockout reaction and γ-ray spectroscopy.

— The ZeroDegree spectrometer: reaction product identification.

As shown in figure 2.2, the BigRIPS spectrometer is comprised between focal plane F1 and focal plane F7 ($\approx$ 78.2 metres). It is a two-step separator composed of six dipoles and fourteen superconducting triplet quadrupoles. The purification of the secondary beam is achieved by two consecutive $B\rho - \Delta E - B\rho$ selections[7], around focal planes F1 and F5. Each of these steps is performed using a combination of two dipoles, slits and a wedge-shaped aluminium degrader. A global time of flight over the whole spectrometer is measured between between plastic scintillators located at F3 and F7. The momentum acceptance around its centred rigidity is $\pm$2.5 %.

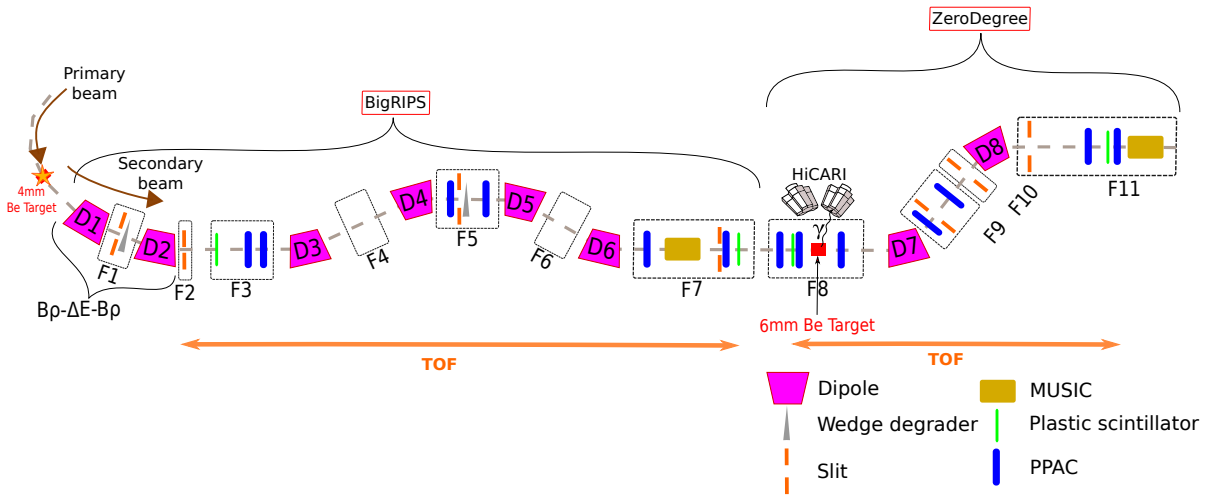

Figure 2.2 – Schematic layout of the BigRIPS and ZeroDegree spectrometers.

The secondary target area is located near the F8 focal plane (right at the exit of the BigRIPS spectrometer). It is the region where the secondary cocktail beam (here containing ^{84}Ge and ^{82}Zn) hits our 6-mm thick beryllium target to induce the nucleon removal reactions of interest. Three pairs of PPAC detectors, two before the target and one after, measure incoming and outgoing trajectories of the ions. The HiCARI array surrounds the reaction

7. define in section 2.2.2

target to detect γ rays emitted in flight by the reaction products. More details on the positioning of the various detectors around F8 and their configuration will be given in section 2.3.4.

Finally between F8 and F11, the ZeroDegree spectrometer achieves reaction product identification and allows their momentum analysis.

2.2.2 Separation and momentum achromat principle

Concept

The separation principle in the first stage of BigRIPS is based on the $B\rho - \Delta E - B\rho$ method [39]. The trajectory of the ions in a constant magnetic field B is described by their magnetic rigidity $B\rho$ defined as follows:

$$B\rho = \frac{p}{Q} = \frac{\gamma m v}{Q} = \gamma\beta\frac{Au}{Qc}\,, \tag{2.1}$$

where ρ is the radius of curvature of the trajectory, Q is the ion's charge ($Q \leq Z$), $m = Au/c^2$ and $u \approx 931.5$ MeV, c is the speed of light, $\beta = v/c$, and $\gamma = (1-\beta^2)^{-1/2}$ [6].

Since secondary ions produced *via* in-flight fragmentation and fission have similar velocities (β), nuclei with different mass-to-charge ratio (A/Q) can be separated by their magnetic rigidities.

In practice, the first bending dipole D1 performs this first A/Q separation of the fragments and sends the unreacted primary beam to a dump. Even if most ions are fully stripped ($Q = Z$) due to the high beam energy, there are still different possible values of Z leading to the same A/Q. Therefore a degrader is placed at the dispersive F1 focal plane after the dipole making isotopes lose energy depending on their Z value according to the Bethe-Bloch formula. These differences in energy loss will result in ions with different Z having different rigidities even if they have the same mass-to-charge ratio. Following this degrader, another dipole magnet (D2) is used to perform this second magnetic rigidity separation.

Thanks to this combination of elements and the wedge shape of the degrader (see reference [40]), the horizontal position of an isotope in the focal plane F2 depends on its nature (A, Z) but not on its momentum (momentum achromaticity). Consequently a set of horizontal slits in this plane is adjusted to mainly select the isotopes of interest.

This $B\rho - \Delta E - B\rho$ selection is performed around the two main momentum dispersive planes in BigRIPS:

— Between F0 and F2 with dipoles D1 and D2 and a 8 mm aluminum wedge degrader.

— Between F4 and F6 with dipoles D4 and D5 and a 2 mm aluminum wedge degrader.

RIBF196 experimental settings

The central rigidity chosen for the tuning of BigRIPS had to be a compromise to ensure optimum transmission for three isotopes ^{84}Ge, ^{83}Ga, and ^{82}Zn. ^{82}Zn is the most exotic and has the lowest production rate (270 times less than ^{84}Ge). In consequence, the BigRIPS spectrometer magnets were centred on it to maximise transmission. The resulting composition of the secondary beam is shown in table 2.1 below. The expected intensities of ^{84}Ge, ^{83}Ga, and ^{82}Zn reaching the secondary target are respectively 5700 pps, 740 pps, and 21 pps with energies of about 261 MeV/nucleon, 255 MeV/nucleon, and 265 MeV/nucleon respectively.

Element	Percentage in secondary beam
^{84}Ge	74.18 %
^{83}Ga	8.71 %
^{85}Ge	6.48 %
^{82}Ga	4.71 %
^{83}Ge	4.16 %
^{82}Zn	0.20 %

Table 2.1 – Proportion of elements in secondary cocktail beam.

For the tuning of the ZeroDegree spectrometer, the counting rates in three main channels had to be optimised, ^{84}Ge$\rightarrow^{83}$Ge, ^{82}Zn$\rightarrow^{81}$Zn, and ^{83}Ga$\rightarrow^{82}$Zn (channel of interest for collaborators). The main difficulty is to transmit most of the momentum distribution especially at the dispersive focal plane F9.

As shown in figure 2.3a, the energy distribution of beam nuclei on target is peaked towards lower energies, and sharply cut due to momentum slit selection. After reaction and transmission in ZeroDegree, we show in figure 2.3b the extrema of the position along the X-axis in F9 for the three reaction products of interest as predicted by LISE++ calculations (centred on ^{81}Zn). Black dots represent the maximum of the distribution, and bars their extrema. The dashed lines represent the interval within which the transmission is 100%, after that, losses occur until the acceptance limit represented by horizontal solid lines.

Experimentally, the ^{81}Zn rate is too low to directly align the spectrometer's rigidity on it. Therefore we first aligned on the unreacted ^{82}Zn in ZeroDegree. The measured X position in F9 obtained as a result is shown by the blue points in the figure. All three nuclei are transmitted but the low-energy part of the ^{83}Ge distribution was partly cut. Given that the spectroscopy of ^{83}Ge is the main goal of the experiment, we decided to offset ZDS by -2% (green dots in the figure) to avoid this loss at the cost of losing only a fraction of ^{82}Zn.

The final settings of dipole rigidities and slits are listed in tables 2.2 and 2.3. The

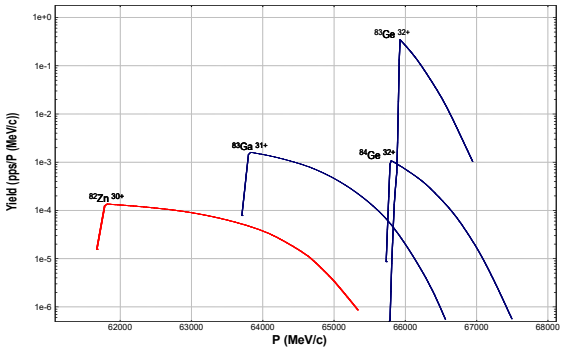

(a) Shape of the momentum distribution according to LISE++ simulations.

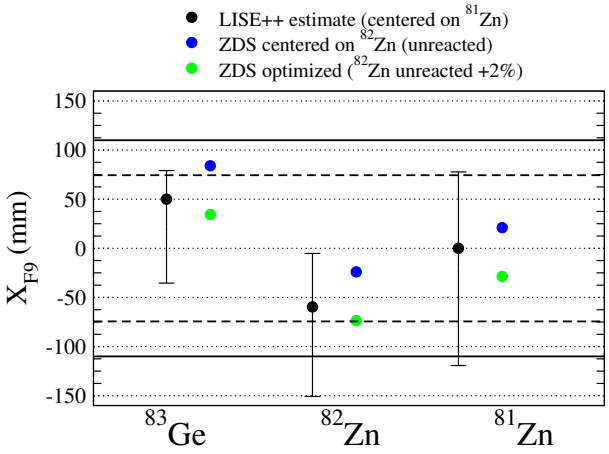

(b) Centroids of the momentum distributions for three different species in F9. Black dots are LISE++ estimates prior to data runs and error bars enclose 90% of the distribution. Colored dots are experimental measurements for two different centre rigidities in ZeroDegree.

Figure 2.3

overall momentum acceptance in BigRIPS is 5.5 %.

Dipole	D1	D2	D3	D4	D5	D6	D7	D8
$B\rho$ (T.m)	7.9677	7.0944	7.0663	7.0658	6.8037	6.8039	5.9429	5.9380

Table 2.2 – Tuning of the BigRIPS and ZeroDegree spectrometers dipoles.

Focal plane	F1	F2	F5	F7	F9	F10
Left opening (mm)	53.50	2.00	110.00	35.00	120.00	120.00
Right opening (mm)	64.20	6.00	110.00	35.00	120.00	230.00

Table 2.3 – Slit opening values used for RIBF 196.

2.2.3 Particle Identification Diagram (PID) production

The identification of the nuclei in both the second stage of BigRIPS and in the ZeroDegree spectrometer is based on their mass-over-charge ratio (A/Q) and atomic number (Z, that here corresponds to the charge of the fully stripped ions). Those features are deduced from the measurement of the time of flight (TOF), energy loss (ΔE), and magnetic rigidity ($B\rho$) [41]. The identification is performed event by event and its conceptual steps will be described in this section in order to introduce further the necessary detection systems.

$B\rho$ determination

In a magnetic spectrometer, the transport of ions from a focal plane to another can be described using an optical transfer matrix. For example in BigRIPS, at first order between F5 and F7 we have the relationship:

$$\begin{pmatrix} X_{F7} \\ A_{F7} \\ Y_{F7} \\ B_{F7} \\ \delta \end{pmatrix} = M_{5-7} \times \begin{pmatrix} X_{F5} \\ A_{F5} \\ Y_{F5} \\ B_{F5} \\ \delta \end{pmatrix} , \tag{2.2}$$

where X, A and Y, B denote the position and angle in the dispersive and non-dispersive planes, respectively, and M_{5-7} the optical transfer matrix between focal planes F5 and F7 discussed more in details below. The variable δ corresponds to the relative variation of momentum (or rigidity) with respect to the central value set for the spectrometer ($B\rho_0 = p_0/Q$). In other words:

$$\delta = \frac{\Delta p}{p_0} = \frac{\Delta B\rho}{B\rho_0} \tag{2.3}$$

Each phase-space parameter in the final plane is thus related to the initial phase-space parameters. For example in the case of X_{F7}:

$$X_{F7} = f_{7x}\left(X_{F5}, A_{F5}, Y_{F5}, B_{F5}, \delta\right) \tag{2.4}$$

A first order Taylor expansion shows that for a given parameter in the final state of the beam, the dependency on each initial beam parameter is a partial derivative [42]. For convenience the partial derivatives are written as:

$$\begin{aligned} (x|x) &= \frac{\partial f_{7x}}{\partial X_{F5}}\Big|_{F7} \\ (x|a) &= \frac{\partial f_{7x}}{\partial A_{F5}}\Big|_{F7} \\ &\dots \end{aligned} \tag{2.5}$$

This gives with the example of X_{F7} and A_{F7}:

$$\begin{aligned} X_{F7} &= (x|x)X_{F5} + (x|a)A_{F5} + (x|y)Y_{F5} + (x|b)B_{F5} + (x|\delta)\delta \\ A_{F7} &= (a|x)X_{F5} + (a|a)A_{F5} + (a|y)Y_{F5} + (a|b)B_{F5} + (a|\delta)\delta \end{aligned} \tag{2.6}$$

Assuming no coupling between the two planes (X, A) and (Y, B) (anti-symmetric

magnetic fields), the "cross-plane" dependencies are null:

$$\begin{aligned}(x|y) &= (y|x) = 0\\ (x|b) &= (b|x) = 0\\ (a|y) &= (a|y) = 0\\ (a|b) &= (b|a) = 0\end{aligned} \tag{2.7}$$

The chromatic terms corresponding to the (Y, B) plane (dispersion $(y|\delta)$, and angular dispersion $(b|\delta)$) are null since it is non-dispersive.

Using all the conditions, the optical matrix M_{5-7} is a 5×5 transfer matrix of the form:

$$M_{5-7} = \begin{pmatrix} (x|x) & (x|a) & 0 & 0 & (x|\delta) \\ (a|x) & (a|a) & 0 & 0 & (a|\delta) \\ 0 & 0 & (y|y) & (y|b) & 0 \\ 0 & 0 & (y|y) & (y|b) & 0 \\ 0 & 0 & 0 & 0 & 1 \end{pmatrix} \tag{2.8}$$

Between F3 and F5, the transfer matrix is of the same type but the values of individual coefficients differ (to restore achromaticity in F7).

To extract the rigidity of each ion experimentally from the measured trajectories in F5 and F7, we combine the two expressions in equation 2.6 to express the δ parameter as a function of X_{F7}, A_{F7}, X_{F5}, and matrix elements alone:

$$\delta = \frac{(a|a)X_{F7} - (x|a)A_{F7} - ((x|x)(a|a) - (x|a)(a|x))\,X_{F5}}{(a|a)(x|\delta) - (x|a)(a|\delta)} \tag{2.9}$$

The rigidity of the particle is then found from equation 2.3:

$$B\rho = B\rho_0(1+\delta) \tag{2.10}$$

The nominal first-order optical matrix elements used in the analysis are provided by the local operators but in a spectrometer with high-momentum acceptance there are also non-negligible high-order terms coming into play. Those higher order terms impact the resolution in $B\rho$ and hence in A/Q, and they need empirical correction that will be described in section 3.1.3.

Beta measurement

Using the known distance ΔL between two focal planes and measuring the time of flight (TOF) of a beam ion between these planes, one can compute event-by-event a mean ion

velocity $\beta = \frac{\Delta L}{c \times TOF}$. However this mean velocity includes in average all energy losses in materials along the line between the two detectors used to measure the time difference (in our case two thin plastic scintillators in F3 and F7 for BigRIPS). In the presence of a thick degrader between the two plastic detectors (like in our case in F5, see figure 2.2), such a mean velocity cannot be used because it differs too much from the ones before or after the degrader needed in later stages of the analysis. Therefore the so-called "two-fold" method [41] is used to extract the velocities in the different sections of the spectrometer by combining the total TOF measurement with the magnetic rigidities extracted in each section.

In this method, the total time of flight between the two plastic detectors is decomposed using:

$$TOF = \frac{L_1}{\beta_1 c} + \frac{L_2}{\beta_2 c}, \tag{2.11}$$

where 1 and 2 respectively denote variables before and after the degrader. $L_{1,2}$ corresponds to the length between each plastic detector and the degrader, and $\beta_{1,2}$ is the actual mean velocity in the corresponding portion of the spectrometer.

As long as there is no change of charge state along the spectrometer path, the mass-to-charge ratio of a beam ion stays the same. Therefore, we can express the A/Q in each portion:

$$\frac{A}{Q} = \frac{B\rho_1 \times c}{u\beta_1\gamma_1} \text{ and } \frac{A}{Q} = \frac{B\rho_2 \times c}{u\beta_2\gamma_2} \tag{2.12}$$

Taking the ratio between these last two equations, we get:

$$\frac{B\rho_1}{B\rho_2} = \frac{\beta_1\gamma_1}{\beta_2\gamma_2} \tag{2.13}$$

Substituting equation 2.13 into equation 2.11 either β_1 or β_2 can be determined as a function of the measured lengths and rigidities.

Production of the particle identification diagram (PID)

In our analysis, the nuclei will be unambiguously identified event-by-event using the mass-to-charge ratio A/Q and the charge number Z.

On one hand, the A/Q ratio is extracted for each portion of the spectrometer (before and after the degrader: between F3 and F5, and between F5 and F7) by using the event-by-event $B\rho$ and β determined as described in the previous section:

$$\frac{A}{Q} = \frac{B\rho \times c}{u\beta\gamma} \tag{2.14}$$

On the other hand, the Z value can be determined by measuring the energy deposited in

a detector placed along the beam's path (in our case ionisation chambers labelled MUSIC in figure 2.2) and then using the Bethe-Bloch formula:

$$(\ln\left(\frac{2m_ec^2\beta^2}{I(1-\beta^2)}\right) - \beta^2) \times Z^2 = -\left[\frac{dE}{dx}\right]\frac{m_ec^2\beta^2}{4\pi n_e}\left(\frac{4\pi\epsilon_0}{e^2}\right) \tag{2.15}$$

where $\left[\frac{dE}{dx}\right]$ is the energy loss per unit of distance, m_ec^2 is the mass of the electron, and β is the velocity. Isolating the variable:

$$Z = \sqrt{\frac{\left[\frac{dE}{dx}\right]\frac{m_ec^2\beta^2}{4\pi n_e}\left(\frac{4\pi\epsilon_0}{e^2}\right)}{\ln(\frac{2m_ec^2}{I}\beta^2) - \ln(1-\beta^2) - \beta^2}} \tag{2.16}$$

This allows to produce a Particle Identification Diagram (PID) in Z vs A/Q (example in figure 2.4) and therefore identify event-by-event each nucleus in the cocktail beam in BigRIPS or among the knockout products in ZDS.

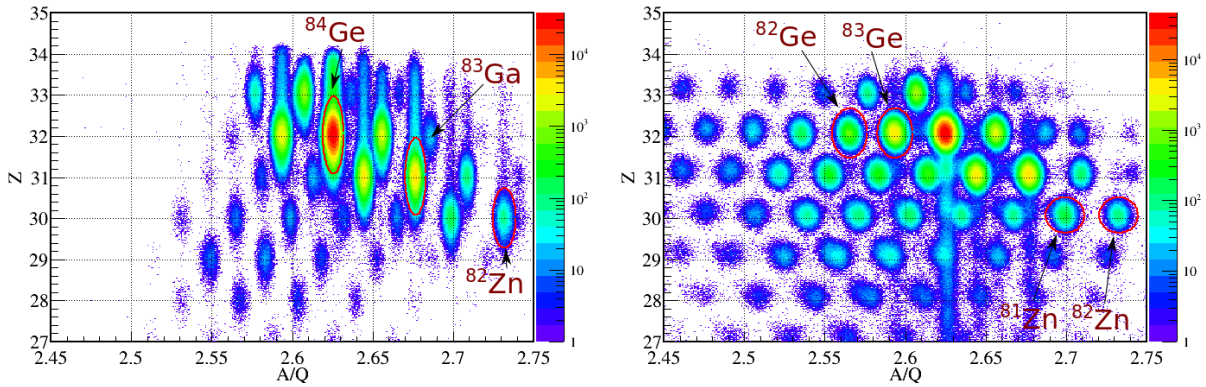

(a) BigRIPS **(b)** ZeroDegree

Figure 2.4 – Particle Identification Diagram (PID) in BigRIPS and ZeroDegree obtained during the experiment RIBF196. A treatment for event selection and optical corrections is already applied but will be detailed later in the section 3.1.2.

2.2.4 Beam line detectors

As explained conceptually in the previous section, the production of the PID (figure 2.4) relies on the measurement of three main types of observables:

— (X, Y, A, B) measured in the Parallel Plate Avalanche Counters that monitor the trajectories of the ions around specific focal planes (F3, F5, F7, F8, F9, and F11, see figure 2.2).

— Time of flight measured between two plastic scintillators.

— ΔE (the energy deposit in a given material) measured in the MUSIC Ionisation Chambers.

This section will briefly describe the functioning principle of those three types of detectors. The placement of the detectors can be seen on the scheme presented in figure 2.2.

Parallel Plate Avalanche Counters (PPAC)

Parallel Plate Avalanche Counter (PPAC) detectors are used to monitor the position of the nuclei in the transverse plane with respect to the beam axis.

As schematically shown in figure 2.5, a PPAC detector is composed of two segmented cathode planes connected to delay lines, an anode plane in between them, and is filled with gas at low pressure (C_4H_{10} or C_3F_8). When an ion passes, atoms in the gas get ionised and produce a fast electron avalanche (rise and fall times of few nanoseconds [43]) due to the strong electric field between the electrodes (around 700 V applied during the experiment and only 3-4 mm gap). These electrons induce charge signals on few strips of the cathodes around the ion trajectory. The position along the axis of segmentation is then determined by combining knowledge of the signal velocity and the time difference of the signal's arrival at either end of the delay lines. In our experiment, the two segmented cathode planes are oriented perpendicularly to each other in order to have X and Y coordinate measurements. The fast timing and low impact on the beam's quality [44] make those detectors a viable tool to monitor the high-rate beam position. At the RIBF, PPAC detectors are always paired in order to maximise efficiency and allow angle measurements. Their active surface varies along the line but can reach areas up to 240 mm by 150 mm, in the horizontal (X) and vertical (Y) direction respectively.

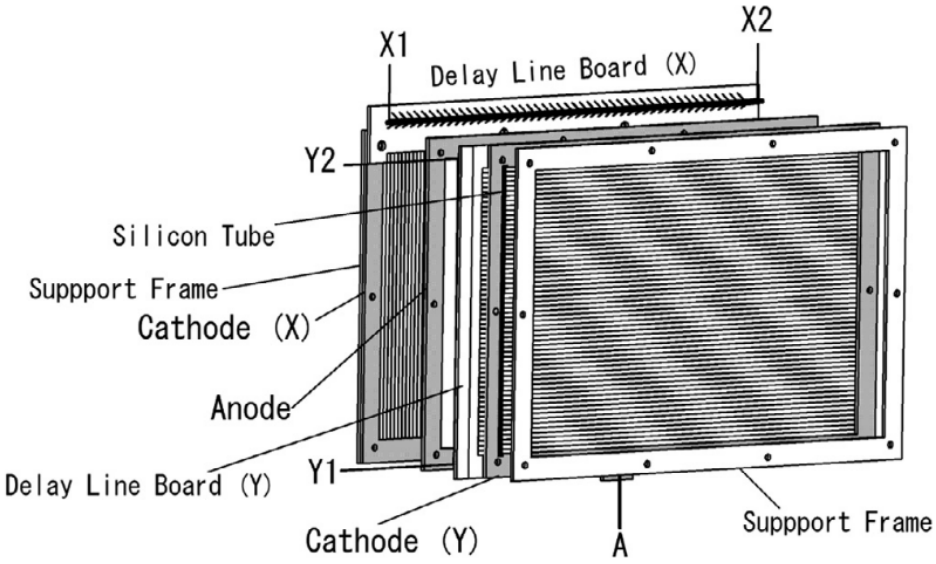

Figure 2.5 – Schematic view of a single PPAC detector. Taken from [43].

There are 26 Parallel Plate Avalanche Counters along the line. For each PPAC the raw data measured in a time-to-digital-converter (TDC) are the charge signal arrival time on the left and right side for each X and Y cathode planes, and the central anode time with respect to a common reference: T_L^X, T_R^X, T_L^Y, T_R^Y, T_A^Y (with L: left, R: right, A: anode). Time differences between left and right values are then converted to position along a cathode plane, for example:

$$X = x_{factor} \times \left(\frac{T_L^X - T_R^X}{2} \right) + X_{offset} \tag{2.17}$$

where x_{factor} (in mm/ns) describes the signal velocity along the delay line and X_{offset} (in mm) is an offset to position the PPAC in its plane according to measured central values (similarly for Y).

The final positions (X_{F_i}, Y_{F_i}) and angles (A_{F_i}, B_{F_i}) in a given focal plane i are then reconstructed by combining measurements from different PPAC sets around the focal plane. For example using only two PPACs, 1 and 2, and noting Z_F the Z position of the focal plane:

$$\begin{cases} X_F = X_1 + \dfrac{(X_1 - X_2)}{(Z_1 - Z_2)}(Z_F - Z_1) \\ Y_F = Y_1 + \dfrac{(Y_1 - Y_2)}{(Z_1 - Z_2)}(Z_F - Z_1) \\ \tan(A_F) = \dfrac{(X_1 - X_2)}{(Z_1 - Z_2)} \\ \tan(B_F) = \dfrac{(Y_1 - Y_2)}{(Z_1 - Z_2)} \end{cases} \tag{2.18}$$

Plastic detectors

The time-of-flight measurement needed for ion velocity β determination involves plastic scintillators emitting light when an ion passes through. There are four 0.2 mm thick plastic scintillators placed at focal planes F3, F7, F8, and F11. A photomultiplier is mounted on each side to measure a time and a charge: T_L, T_R, Q_L, Q_R. The time at which a particle hits the plastic is defined as the mean value between the left and right time measurements in order to eliminate the time of light propagation in the plastic: $T = (T_L + T_R)/2$.

The distance ΔL between two plastic detectors being known, the velocity can be calculated (see section 2.2.3 for the more complex case when there is a degrader between the plastics):

$$\beta = \frac{\Delta L}{c \times \Delta T} \tag{2.19}$$

The times-of-flight are measured between F3 and F7 (for BigRIPS), and between F8 and F11 (for ZeroDegree). The length between the F3 and F7 plastic scintillators is about

46.6 metres, and the total length of ZeroDegree is about 36.5 metres.

The time-of-flight measurement needs to be calibrated in order to account for the difference of signal travel time (wire length) from a plastic to another. This calibration is detailed in section 3.1.3.

The rise and fall times are of a few nanoseconds and the efficiency is assumed to be close to 100% which is why they are used for triggering the BigRIPS and ZeroDegree acquisitions.

Ionisation chambers

In order to identify the charge of the ions (method described in section 2.2.3) multi-sampling ionisation chambers (MUSIC) are used. They consist of six electrodes enclosed within low pressure CH_4 gas that will be ionised by the beam. The resulting electron-ion pairs are collected on the electrodes producing a signal proportional to the energy lost by the beam in the gas *via* the ionisation process [45].

The use of multiple electrodes allows a better resolution in ΔE to be reached ($\approx 2\%$). The signals from all electrodes are combined by computing a geometrical mean of all the charges registered:

$$\Delta E = \sqrt[6]{\prod_{i=0}^{6} Q_i} \tag{2.20}$$

These detectors have a rather slow rise time due to an electron drift time of about 2 μs [46] which leads to a large amount of pileup as it will be showed in section 3.1.2.

2.3 The HiCARI γ-ray detector

In beam γ-ray spectroscopy following direct reactions has been a major tool for structure studies of nuclei near the drip lines at the RIBF facility .

Up to now, most experiments focused on performing the first spectroscopy of even-even nuclei (2_1^+, 4_1^+, ...) produced with very low rates (down to a few particles per second). For this purpose, the DALI2 scintillator array [47] with its high γ-ray detection efficiency ($\sim 20\%$ full-energy photopeak around 1 MeV) has been particularly successful [6, 48].

However, its energy resolution of about 10% FWHM at 1 MeV is too large for the detailed spectroscopy of dense level schemes.

The HiCARI project (figure 2.10a) was developed in order to assemble various high purity germanium detectors, comprising highly segmented crystals thus improving the intrinsic energy resolution as well as the angular granularity. This section will first detail the conceptual improvements brought by HiCARI and the technical details of this setup at RIBF.

2.3.1 In beam γ-ray spectroscopy

The energy of a γ ray emitted in-flight by a given reaction product undergoes a Doppler shift in the laboratory frame. The strength of this shift depends on the velocity β and the angle θ_γ between the γ-ray direction and the velocity vector of the emitting nucleus. The relation between the intrinsic transition energy E_0 (rest frame of the nucleus) and the measured energy E_{lab} in the laboratory (observation frame) is given by:

$$E_0 = E_{lab}\frac{1-\beta\cos\theta_\gamma}{\sqrt{1-\beta^2}} \tag{2.21}$$

Because of the beam's relativistic velocity ($\beta \approx 0.6$), this Doppler shift is of very significant impact: at forward angles (towards $\theta_\gamma = 0\,\text{deg}$) the measured energy E_{lab} will be twice as large as the rest frame energy E_0, and half as large at backward angles ($\theta_\gamma = 180\,\text{deg}$).

The measurement of the θ_γ angle between the reaction residue and the photon uses ZeroDegree data for the beam's scattering angle, and HiCARI data for the angle of the photon with respect to the spectrometer axis.

Equation 2.21 implies that the overall energy resolution is impacted not only by the detector intrinsic resolution in E_{lab}, but also by the uncertainties on the velocity and the observation angle (also called Doppler broadening). One can express the attainable energy resolution after Doppler correction by:

$$\left(\frac{\Delta E_0}{E_0}\right)^2 = \left(\frac{\Delta E_{lab}}{E_{lab}}\right)^2 + \left(\frac{\beta\sin\theta_\gamma}{1-\beta\cos\theta_\gamma}\right)^2 (\frac{\Delta\theta_\gamma}{\theta_\gamma})^2 + \left(\frac{\beta-\cos\theta_\gamma}{(1-\beta^2)(1-\beta\cos\theta_\gamma)}\right)^2 (\frac{\Delta\beta}{\beta})^2 \tag{2.22}$$

Even if details about the analysis methodology and uncertainties will be given in section 2.3.3, we can summarise that:

— Velocity uncertainty $\Delta\beta$ originates mainly from both the imprecise knowledge of the beam ion velocity before the target (β_{in} deduced from BigRIPS in our case) and the unknown energy losses before the γ-ray emission point. When using a thick solid target, like our 6-mm thick beryllium target, this last effect dominates since we use the estimated mid-target velocity.

— Angular uncertainty $\Delta\theta_\gamma$ is due to (i) the unknown emission point within the target (similar effect as for $\Delta\beta$), (ii) the imprecise determination of the velocity vector ($\vec{v_{out}}$) of the outgoing reaction product emitting the γ-ray and (iii) the uncertainty on the γ ray hit position within the detector. In general, this last contribution dominates the angular uncertainty.

In figure 2.6, we illustrate quantitatively the contributions of these different uncertainties to the total energy resolution for a 1-MeV γ ray emitted at $\beta = 0.6$ and various detector

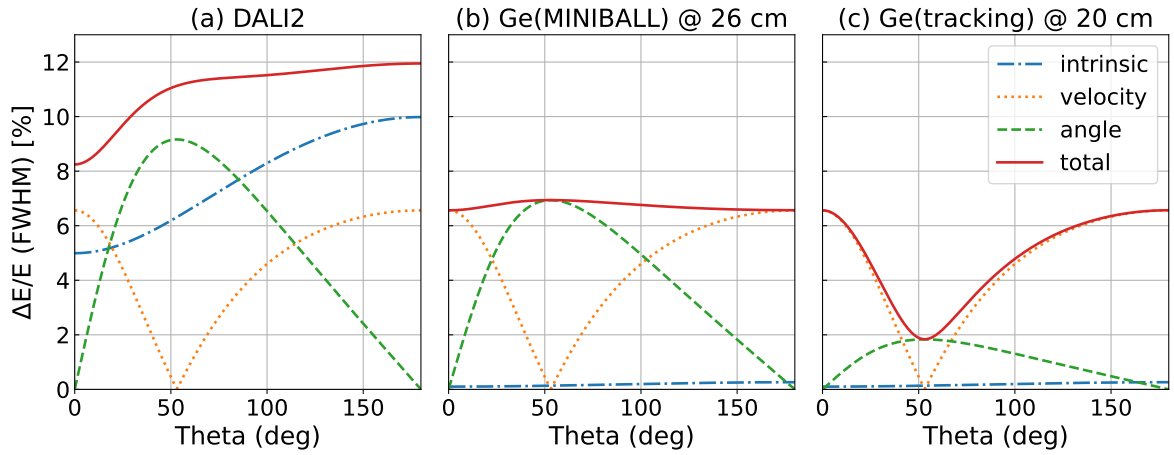

Figure 2.6 – Comparison of Doppler-corrected energy resolution (FWHM) as a function of the γ-ray emission angle θ_γ for different experimental setups (solid red lines). Individual contributions from different sources to the total uncertainty are displayed: angle $\Delta\theta$ (dashed lines), velocity $\Delta\beta$ (dotted lines), and intrinsic energy resolution ΔE_γ (dash-dotted lines). Panel (a) corresponds to the DALI2 scintillator array, (b) MINIBALL germanium detector at 26 cm, and (c) to state-of-the-art γ-ray tracking detector such as GRETINA/AGATA at 20 cm (see text for details).

setups: (a) the DALI2 array in nominal configuration, (b) segmented germanium detectors from MINIBALL [49] at 26 cm from the target and (c) state-of-the art Ge detectors from a tracking array at 20 cm.

Configuration (b) and (c) were chosen to mimic the configuration of Ge detectors in HiCARI detailed in next section. In all cases, a thick solid target (beryllium or carbon) inducing a $\Delta\beta/\beta$ of 7% was considered.

Naturally, the first obvious gain in resolution with the germanium detectors from HiCARI originates from their much superior intrinsic resolution compared to scintillators from DALI (2-3 keV compared to $\sim$ 100 keV at 1 MeV). Despite this significant intrinsic gain, the overall resolution remains limited in our configuration to about 6% for MINIBALL-like detectors because of the velocity uncertainty at low and high angles (due to the use of the thick target) and because of their limited angular segmentation dominating around 50 degrees (6-fold slices for a 7 cm diameter crystal). Finally, panel (c) demonstrates that detectors with pulse shape decomposition capabilities such as the GRETINA-type used in HiCARI can lead to an improvement of the total resolution down to 2% at some angles thanks to their 5 mm (FWHM) resolution in the γ-ray hit position.

2.3.2 Lifetime sensitivity

In the previous discussion, it was considered for simplicity that the γ-ray emission point coincides with the reaction vertex and in consequence that the mid-target point matches

with the average decay position. This assumption is correct only if the decaying state of the nucleus does not have a significant lifetime.

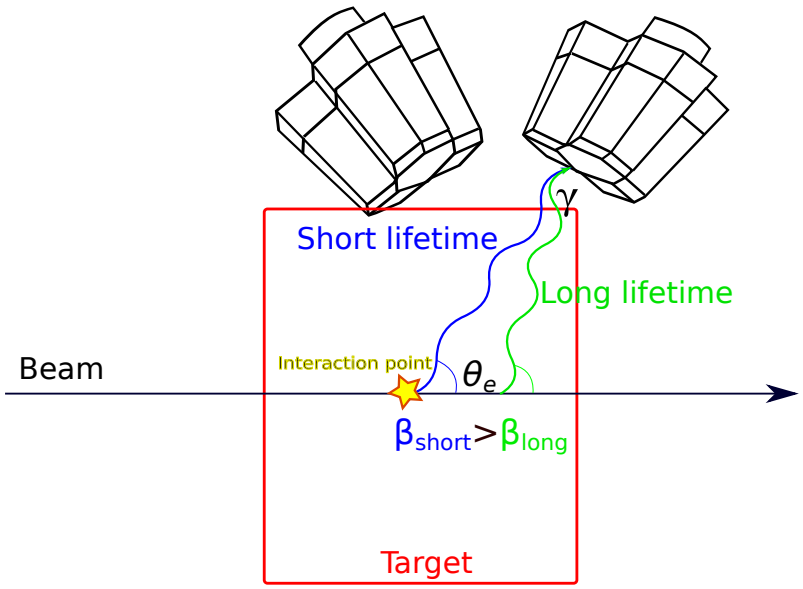

Figure 2.7 – Scheme of the lifetime effect on in-flight γ-ray detection. A long lifetime (in green) reduces the velocity at emission, and increases the emission angle of the γ ray.

As presented schematically in figure 2.7 a non-zero lifetime will make the average emission point deeper in the target (or even outside the target), thus reducing the average β at emission due to energy loss. Similarly, the mean θ_γ angle at emission will be increased by a non-zero lifetime.

These two effects induced by a non-zero lifetime will modify the position and shape of the photopeaks Doppler-corrected assuming a mid-target emission. In figure 2.8, simulations of the HiCARI detector's response for different lifetimes show that the mean energy of the Doppler-corrected photopeaks is shifted towards lower values compared to the actual transition energy, and a tail appears at low energy.

In our experiment, we actually use any observed energy shift and distortion of the peaks to determine the lifetime of the decaying state. To do so, a given experimental spectrum after Doppler correction is fitted using various simulated response functions assuming different lifetimes (as in figure 2.8). The goodness-of-fit (through a chi-square indicator for example) is then used to determine the lifetime with its error bar.

Having different kinds of detectors at different angles provides a better constraint on the lifetime since their response function is affected differently. For example, according to

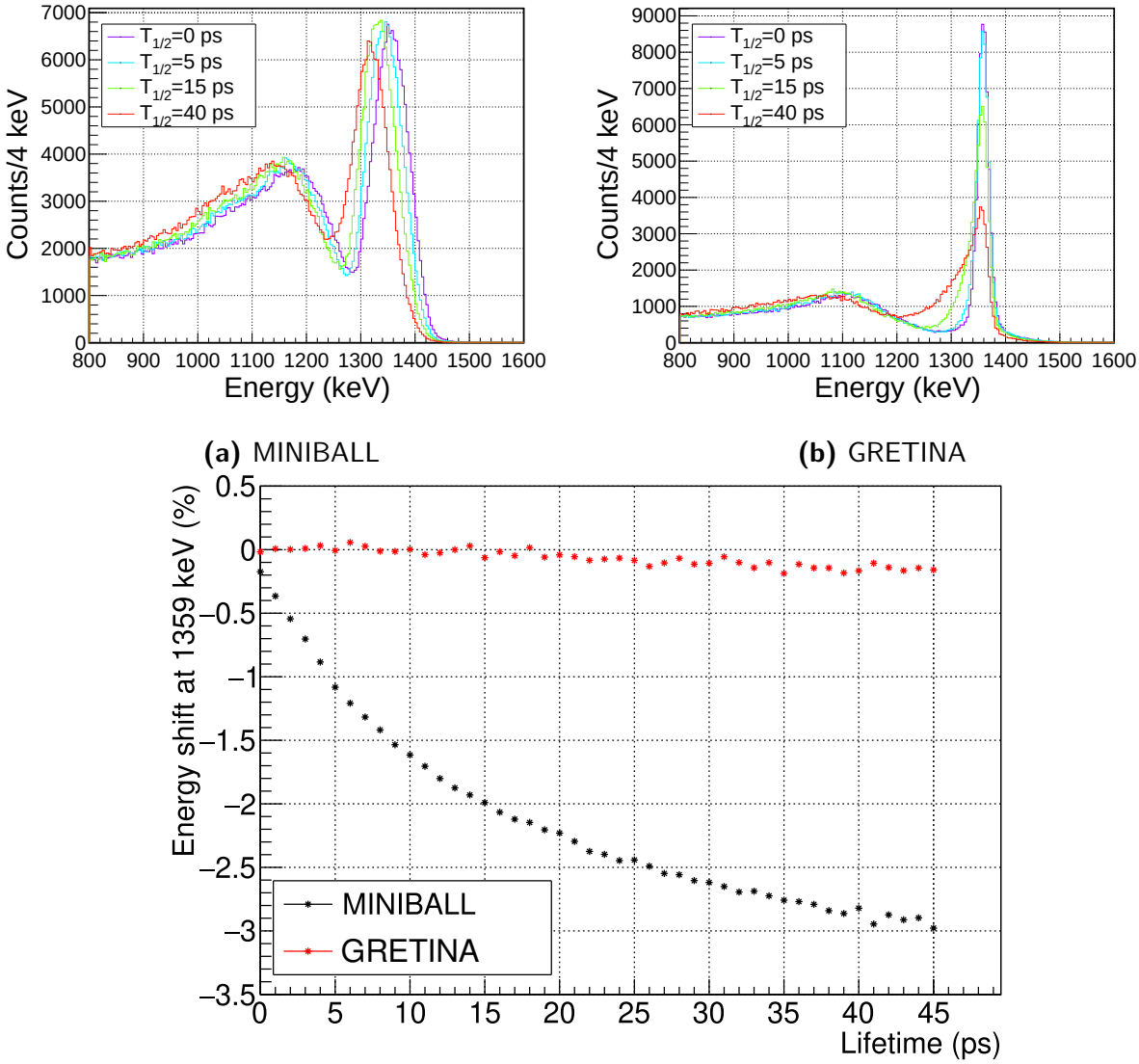

(a) MINIBALL **(b)** GRETINA

(c) Energy shift against half-life

Figure 2.8 – (a) and (b): Simulation of the sensitivity to lifetimes at 1359 keV for MINIBALL at low angles and GRETINA-like detectors at high angles. (c): Relative shift of the maximum of the peak as a function of the lifetime according to simulations. In black for detectors at low angles, in red for detectors at angles close to 70 deg.

equation 2.21, at an angle θ_γ for which:

$$\cos\theta_\gamma = \frac{1-\sqrt{1-\beta^2}}{\beta} \tag{2.23}$$

is fulfilled, the relativistic Doppler effect does not shift the γ-ray's energy (E_{lab}=E_0). Therefore at this angle (about 70 deg for $\beta \approx 0.6$) the energy shift due to a lifetime is very small.

An estimation of the peak's energy shift with respect to lifetime according to simulation of two groups of detectors described in the next section is presented in figure 2.8c. One can

observe that the peak position measured in GRETINA-like detectors is not shifted much. This shows the necessity at those angles to have a better Doppler reconstructed energy resolution in order to constraint the lifetime by analysing the peak trail.

At $\beta = 0.6$ a ^{83}Ge nucleus takes about 30 ps to travel through our 6-mm thick beryllium target. This means that for lifetimes longer than this, the main effect is caused by the mean θ_γ increase, since the velocity does not change anymore. Overall as it can be observed in figure 2.8, MINIBALL detectors have a good sensitivity to short lifetimes (of the order of a picosecond) since they induce a measurable energy shift (see figure 2.8c), and GRETINA-like detectors have a sensitivity to longer lifetimes (tens of picoseconds) due to their high angle (mainly from line-shape). This HiCARI multi-detector therefore provides a better sensitivity to level lifetimes than DALI2 thanks mainly to its superior energy resolution.

2.3.3 Overview of the array

Three types of detectors

The HiCARI γ-spectrometer is a multi-detector made of three different detector types. The final array that was used during our campaign comprised:

— 6 MINIBALL triple clusters [49] with tapered hexagonal crystals, each 6-fold segmented.

— 4 Super Clover detectors [50], each comprising four tapered 4-fold segmented crystals.

— A quadruple GRETINA detector (demonstrator) from RCNP and a triple GRETINA-like detector from LBNL Berkeley (referred to as "P3") both 36-fold segmented [51]. Both are referred to as GRETINA-type detectors.

The geometry of the crystals for each detector type and their segmentation are presented in figure 2.9, showing on the bottom the modelisation used for the Geant4 simulations (discussed in section 3.4).

The MINIBALL detectors are placed at rather low angles between 20 degrees and 50 degrees, the four Clover detectors are placed between 50 and 80 degrees, and the hexagonal-shaped GRETINA-type detectors are placed at high angles between 60 and 90 degrees. Figure 2.11 shows the angular position of all the segments of the MINIBALL and Super Clover detectors. The figure also shows as a histogram an example of the extracted positions of the hits in the GRETINA-type detectors. Two out of the four crystals in the RCNP quadruple detector were not working (which leaves two crystals).

The centres of all segments with respect to the target have been determined through a photogrammetry method that uses image treatment of photographs of the detector on which small targets have been attached (bright dots in figure 2.10a). Using a minimisation algorithm, every capsule is placed in the lab frame and using each detector design provided

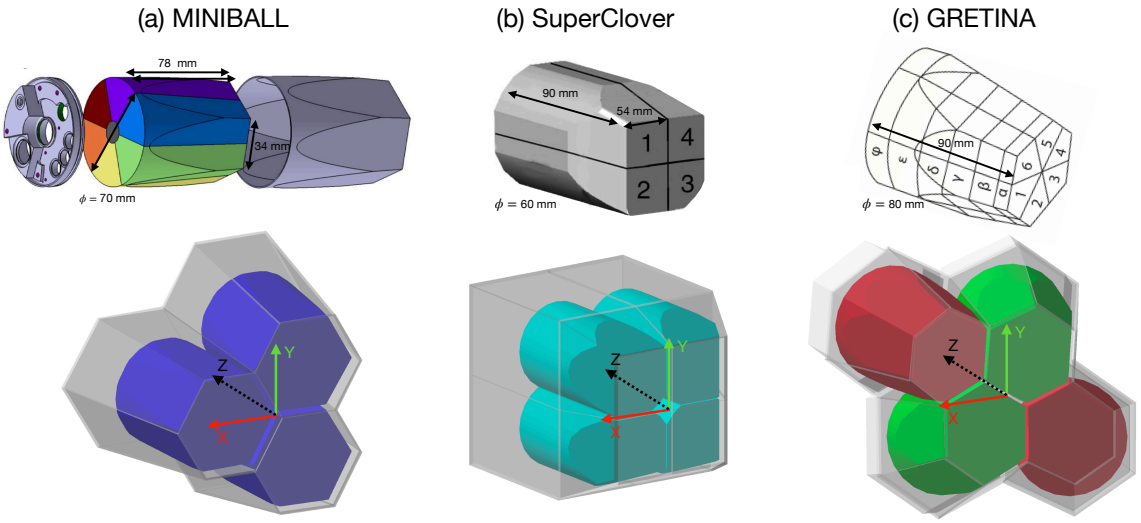

Figure 2.9 – Top: geometry of the crystals from MINIBALL, Clover, and GRETINA-like detectors. Bottom: view of the modelisation of a complete detector set.

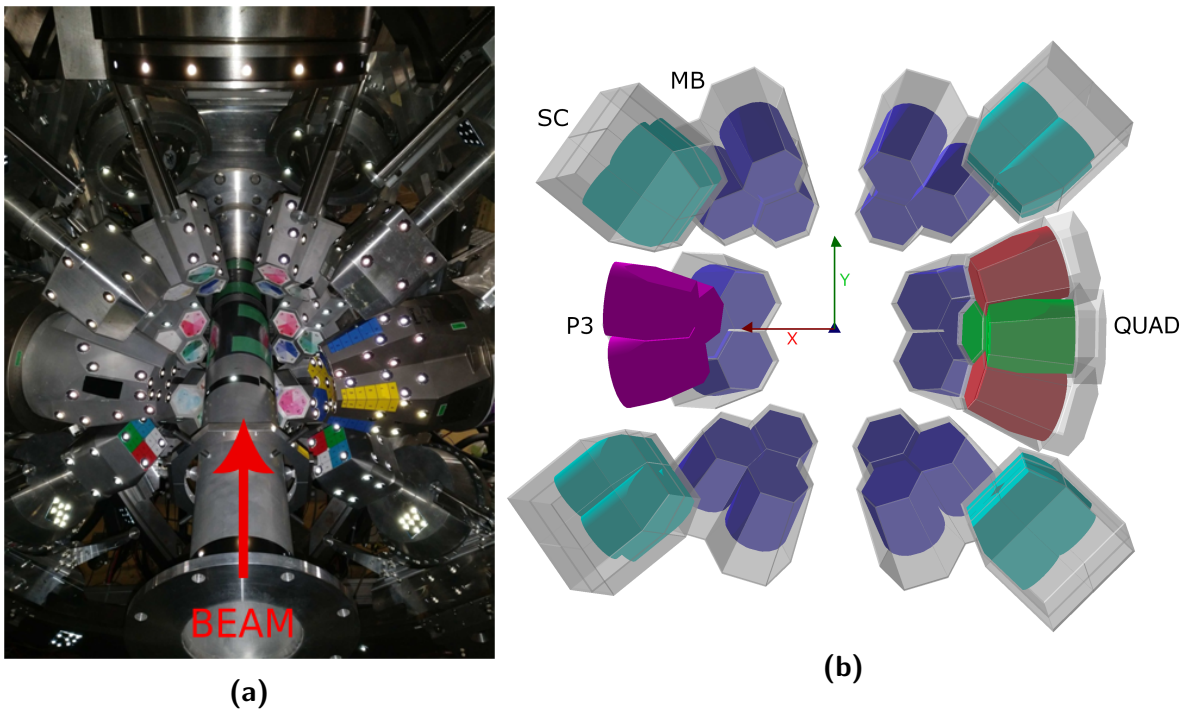

(a) **(b)**

Figure 2.10 – (a) Photograph of HiCARI around the F8 focal plane. (b) Position of detectors according to the CAD drawing.

by the constructor, the coordinates of the centres of the segments are determined. The results are presented in figure 2.11.

One can observe in figure 2.11 that some crystals are missing in MINIBALL and Clover

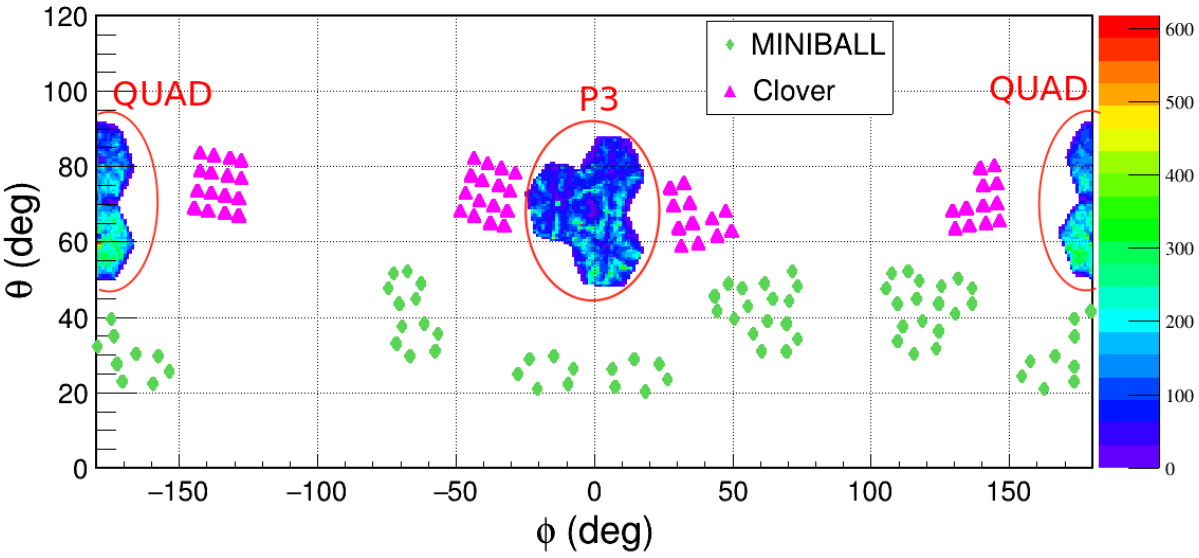

Figure 2.11 – Photogrammetry determined position of each segment in the lab frame.

clusters. In total for the MINIBALL detectors, a full cluster is missing (it would be at $\phi \approx -120\,\text{deg}$), and two crystals are missing from the clusters located at around $\phi \approx 0$ and $\phi \approx -70\,\text{deg}$. Among Clover-type detectors two crystals are missing from the clusters located at $\phi \approx 40\,\text{deg}$ and $\phi \approx 130\,\text{deg}$.

The acquisition is based on the GRETINA acquisition system designed to perform pulse shape decomposition (PSD) for the GRETINA-type detectors that will be described below.

The analogical signals from the crystal core and segments are sampled by a digitizer module using 14-bit ADC. A FGPA module then computes the energy by applying a trapezoidal filter [52].

Pulse shape decomposition

The high segmentation of the GRETINA-type detectors is used to determine the hit position of the γ ray in the crystal to a high precision. This section briefly describes the method to extract it.

The signal pulse shape (trace) of each segment is recorded and compared to a library (called the basis) relating the detector response pulses to the position of the hit in the detector.

In order to generate the basis, first the sum of a large number of single-segment events (called "super-pulse") is measured typically with a ^{60}Co source. This gives a typical signal in a given segment and induced signals in the neighbouring segments. An example of a "super-pulse" is given in figure 2.12 in red. The measured "super-pulse" is then fitted with about 996 parameters (taking into account cross-talk, rise time, crystal impurities, neutron

damage...) in order to obtain a set of parameters for each segment. Two examples of such a fit are shown in figure 2.12 (in green before parameter adjustment, and in blue after the fit).

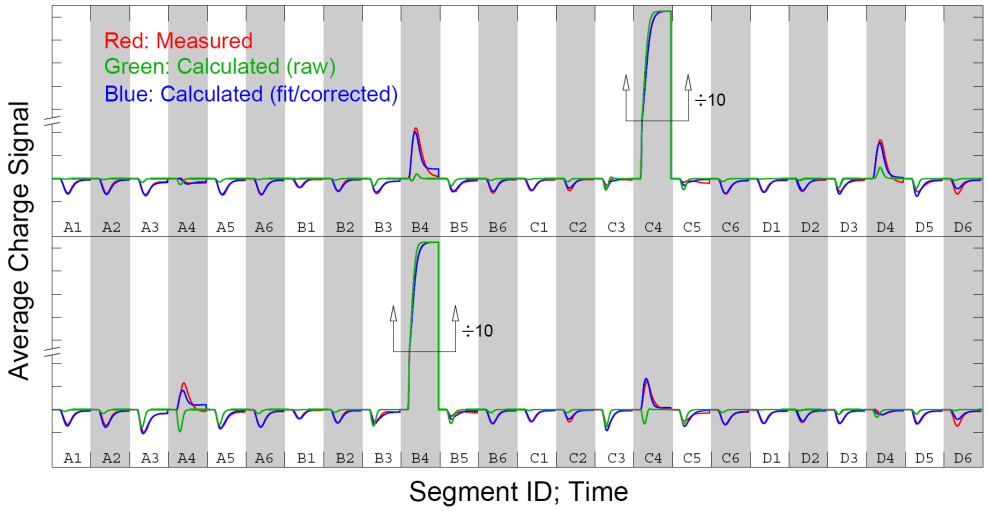

Figure 2.12 – Fitting of two "super-pulses" (in red). The Monte-Carlo simulation is used to generate a rough response function (green). The parameters of the final fit (blue) are used to produce the basis at each point of the grid. Extracted from [53].

The parameters determined through these fits are used to produce a set of simulated signals corresponding to a hit at each point of a grid within the crystal. The location of these grid points is optimised for a good compromise between precision and calculation time, see [54] for more details.

An optimal linear combination of each basis signal is then found *via* a least-squares fit. The linear combination is then used to estimate the location of the interaction point.

The coordinates of the hits in the detectors are determined thanks to this procedure with a precision of about 4 mm FWHM [55]. Without this procedure, the precision would have been the size of a segment.

2.3.4 Beam tracking setup

For γ-ray analysis purposes, beam tracking at the target must be performed. The two PPACs present before the target are used to measure the angle and the position of the incoming secondary beam on the target. A third PPAC has been inserted right after the target, thus allowing the measurement of the scattering angle θ_S.

The F8 focus is a beam focal plane that has been determined independently from HiCARI. The HiCARI position determined through photogrammetry is not defined with respect to the F8 focus and therefore a common reference point had to be found. The offset between the HiCARI reference frame and the centre of the target was measured to be 9.85 mm (using technical drawings inputs).

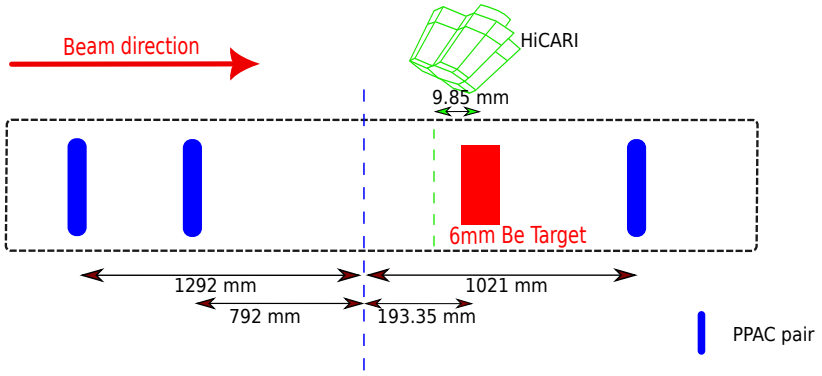

Figure 2.13 – Schematic view of the layout around the F8 focus. The dashed green line shows the Z-axis origin of the reference frame of HiCARI.

2.4 Data acquisition system and trigger

As mentioned previously, the GRETINA-type detectors use pulse-shape decomposition in order to determine the interaction point in the crystal. This requires an analysis of the signal pulses that was performed online.

Therefore the HiCARI spectrometer data were written to disk in two modes:

— "Mode 3": Written to disk directly from data acquisition. They contain the traces along with the raw data

— "Mode 2": The data flux collected is also sent to a software that performs the decomposition and writes a data file with positions from the decomposition stored.

All of the data storing types keep timestamps that are compared to the reference timestamp recorded by the BigRIPS acquisition in order to merge the data into a single file.

A summary of the analysis software flow is shown in figure 2.14.

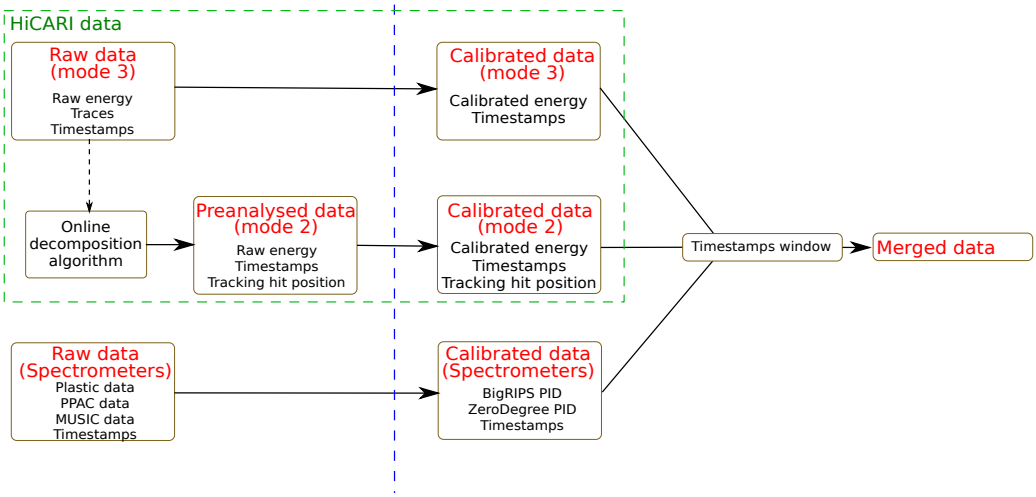

Figure 2.14 – Schematic view of the data analysis framework.

The total trigger condition is generated from the combination of several single triggers. Trigger signals care generated by plastic scintillators in F7 and F11 when they are hit. In the HiCARI acquisition, a γ-detector signal is used as a trigger signal if the energy passes a given threshold. The high beam intensity doesn't allow for a trigger condition simply relying on a hit in the plastic scintillator in F7 as the data acquisition would be flooded and we would have mostly dead time. In order to still have incoming beam monitoring, a downscaling factor of 10% is applied to the condition of a simple hit in the F7 plastic (third item below). This downscaling factor can be later compensated in the analysis.

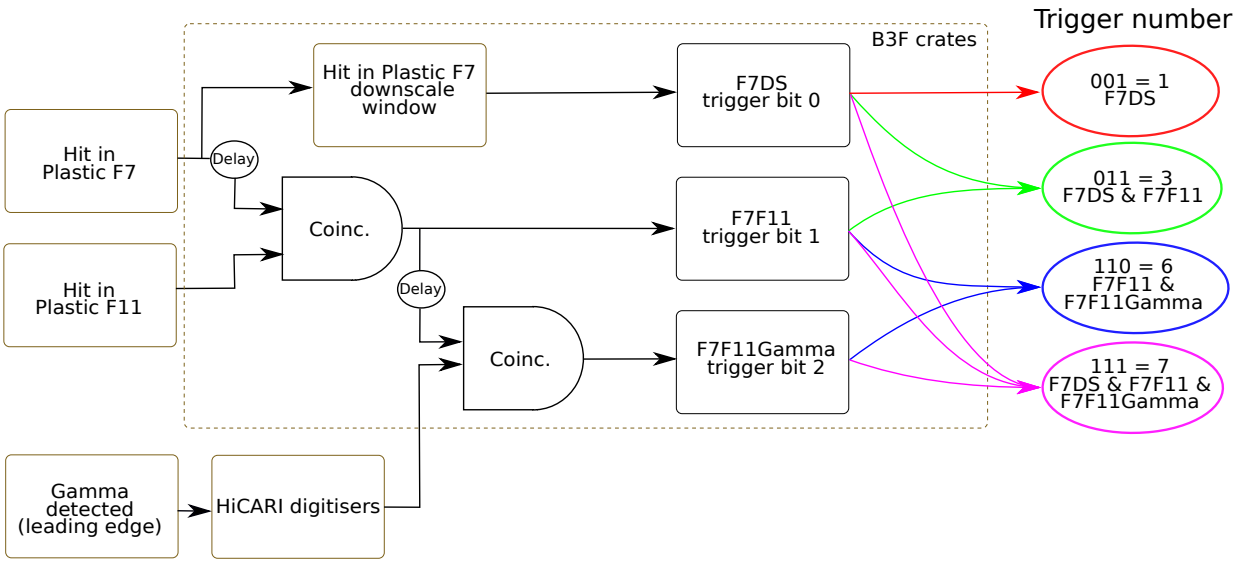

Figure 2.15 – Schematic view of the trigger processing.

The acquisition can be triggered by three different possible assertions:

— The plastic scintillators in F7 and F11 are hit, without requesting a detected γ-ray (trigger F7F11).

— The plastic scintillators in F7 and F11 are hit, and a γ-ray is detected (trigger F7F11Gamma).

— The plastic scintillators in F7 is hit and the event goes through the downscale window (10%) (trigger F7DS).

The second item is used for γ-ray analysis and the other two are used for cross-section and transmission measurements. Those three conditions are summarised in figure 2.15.

The three possible trigger types are combined into a three-bit binary number (on the right of figure 2.15). We could expect that this results in 7 possibilities (000 is excluded). However some possibilities are removed:

— The F7F11Gamma trigger bit never comes without the F7F11 trigger bit, hence removing the possibility $100 = 4$, and $101 = 5$.

— The rank-1 bit F7F11 is not encoded when alone, removing the $010 = 2$ possibility.

The remaining 4 possibilities can be plotted as an histogram shown for illustration in

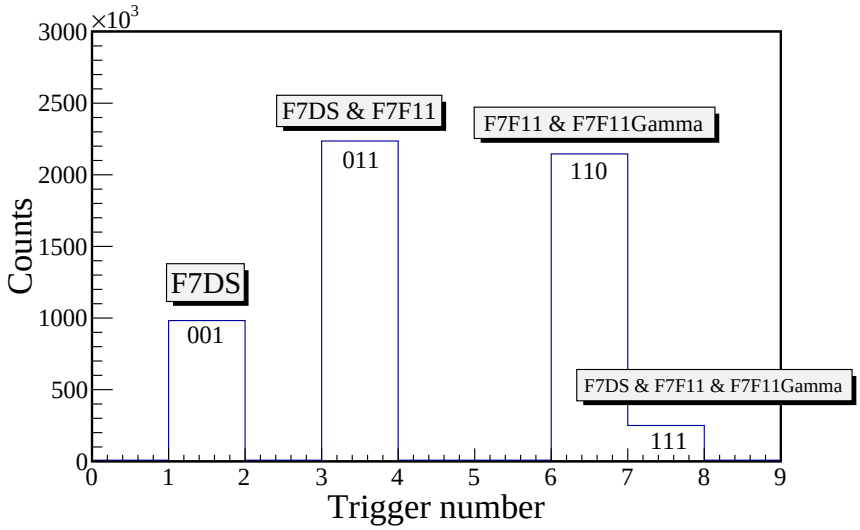

Figure 2.16 – Histogram of trigger types for an example run.

figure 2.16.

The gamma trigger boolean is created *via* a leading-edge discriminator timing signal. This timing is sent to the BigRIPS acquisition system that compares it to a window around its own timings. If there is a correspondence, a logical signal is sent back to the HiCARI digitisers in order to validate the data acquisition.

Since only plastic scintillators and γ-ray detectors are implicated in trigger conditions, the delay of the trigger is short. However the ionisation chambers being slow detectors (see next chapter for an estimation of the amount of pileup that they induce), they dictate the dead time for the acquisition thus becoming the limiting factor for the acquisition rate.

Chapter 3

Data analysis

This chapter provides a description of all the analysis steps performed to build the final Doppler corrected spectra for a given reaction channel. For the beam and reaction product identification, this includes first the removal of parasitic or erroneously reconstructed events *via* selection cuts but also the various calibrations involved and the optical corrections implemented to improve the A/Q and Z resolution. For the γ-ray analysis, the section includes both a characterisation of the HiCARI detectors with source data at rest (energy and time calibration, efficiency) and kinematic reconstruction (beam trajectory, velocity determination, γ-ray hit location) needed to perform Doppler correction. In the end, a section is dedicated to the GEANT4 simulation of the HiCARI response functions necessary to interpret the data of interest and more specifically how its parameters were tuned to match the experimental conditions.

3.1 Particle identification

As described in the previous chapter, the identification of the nuclei is obtained using the mass-to-charge ratio (A/Q) and the charge (Z). Due to unwanted reactions of the beam in the spectrometer or non-optimal detector responses, some events degrade the quality of the identification. This section will describe as well the procedure used to remove them.

3.1.1 PPAC analysis

The PPAC detectors are used for the reconstruction of the position and angles at each focal plane with the method described in section 2.2.3. For illustration, we show in figure 3.1 the trajectory reconstruction in all focal planes. One can observe the main dispersive planes: F5 in BigRIPS where the second stage separation is performed, and F9 in ZeroDegree.

When beam ions pass through a PPAC detector they can produce secondary electrons by knocking them out from atoms in the detector material (windows, electrodes or gas).

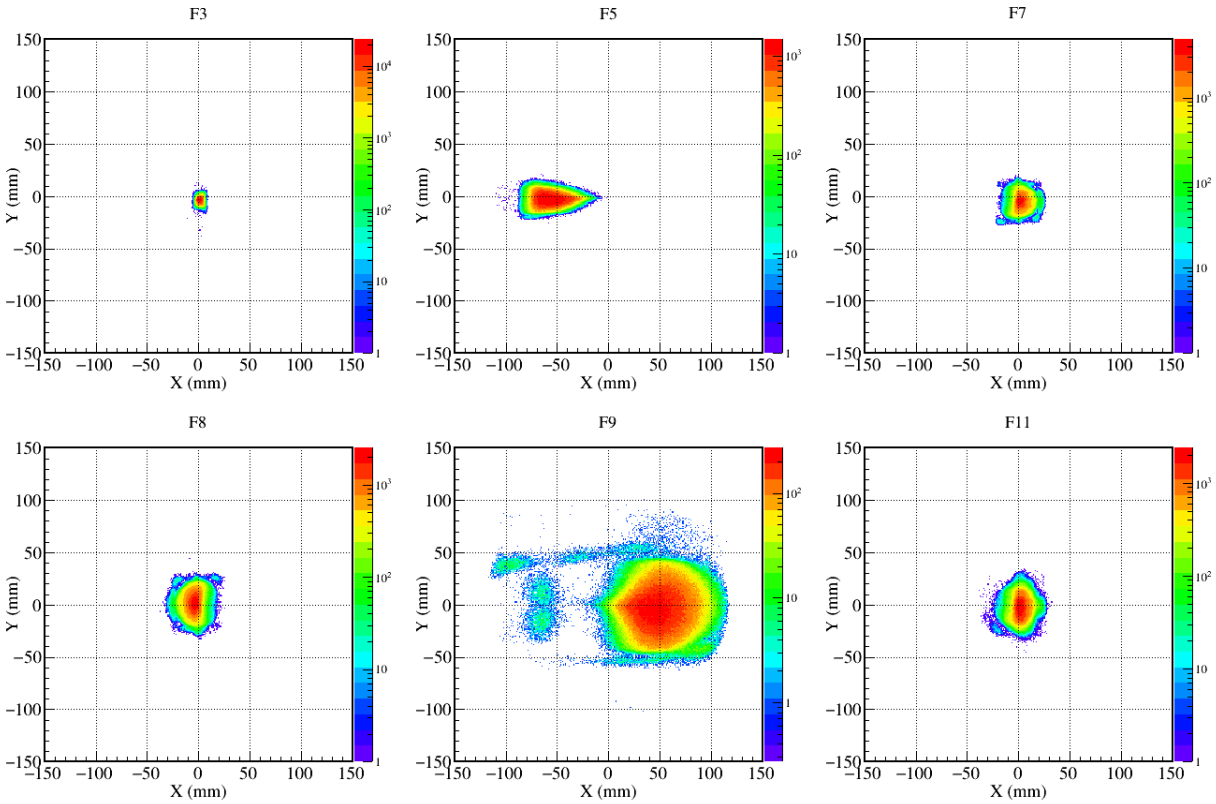

Figure 3.1 – X and Y positions in each focal plane for the ^{84}Ge→^{82}Ge channel. As discussed in the previous chapter, F5 and F9 are the dispersive planes, which is illustrated here.

These electrons, called delta electrons, can artificially enlarge the avalanche profile and consequently degrade the position reconstruction.

Fortunately, the delay line method allows a selection of such events using the total travel time along the full delay line. Indeed, the sum of the times measured on each side of the delay line (noted T_{sum} in the following) should be constant independently of the position of the ion since it depends only on the total length of the delay line. If a second event is collected at the same time, due to pileup or delta electrons produced within the PPAC, the delay-line end closest to the parasitic event will have a shorter recorded timing [43].

To filter out such events, we apply a condition on the T^X_{sum} and T^Y_{sum} variables defined as follows (for the X example):

$$T^X_{sum} = \left(T^X_L - T^A\right) + \left(T^X_R - T^A\right) \tag{3.1}$$

The time measured on the "anode" plane T^A is used as a reference time for each event.

A characteristic distribution is shown in figure 3.2. One can observe that the delta electron events cause a tail at lower T^X_{sum} or T^Y_{sum} on the variable's distribution. To select the window comprising proper events, a gaussian fit is applied on a range that starts at

half the maximum of the distribution on the left and extends widely on the right. All the events outside of the window defined by $\pm 3\sigma$ of the fitted gaussian are then dismissed.

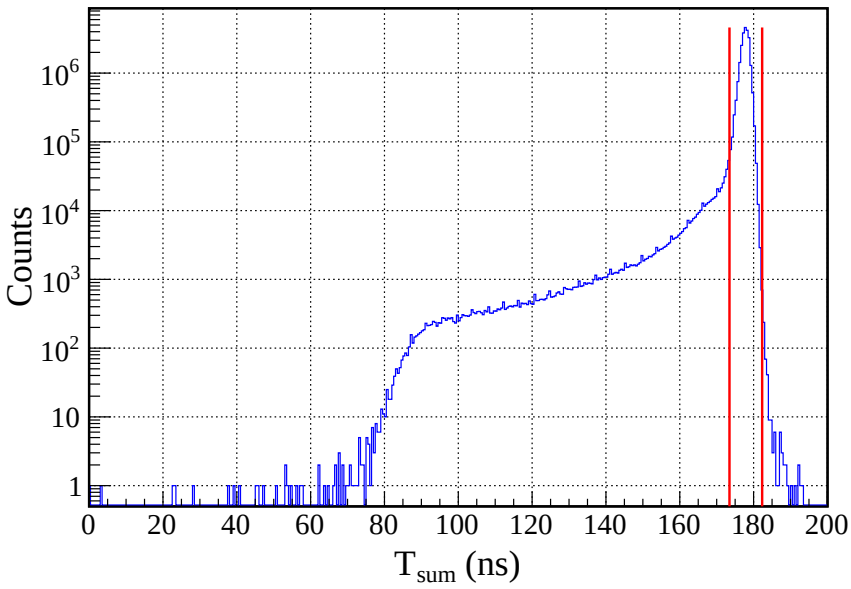

Figure 3.2 – Example of the removal of delta electrons in a PPAC detector on the X axis. The red lines delimit the window of accepted events in this case.

This selection was applied to 24 PPAC detectors out of the 26 in total on the experimental beam line and removes between 1% and 6% of the events for a given single plane. The two exceptions are F9PPAC-1B and F9PPAC-2A for which charge collection issues arose on the anode plane and therefore T_{sum} gates, requiring implicitly a proper anode time T^A, would heavily reduce their efficiency. Actually, this reduction is one of the features observed in figure 3.3 where all individual PPAC efficiencies are plotted. These efficiencies were calculated by comparing the number of hits in various PPAC variables (T_L^X, T_R^X or T_{sum}) to the number of hits in a plastic scintillator used as a reference (in our case the one placed at F7 used for the trigger). In summary, one can see that:

— Most of the individual PPAC efficiencies are above 90% indicating good working conditions.

— Requesting a proper T_{sum} value combining left, right and anode information decreases the individual efficiencies only by 1-2% in most cases.

— For the two PPACs with anode collection issues mentioned before (corresponding to ID 24 and 25), the efficiency calculated using T_{sum} is indeed of about 50% but an efficiency superior to 90% can be retrieved by using only T_L^X and T_R^X variables, confirming that the problem can be overcome and only originates from the anode time T^A.

— The first PPAC in the F3 focal plane (ID=5) malfunctioned. It was recurrently tripping during the experiment which caused a low detection efficiency, and hence

it was removed from our analysis.

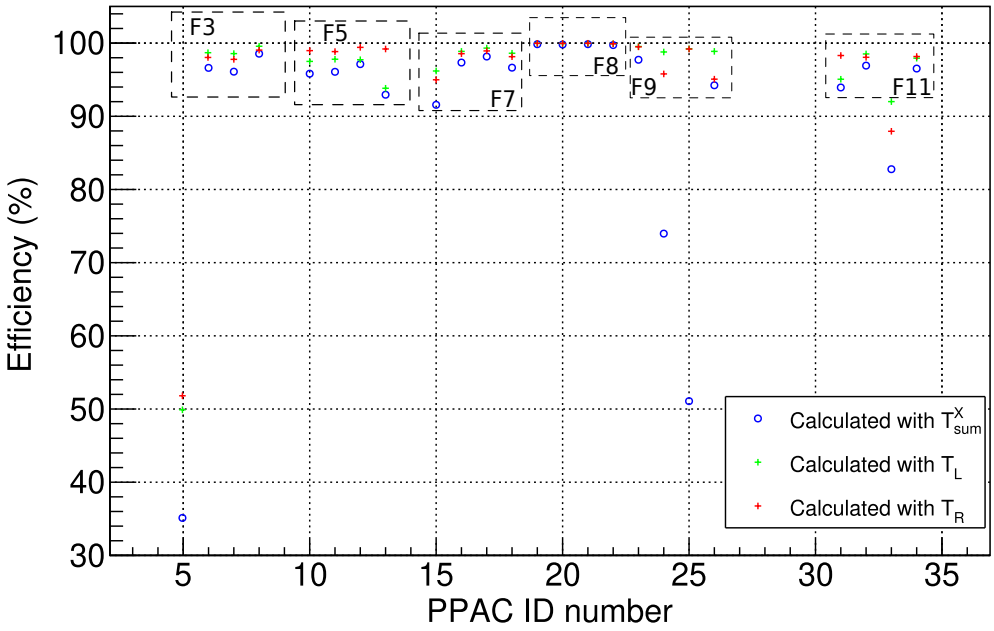

Figure 3.3 – Efficiency of each PPAC detector for different variables used as integrals. The blue circles show the efficiency calculated using the T_{sum} variables, and the green and red crosses show the efficiency obtained from individual left and right measured times.

Finally for reconstruction of trajectories in a given focal plane (described in the previous chapter), it is worth mentioning that only information from one PPAC plane is needed to measure a position (X, Y), and from two to measure an angle (A, B). Given that each focal plane has a minimum of 4 X and 4 Y planes (two double PPAC), applying individual cuts on each PPAC plane has little impact on the final trajectory reconstruction efficiency (the probability for suppressing or missing an event simultaneously in all PPAC planes becomes marginal). The impact of this background removal on the final reconstructed focal plane positions and angles is of about 1% in total. For illustration in the described experiment, the percentages of rejected events due to this T_{sum} selection are summarised in Tab 3.1 for the horizontal position and do not exceed 2%.

X_{F3}	X_{F5}	X_{F7}	X_{F8}	X_{F9}	X_{F11}
0.78%	1.16%	0.87%	0.74%	1.40%	0.93%

Table 3.1 – Proportion of the final reconstructed focal plane variable X rejected by the T_{sum} selection.

3.1.2 Event selection and background removal

Pileup events in ionisation chambers

The gas ionisation chambers have been preferred to semi-conductors in order to measure ΔE because the latter deteriorate rather quickly under beam irradiation [45]. Due to an electron drift time of the order of 5 μs [46] which is long compared to our experiment's beam rate, the response of the Multi-Sampling Ionisation Chambers (MUSIC) is quite slow. This induces a large number of pileup events that manifest on the PID, figure 3.5 (left), as a trail going to the higher Z values. A way to reject the pileup events is to check the correlation between the charge deposited in the ionisation chambers and the charge deposited in the plastic detectors, which are faster by several orders of magnitude (few nanoseconds). Such a plot is presented in figure 3.4 for the focal plane F7 (see further).

As already described, the plastic detectors are organic scintillators (C_9H_{10}) that are coupled to photo-multipliers on each end giving a signal on the right and on the left side. Their time measurement has already been discussed, here the charge measurement (based on the same principle) is used. A plastic scintillator oriented along the x axis will measure a charge on the "right" side Q_R (positive x) and a charge on the "left" Q_L (negative x) that are directly related through light attenuation to intrinsic and kinematic information of the incident ion [41]. They can be expressed as follows:

$$\begin{cases} Q_R = Q_0 e^{-\dfrac{L+x}{\lambda}} \\ Q_L = Q_0 e^{-\dfrac{L-x}{\lambda}} \end{cases} \tag{3.2}$$

Where x is the position of the particle, L is the length of the scintillator, λ is the attenuation length, and Q_0 is the signal corresponding to the full scintillation.

The total charge used for comparison with the one measured in ionisation chambers is the geometrical mean between left and right charges:

$$\begin{aligned} Q_{plastic} &= \sqrt{Q_L \times Q_R} \\ &= Q_0 e^{-L/\lambda} \end{aligned} \tag{3.3}$$

There are plastic detectors in F3, F7, F8, F9, and F11, and there are ionisation chambers only in F7 and F11. Therefore plastic detectors before the target (F8) are correlated with the ionisation chamber in F7 (BigRIPS), and the ones after F8 are correlated with the ionisation chamber in F11 (ZeroDegree).

Figure 3.4 presents the correlation between the energy measured in the ionisation chamber in F7 and the charge measured in the plastic scintillator in F7. The high intensity part

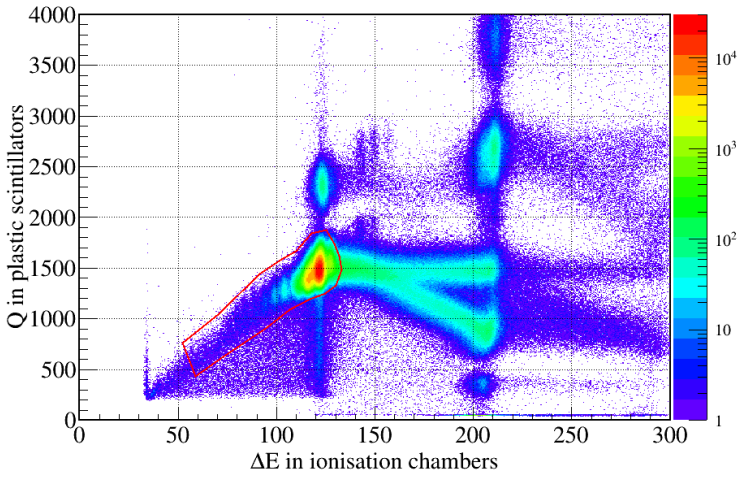

Figure 3.4 – Example pileup in scintillators and ionisation chambers placed in F7. The events selected are in the red graphical cut.

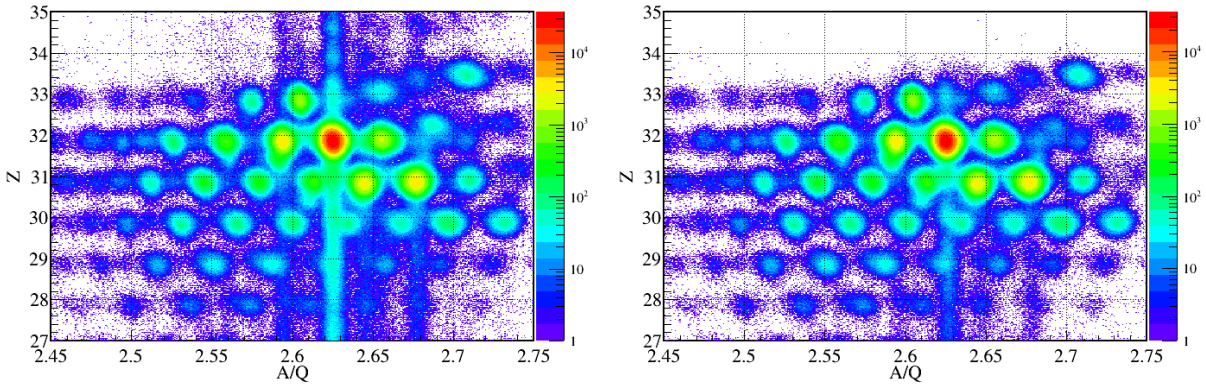

(a) Before pileup removal.

(b) After pileup removal.

Figure 3.5 – Illustration of pileup events removal for the ZeroDegree spectrometer. On the left before purification, on the right after purification.

($Q \approx 1500$ a.u. and $\Delta E \approx 120$ a.u.) corresponds to the energy/charge deposited by elements with a charge state of +32 which is most of our statistics. A diagonal from the bottom left of the diagram to the centre shows the expected correlation between the two variables. Some events form a trail along the X-axis (corresponding to the energy deposited in the ionisation chambers) starting from the diagonal to its right. They correspond to pileup events in the ionisation chambers. The *loci* when looking above $Q \approx 2000$ a.u. show that there are also some pileup events in the plastic detectors. Unlike for ionisation chambers pileup events, the shape on the diagram for plastic detectors pileup events is not a continuous trail, which is to be expected since they are faster than MUSIC detectors. Those can be cleared by applying a graphical cut to select the correlation. This cut can be seen in red in figure 3.4.

In total this selection removes of the order of 10% to 15% of events in the total particle

identification diagram. The main effect that can be observed in figure 3.5 is the trail at high Z that is removed. These events are not fully removed since it would require a more restrictive graphical cut which would also remove events of interest.

Charge collection correlation

The charges measured by plastic detectors are not used for reconstruction because of their poor resolution. However they can be used to check the consistency of the information between scintillators and ionisation chambers with the method described below. This method also allows the removal of out-of-target nuclear reacted ions.

Thanks to the two different types of variables measured in plastic scintillators, we express the position x in two different ways. First from equation 3.2 we obtain:

$$\begin{cases} \ln\left(\frac{Q_R}{Q_0}\right) = -\frac{L+x}{\lambda} \\ \ln\left(\frac{Q_L}{Q_0}\right) = -\frac{L-x}{\lambda} \end{cases} \tag{3.4}$$

Subtracting the two equations, we can express the position x of the ion as a function of the measured charge signals on each end of the scintillator:

$$x = \frac{\lambda}{2} \ln\left(\frac{Q_L}{Q_R}\right) \tag{3.5}$$

Similarly, knowing the propagation velocity v of the light in the scintillating medium, one can deduce the position x of the ion from the time difference between left and right signals:

$$x = \frac{v}{2} \left(T_L - T_R\right) \ . \tag{3.6}$$

Combining equations 3.5 and 3.6 shows a proportionality relation between $\ln\left(Q_L/Q_R\right)$ and $(T_L - T_R)$:

$$\frac{\lambda}{2} \ln\left(\frac{Q_L}{Q_R}\right) = \frac{v}{2} \left(T_L - T_R\right) \tag{3.7}$$

This allows the removal of inconsistent events, for example multihit (similarly to the PPAC case) or remaining pileup events. In figure 3.6, we show the correlation between $\ln\left(Q_L/Q_R\right)$ and $(T_L - T_R)$ for the F8 plastic scintillator. The diagonal ellipse shows that most of the events have a linear correlation as expected. For this specific case, a non negligible portion of events do not match this correlation possibly due to collection problems on a side of the plastic scintillator. We removed them using the ellipse drawn in the figure as a selection, and an additional 1.8% of events are removed through this step.

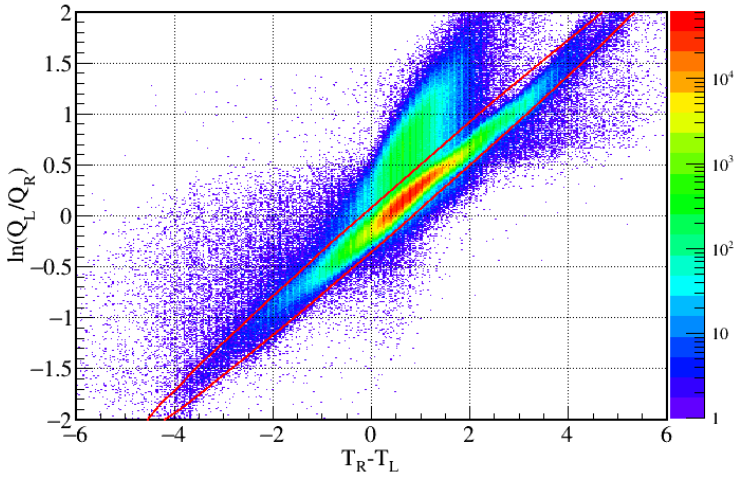

Figure 3.6 – Event removal in the F8 plastic scintillator to require correlation between charge and time. Red ellipse shows the events selected for physics analysis.

Ion charge state selection

The $B\rho$ value is proportional to A/Q. Therefore if the charge Q of the nucleus stays constant, $B\rho$ stays constant as well. Accelerated ions can however capture an electron along the way in the spectrometer changing their charge state and thus their $B\rho$. If on the contrary there is no change of charge state in the middle of the spectrometer, the ratio between the rigidity in the first part and in the last part of the spectrometer should be constant and characteristic of the energy lost in the spectrometer (the fewer the materials, the closer $B\rho_1/B\rho_2$ is to 1). Since our PID construction assumes the beam to be fully stripped, we need to remove events in which a change of charge state has been identified.

We show $B\rho_1$ against the ratio $B\rho_1/B\rho_2$ in figure 3.7. The middle spot (close to 1 on the X-axis) corresponds to unchanged beam charge state (fully stripped in our case). Separated spots on the side show that there are some events with a charge state of $+1$ and with a charge state of -1. Indeed if a fully stripped nucleus coming out of the production target catches an electron between the first part of the spectrometer and the second one, its charge is reduced, therefore its $B\rho$ is increased. In figure 3.7 it corresponds to the left spot. The right spot corresponds to a nucleus that is not fully stripped in the first part of the spectrometer, and loses an electron during its travel time thus increasing its charge and decreasing its $B\rho$.

This example is given for the ZeroDegree because even though there is a 2 mm aluminium degrader in BigRIPS (and therefore necessarily a rather large number of electron captures), the presence of a momentum slit that selects the charge states implies that we do not observe any in our data.

The selection applied in figure 3.7 is to keep events with $B\rho_{8,9}/B\rho_{9,11}$ superior to 0.985 and inferior to 1.025. The impact of this selection on the particle identification diagram

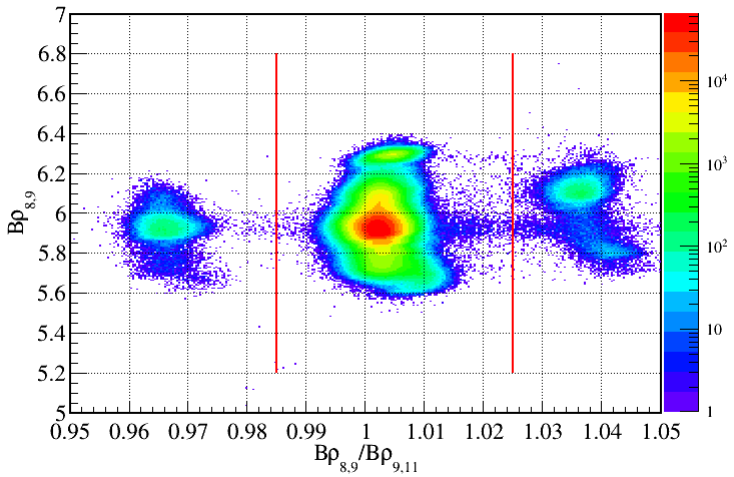

Figure 3.7 – Charge states in the ZeroDegree spectrometer. The X-axis shows the ratio between the rigidity in the first part of the spectrometer (from F8 to F9) and the rigidity in the last part of the spectrometer (from F9 to F11). The selected events lie between the red lines.

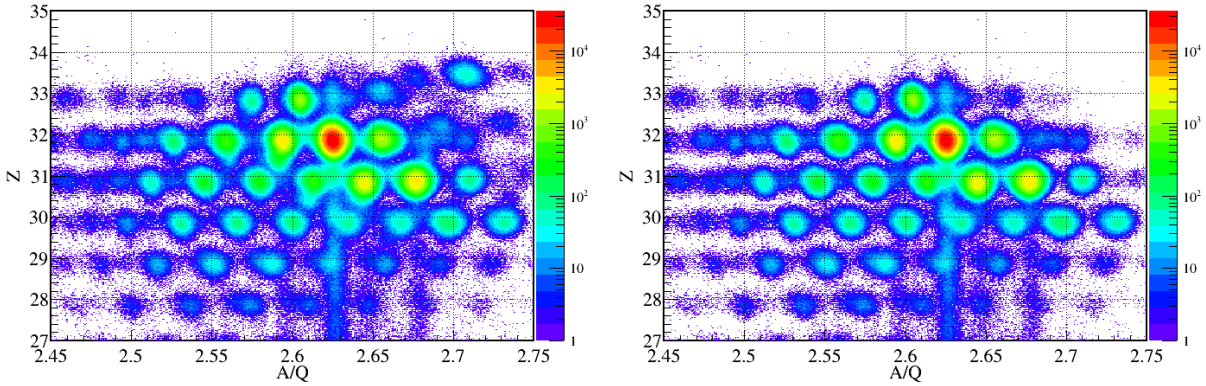

(a) Before charge-state selection. **(b)** After charge state selection.

Figure 3.8 – Charge-state selection in ZeroDegree spectrometer. On the left before the removal, and on the right after the removal.

can be seen in figure 3.8 (left: before, right: after). Some additional spots on the diagram that were corresponding to unwanted charge states can be observed in the top right corner in figure 3.8a at about $A/Q \approx 2.7$ and $Z \approx 33.5$, which could correspond to ^{84}Ge with a charge of +31 ($A/Q = 2.7$).

3.1.3 PID construction

Mass-to-charge ratio calibration The determined mass-to-charge ratio A/Q and charge Z are highly dependent on the measured velocities β. For relativistic beams, the travel time from one end of a spectrometer to the other is comparable to the travel time of the signal from plastic scintillators to the central acquisition system (few hundreds of nanoseconds).

Therefore if the signal travel time isn't compensated it has a large impact on A/Q and Z identification.

The time-of-flight offset to apply as a compensation is determined based on the knowledge of the most intense species (^{84}Ge) in our cocktail beam. We produced several identifications for different time-of-flight offsets (ToF_{offset}). For each offset, a different central A/Q value is measured. From equation 2.14, there is a linear correlation between the measured central A/Q and ToF_{offset}. This allows to find the ToF_{offset} value that gives the expected theoretical mass-to-charge ratio (2.625 in BigRIPS for ^{84}Ge, and 2.594 in ZeroDegree for ^{83}Ge).

The centred A/Q against time-of-flight offset values are shown in figure 3.9 with BigRIPS spectrometer on the left (using ^{84}Ge) and ZeroDegree spectrometer on the right (using ^{83}Ge). An optimum value for each spectrometer that arises from this method is shown by the blue dashed lines.

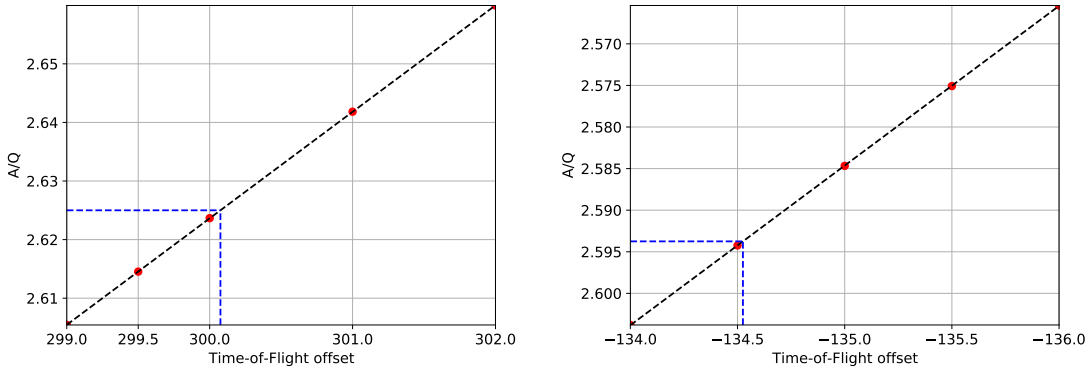

(a) BigRIPS **(b)** ZeroDegree

Figure 3.9 – Optimal time-of-flight offset determination. Blue dashed lines represent the expected mass-to-charge ratio and its corresponding time offset for ^{84}Ge in BigRIPS (left) and ^{83}Ge in ZeroDegree (right). Red dots are experimental points and the black lines are linear fits.

Applying the determined offsets inevitably shifts the extracted Z value as well. This led us to applying a small re-calibration of the charge afterwards in order to have the identification spots right where they are expected.

Calibration of the charge The ionisation chambers (MUSIC) measure the deposited energy using six electrodes (see section 2.2.4). The charge measured in each strip of the chamber is presented in figure 3.10. These ADC values are calibrated for each channel and then the geometrical mean of all the layers is calculated to be used in the formula 2.16 presented in section 2.2.4 thus giving Z. All gain matching for the strips and calibration has been done prior to the experiment.

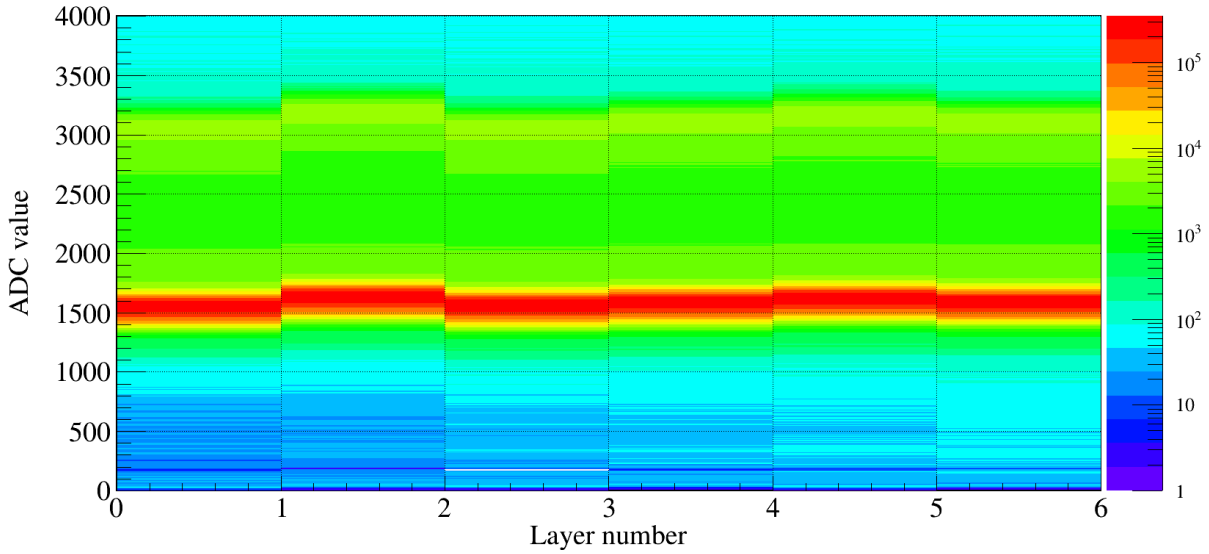

Figure 3.10 – Raw ΔE from the MUSIC detector in F7 in each of the six layers.

Stability The stability of all the used variables over the course of the beam time have been checked. The only rather unstable variable is the charge measured in ZeroDegree due to some jumps of the measured ΔE in the ionisation chamber (see figure 3.11).

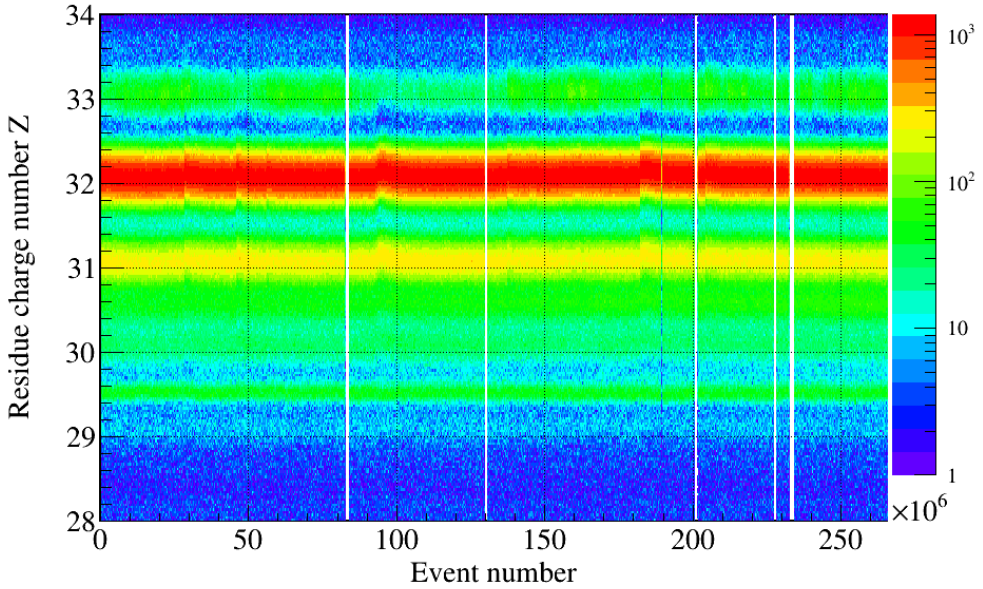

Figure 3.11 – Z value measured in ZeroDegree over the course of the experiment.

The jumps of the measured ΔE in the ionisation chamber in ZeroDegree were small enough to have no impact on our identification since the species are also separated by their mass-to-charge ratio.

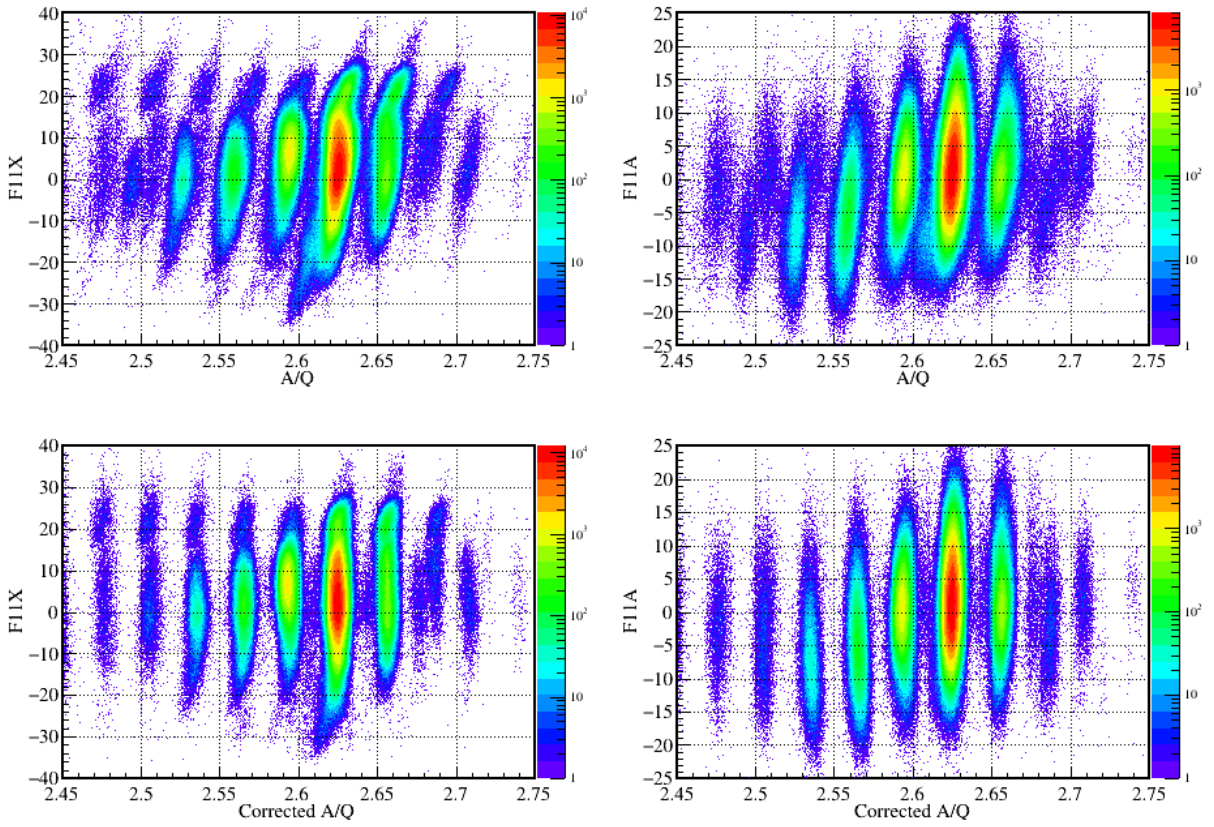

Figure 3.12 – Example of the optical correction of the dependencies between the A/Q measured in ZeroDegree and the position X and angle A measured in F11. On top before correction, A/Q and kinematic variables in F11 are not independent. On the bottom after correction, most of the dependency is corrected for. See text for details on the optical corrections.

Optical corrections

Some dependencies on spectrometer variables can be found in the A/Q distribution. This can be demonstrated with an example in the upper part of figure 3.12 where the A/Q value that should theoretically be independent of the position or angle in any focal plane shows a dependency (one would otherwise expect a straight vertical line). Therefore the resolution in A/Q is deteriorated. This is partly due to transfer matrices approximations.

The A/Q are determined using the transfer matrix of the spectrometers. The following equation (equivalent to equation 2.9 shown in section 2.2.3) is used to calculate $\delta = \Delta B\rho/B\rho$ which then leads to A/Q:

$$\begin{pmatrix} F5A \\ \delta \end{pmatrix} = \begin{pmatrix} (x|a) & (x|\delta) \\ (a|a) & (a|\delta) \end{pmatrix}^{-1} \times \left[\begin{pmatrix} X_{F7} \\ A_{F7} \end{pmatrix} - X_{F5} \times \begin{pmatrix} (x|x) \\ (a|x) \end{pmatrix} \right] \tag{3.8}$$

Here we correct, in each spectrometer, dependencies of A/Q on X, Y, A, and B (the positions and angles in each focal plane). The procedure consists in finding a function f_{BR}

and f_{ZD} such that:

$$\begin{cases} A/Q^c_{BR} = A/Q_{BR} - f_{BR}(X_{F5}, Y_{F5}, A_{F5}, B_{F5}, X_{F7}, Y_{F7}, A_{F7}, B_{F7}) \\ A/Q^c_{ZD} = A/Q_{ZD} - f_{ZD}(X_{F9}, Y_{F9}, A_{F9}, B_{F9}, X_{F11}, Y_{F11}, A_{F11}, B_{F11}) \end{cases}, \tag{3.9}$$

where A/Q^c_{BR} and A/Q^c_{ZD} are the new mass-to-charge ratio in BigRIPS and ZeroDegree, respectively, with same central value but without focal plane kinematics dependencies.

In order to do so, we use an algorithm from [56, MultiDimFit class] [1] that determines the functions f_{BR} and f_{ZD} as a multi-linear (with interaction terms included) polynomial of maximum degree set to 4 (empirically chosen to compromise between acceptable running time and high order dependencies).

Applying this correction to the dependencies described above gives the result presented in the lower part of figure 3.12. In the corrected graph the lines are now mostly straight and the dependencies of A/Q on X and A variables in F11 are removed in this example. The same effect can be observed for every variable considered.

This treatment improves the A/Q resolution and allows a better separation of the isotopes. The FWHM resolution achieved in BigRIPS is 0.18% for ^{84}Ge, and the one achieved in ZeroDegree is 0.25% for ^{83}Ge. in figures 3.13a and 3.13b, we show the distribution of the mass-to-charge ratio for germanium isotopes in BigRIPS and ZeroDegree. The resolutions quoted here are obtained through a gaussian fit of the shown distributions for the element of interest in BigRIPS and ZeroDegree.

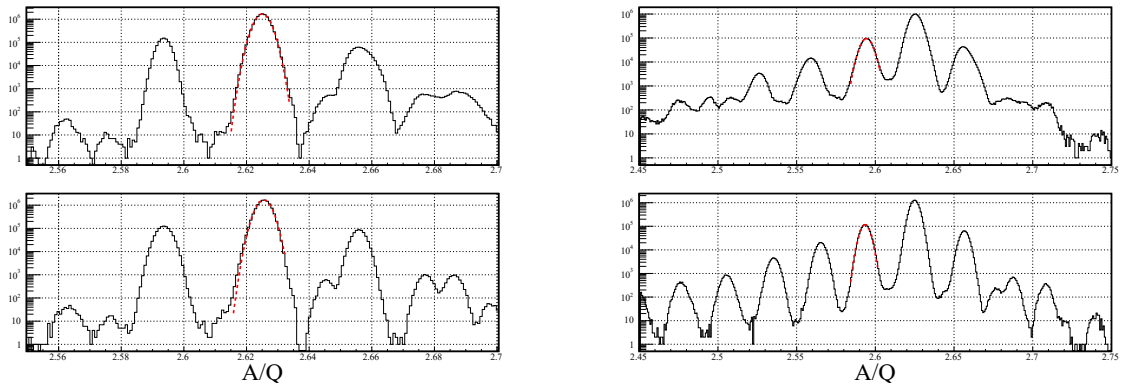

(a) BigRIPS **(b)** ZeroDegree

Figure 3.13 – Projection of the BigRIPS and ZeroDegree PID for germanium isotopes. Top: before optical corrections. Bottom: after optical corrections. The A/Q resolution is measured for ^{84}Ge in BigRIPS and for ^{83}Ge in ZeroDegree.

The extracted Z of the nuclei can also have some unwanted dependencies. In our case we corrected its dependencies with respect to β using the following correction formulae

1. https://root.cern.ch/doc/master/classTMultiDimFit.html

(up to second order, determined using an polynomial fit) respectively for BigRIPS β and ZeroDegree β:

$$\begin{cases} Z_c(BR) = Z + 2.1994\beta_{BR}^2 - 16.2184\beta_{BR} + 9.45 \\ Z_c(ZD) = Z + 18.3313\beta_{ZD}^2 - 17.3329\beta_{ZD} + 4.07 \end{cases} \tag{3.10}$$

The gain in charge resolution from this correction is negligible.

These two optical corrections above allow for an easier separation of the isotopes as can be seen in figure 3.14 where the identification diagrams are compared before and after optical corrections. Some elements that were overlapping for example ^{82}Ga ($A/Q = 2.645$) and ^{85}Ge ($A/Q = 2.656$) are now separated thanks to this procedure.

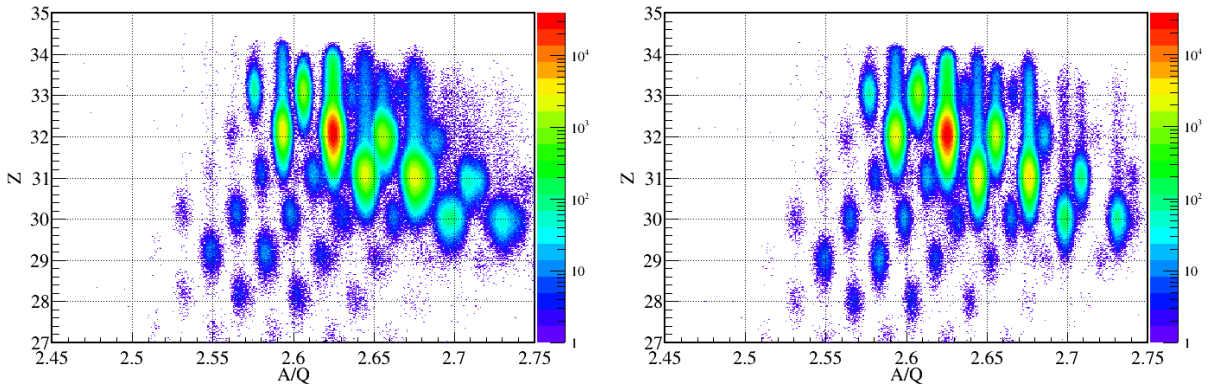

(a) BigRIPS

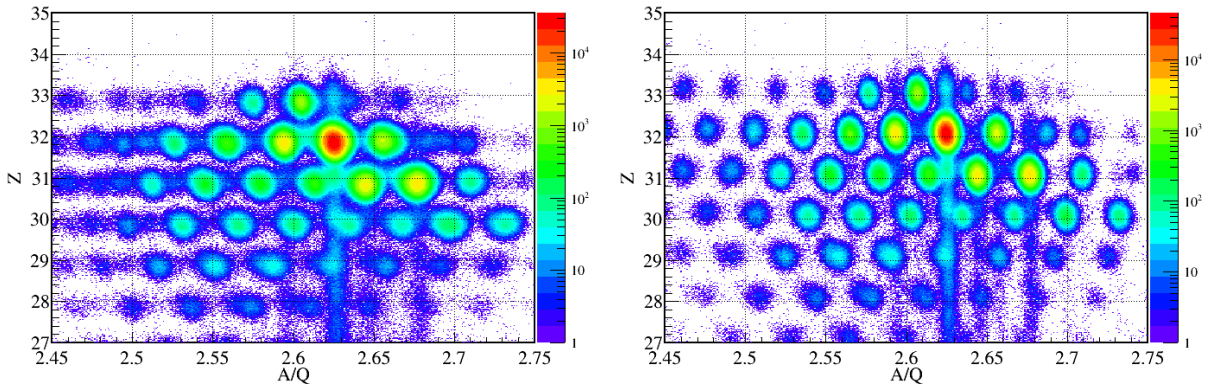

(b) ZeroDegree

Figure 3.14 – Effect of the optical corrections on the Particle Identification Diagrams in BigRIPS and ZeroDegree. On the left: before treatment. On the right: after.

With the elements now sufficiently separated on the particle identification diagrams, the reaction channels will be selected in order to treat the γ-ray spectra. The next section will present the calibration steps required on HiCARI data before obtaining a Doppler corrected γ-ray spectrum.

3.2 HiCARI calibration

This section will present details of the procedure used for energy calibration and time alignment, the achieved precision, as well as the γ-ray efficiency extraction.

3.2.1 Energy calibration

For the energy calibration of this multi-detector, sources of ^{60}Co (two transitions), ^{152}Eu (ten transitions), ^{133}Ba (five transitions) have been used.

The shape of a γ-ray peak in a germanium semi-conductor detector is affected by a low-energy tail mostly due to incompletely collected charges because of imperfections in the crystal structure [57].

The low energy tail is taken into account empirically by adding a step function to our linear background estimation under the peak. The total fitting function is written as follow:

$$f(E) = \underbrace{p_0 E + p_1}_{\text{linear}} + \underbrace{\frac{p_2}{\sqrt{2\pi}p_4} \exp\left\{\left(-\frac{(E-p_3)^2}{2p_4^2}\right)\right\}}_{gaussian} + \underbrace{\frac{p_5}{\left(1+\exp\left\{\left(\frac{E-p_3}{p_4}\right)\right\}\right)^2}}_{step} \tag{3.11}$$

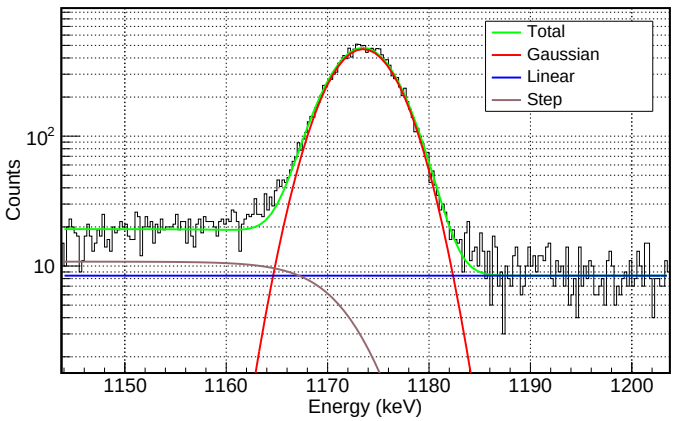

Figure 3.15 – Fit example of the 1173-keV peak in ^{60}Co spectrum. Green line shows the final fit while red and brown lines show the contribution of the gaussian term and the step term respectively.

A visible doublet peak in the ^{152}Eu spectrum at 1085.8 keV is fitted using a sum of two gaussians and a simple linear background. This doublet was not visible on the eye-test for nine of the crystals therefore for those crystals the fit is the function defined on equation 3.11. For seven of the crystals, the first europium peak at 121.7 keV was not strong enough and therefore has not been fitted either. Each segment has also been calibrated

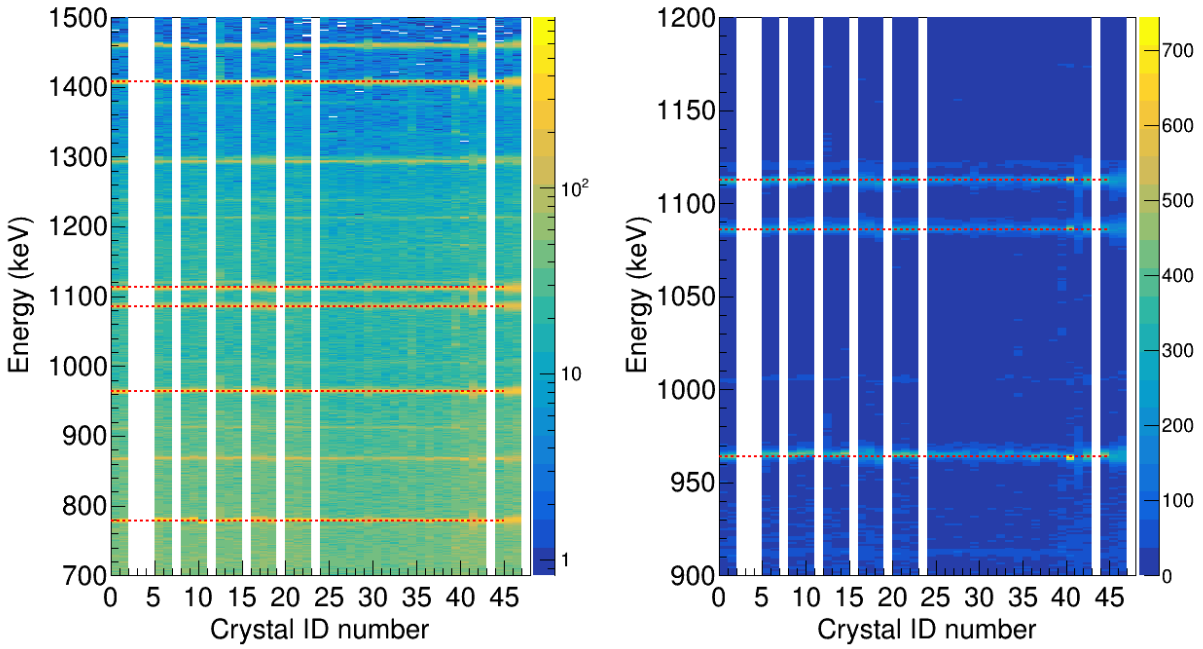

Figure 3.16 – Calibrated γ-ray energies from a ^{152}Eu run for every crystal. Selected literature energies of ^{152}Eu transitions are shown with the dotted red lines. On the left a wide range of energies show a seemingly good calibration. On the right a closer look shows some residuals mainly due to ADC non linearities.

using a simple background and without any doublet consideration. An example of a fit of a ^{60}Co peak is shown in figure 3.15.

The ADC values extracted from those fits (parameter p_3 in equation 3.11) are then correlated linearly with the associated peak's energy to obtain calibration coefficients for each crystal and segment.

Figure 3.16 shows the superimposition of literature energies (black lines) with a calibrated spectrum from a ^{152}Eu source. Some deviations from the literature lines can be observed. The quality of the calibration can be evaluated using the residuals $E_{th} - Ecal$ where E_{th} is the theoretical energy and E_{cal} is the calibrated energy. An example of those residuals plotted against the energy is shown in figure 3.17a.

One can observe a zig-zag pattern roughly centred around zero with an amplitude of about ± 2 keV. This is caused by non-linearities of the Analog-to-Digital converter. As illustrated in figure 3.17b, such non-linearities pattern have already been observed for GRETINA digitisers. Some experiments have corrected this pattern using a measured response from an input slow voltage ramp that scans the entire ADC range. In other experiments [58] the corrections reduced the residual spread to about 0.1 keV.

The online decomposition algorithm (see figure 2.14) requires a calibration in order to compare the measured signal shapes to the pulse-shapes tables. Therefore applying new

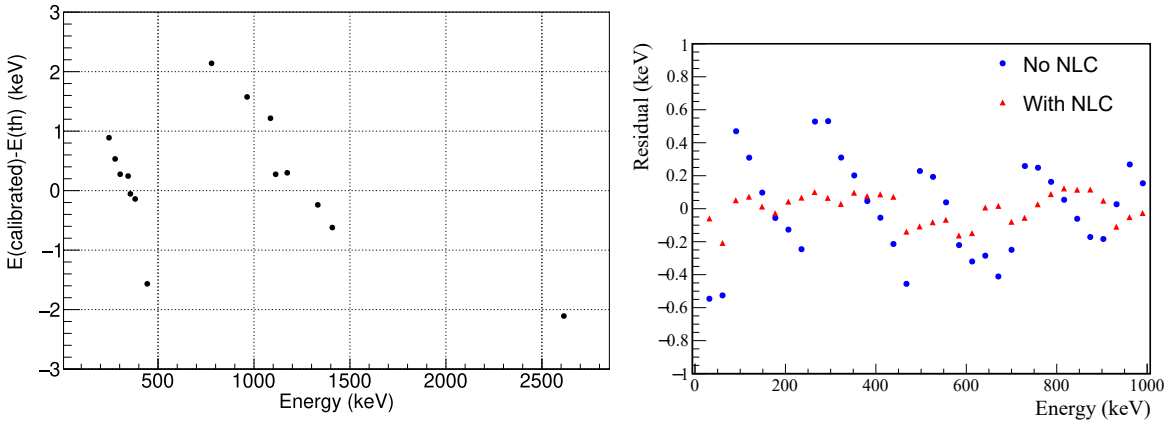

(a) Our experiment.

(b) Extracted from [58].

Figure 3.17 – (a) Energy residuals (in keV) between calibrated and tabulated values for a MINIBALL crystal given as an example. (b) Non linearities of the ADC (blue) observed in [58] for a GRETINA detector. The red dots show the results after their correction procedure (NLC stands for NonLinearity Correction.

calibrations to the mode-2 data would require to rerun the decomposition algorithm. For schedule reasons, for mode-2 data online calibration coefficients were used. The residuals have been verified to be of the same order as the ones resulting from an offline calibration.

3.2.2 Efficiency

The efficiency of the HiCARI array is determined using a known activity of each source at a certain date, and the date and duration of each calibration run. We can calculate the number of γ rays emitted during the run as $N_{emitted} = A \times \tau$ where A is the activity (in Bq) and is assumed constant and τ is the duration. These are given in table 3.2 [59].

Source	Activity (Bq)	Duration (s)	N
^{60}Co	21691.8	891	19327394
^{152}Eu	6155.3	1845	11356528
^{133}Ba	48784.7	1199	58492855

Table 3.2 – Activities of each source used, duration of each corresponding calibration run, and calculated number of emitted γ rays.

Unused crystals

The total efficiency of HiCARI is affected by the removal of malfunctioning crystals from the analysis. In total nine crystals are not taken into account in the analysis for several reasons (three were not functioning, three had double peaks, two had a very high threshold and degraded data, one had a degraded energy resolution). Those removed

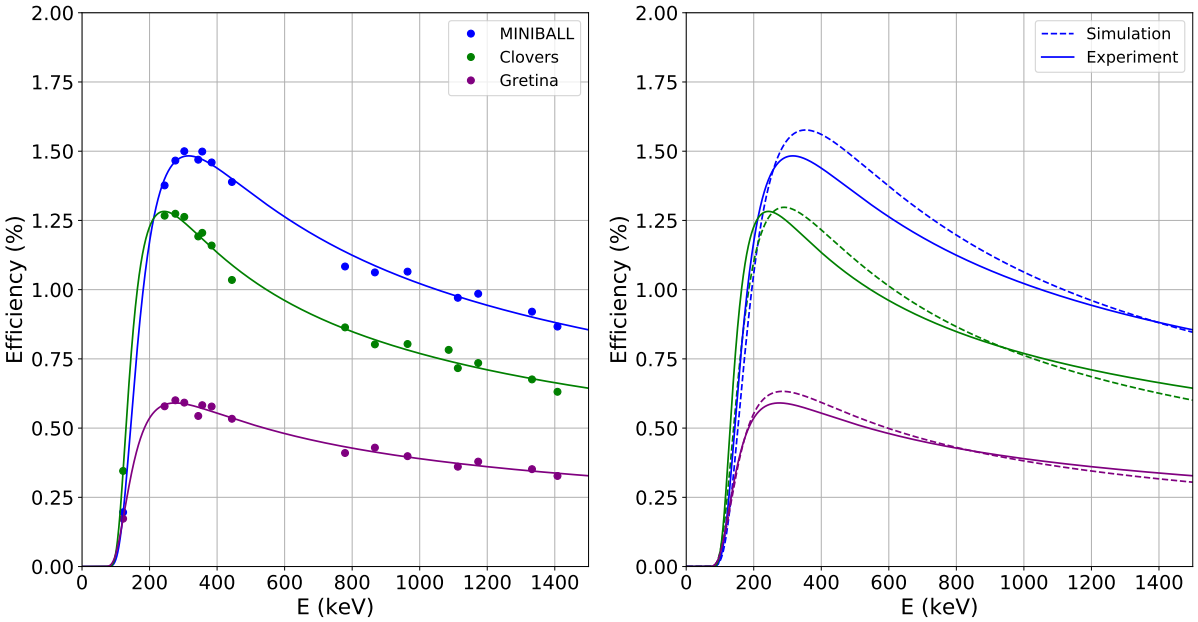

Figure 3.18 – On the left: separated efficiency of all the type of detectors with experimental data points and the fitted *ad hoc* function. On the right: comparison between simulated efficiency (dashed lines) and experimental fitted function (plain lines).

crystals comprise five from MINIBALL, two from Clovers, and two from the GRETINA Quad detector. In addition, the signals from the P3 detector were not fully decomposed during our beam time (first experiment of the campaign) therefore we did not use it for our analysis and left it to be added in the future.

The efficiency is calculated from $N_{emitted}$ using the integral parameter p_2 from the peak's fit as defined in equation 3.11, and the branching ratio p:

$$\epsilon = \frac{p_2}{N_{emitted} \times p} \tag{3.12}$$

The efficiency curve has been fitted using the following four-parameters function:

$$\epsilon(E) = aE^b exp\left(-\left(\frac{E}{c}\right)^d\right) , \tag{3.13}$$

where a is a scaling factor, b is related to the slope at higher energies, c is the energy at the maximum efficiency, and d is the attenuation coefficient at lower energies [60].

The total efficiency calculated during commissioning using the same 0.5 mm Pb shielding was of about 4% at the maximum and 2.5% at 1 MeV. In our experiment we observe an efficiency of about 4.5% at the maximum and 3% at 1 MeV. Separated efficiencies for each type of detectors have been calculated and are shown in figure 3.18 along with the

Geant4 simulated efficiencies (more details in section 3.4) on the right side of the figure. We obtain a good overall agreement comparable with previous simulation studies [61]. The agreement with experimental data is necessary for the determination of cross sections in further chapters.

3.2.3 Time alignment

Time correlation between beam and γ-ray events is verified in this section.

The timestamp associated with the BigRIPS event (ts_{BR}) is measured at the passing of the ion in the plastic scintillator in the focal plane F7. This time is compared to the recorded γ-ray event timestamp (ts_{gamma}):

$$\Delta t_{event} = ts_{gamma} - ts_{BR} \tag{3.14}$$

Gamma rays detected in HiCARI emitted from the beam should have the same timestamp difference $ts_{gamma} - ts_{BR}$. Time distributions of MINIBALL and Clover type detectors were not aligned and hence were realigned around zero (for convenience) by selecting events with a high enough energy ($E > 2$ MeV) so that it can only come from a desexcitation of the beam. An example of such a distribution is shown in figure 3.19.

Time alignment has been done using a fit of the peak's position in the time distribution for events with $E > 2$ MeV. The clock defining the timestamps ticks at 100 MHz, which means that a timestamp unit corresponds to ten nanoseconds.

In order to align them, the distributions are fitted with a skewed gaussian:

$$f(t) = \frac{A\lambda}{2} \exp\left\{ \left(\frac{\lambda}{2} \left(2m + \lambda\sigma^2 - 2t \right) \right) \right\} \times \operatorname{erfc}\left(\frac{m + \lambda\sigma^2 - t}{2\sigma} \right) \tag{3.15}$$

Overall this gives a total resolution in time of about $\sigma = 12$ ns for the MINIBALL, and $\sigma = 6$ ns for GRETINA-type detectors. Those resolutions are calculated using the type of figure presented for an example of MINIBALL and an example of GRETINA-like crystal in figure 3.19. One can observe that the GRETINA-like crystals have a much better time resolution and a much weaker walk effect at low energy [57]. This is due to the fact that in addition to the leading-edge trigger used for every crystal on the setup, the decomposition algorithm runs a CFD filter on top that is necessary for a good treatment of the traces [55].

A contour can be applied in order to select events in correlation with the beam. For example in the top right part of figure 3.19, some horizontal lines (at about 700 keV for example) are completely uncorrelated in time with the beam. The applied contour in red helps to remove these background γ-ray events.

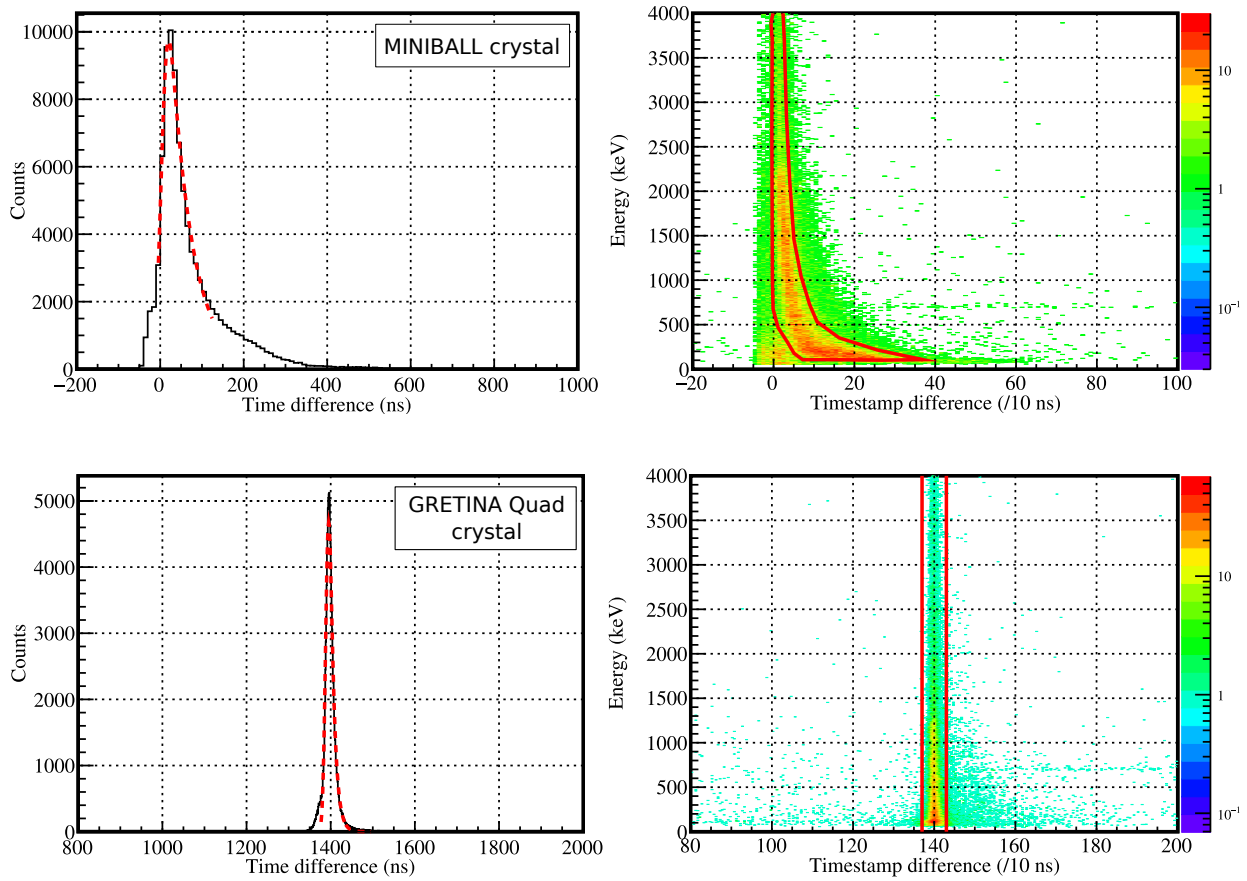

Figure 3.19 – Example of a time distribution for a MINIBALL crystal on top and a GRETINA Quad crystal on the bottom. On the right side the time difference is shown against the energy with the graphical selection applied to the data as red lines. The difference of resolution and behaviour at low energy are discussed in the text.

3.3 Production of the Doppler corrected spectra

As described in section 2.3.1 the γ rays being emitted in flight, a correction of the Doppler effect needs to be performed. This section will go into details on how the parameters for this procedure are adjusted.

3.3.1 Trajectory reconstruction around F8

In order to find the angle between the emitted γ ray and the emitting residual, some trajectography has to be performed around the target. The angle of interest is determined by measuring the angle of the residual with respect to the incoming beam direction (scattering angle θ_S) on one hand, and the angle of the γ ray with respect to the beam axis (θ_γ) on the other hand.

Alignment of the additional PPAC in F8

The angle of the residual with respect to the beam axis θ_S is measured using the additional PPAC pair in F8 after the target (F8PPAC-3A and F8PPAC-3B). Since those PPAC are non-standard, they need to be aligned with the beam line by offsetting the position data.

The alignment method was performed using runs without a target. We extrapolated values of X and Y at the position of the third PPAC in F8 assuming a straight line trajectory. An example for the X direction is given by the equation below:

$$X_{extrapolated} = X_{before} + \Delta Z \times \tan\theta_X \tag{3.16}$$

By comparing those values with actual X and Y measured by the third PPAC pair in F8, we observe the shifts listed in table 3.3 and these values were used as offsets for the analysis.

PPAC name	X Offset (mm)	Y Offset (mm)
F8PPAC-3A	-0.08682	-1.161
F8PPAC-3B	1.646	-0.2919

Table 3.3 – Offsets applied in the analysis to compensate for F8PPAC-3 misalignment.

Scattering angle determination

The two PPAC detectors before the target in F8 are used to measure the incoming beam direction vector ($\overrightarrow{V_{in}}$). In the absence of a vertex tracker for the reaction in the target, the

position of the reaction is always assumed to be in the transverse plane passing through the centre of the target. Using the incoming beam direction, we extrapolate an assumed vertex position in the target (X_t, Y_t, Z_t) where Z_t is always the half-depth of the target. The result of this vertex position reconstruction is shown in figure 3.20b.

Combining the (corrected) position measured by the PPAC pair after the target and (X_t, Y_t, Z_t) the position of the vertex in the target, we extract the outgoing beam direction vector ($\overrightarrow{V_{out}}$).

Event-by-event, the angle between $\overrightarrow{V_{in}}$ and $\overrightarrow{V_{out}}$ is calculated thus giving the scattering angle θ_S.

Resolution on the scattering angle and position on target

The scattering angle distribution can be calculated from the measurement described above. The distribution measured without a target gives a scattering angle spread that is characteristic of the measurement uncertainty.

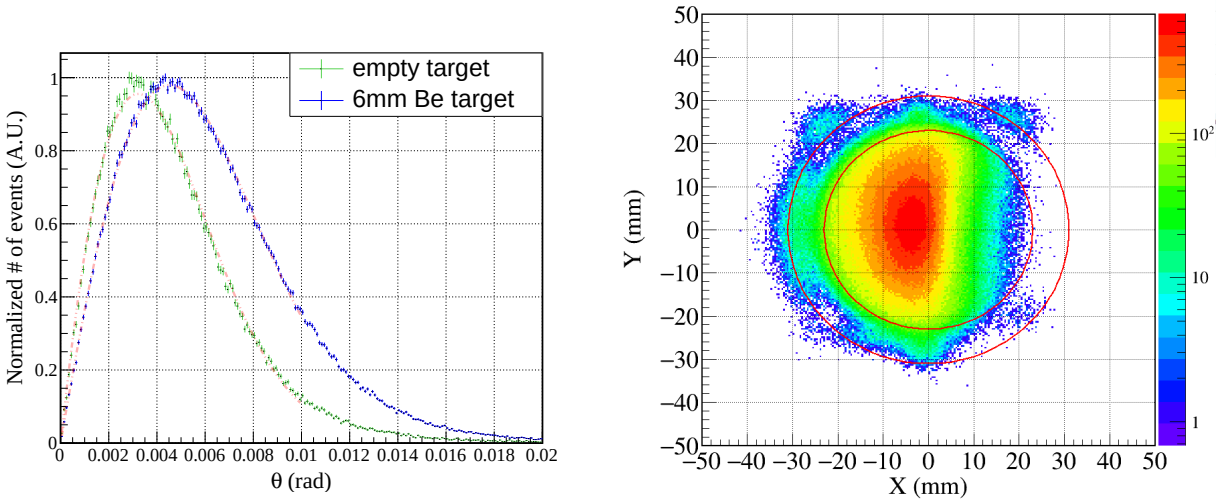

(a) Scattering angles

(b) Position on the target

Figure 3.20 – (a) Comparison of the scattering angle measured without the target, and with the target. Fitted functions are superimposed in red. (b) Reconstructed position of the vertex on the target (for the channel ^{84}Ge→^{83}Ge given as an example). The red circles represent the edges of the target holder.

in figure 3.20a the distributions have been fitted with the following function:

$$f(\theta_S) = \frac{A}{\sqrt{2\pi}\sigma} exp\left(-\frac{(\theta_S - \langle\theta_S\rangle)^2}{2\sigma^2}\right) \times \sin\theta_S \times \cos\theta_S\,, \tag{3.17}$$

where A, $\langle\theta_S\rangle$, σ are the usual gaussian parameters. The sine and cosine factors come from geometrical considerations although at angles as low as few milliradians, the approximations

$\cos\theta_S \approx 1$ and $\sin\theta_S \approx \theta_S$ could have been used without a visible loss of fit quality. This will allow us to compare the scattering angle with the simulation in section 3.4.5.

3.3.2 γ-ray interaction vertex

In order to determine the angle at which the γ ray was emitted, the coordinates of the interaction point in the germanium detector need to be found. The procedure differs between GRETINA-type detectors and the others.

For MINIBALL and Clover types detectors, the segment that stored the highest energy (in the lab frame) is defined as the first hit segment. The coordinates of its centre are then used to define the position of the γ-ray interaction vertex.

A particular procedure is applied when one segment *only* did not work in a crystal. In this case, $E_{missing} = E_{core} - \sum_{segments} E_{segments}$ is the missing energy that the segment would have measured if it had worked. This missing energy is therefore assigned to it and the comparison with other segments can proceed.

For GRETINA-type detectors the signal decomposition described in section 2.3.3 is applied in order to give the γ-ray interaction vertex coordinates.

As mentioned in section 2.3.3 the positioning of HiCARI with respect to the lab frame is done *via* the photogrammetry process. An unknown offset between the reference frame in which γ-ray interaction points are placed and reaction vertex coordinates has an impact on the result of the Doppler correction (since the emission angle would be badly evaluated) that depends on the angle of the detector.

An offset between γ-ray detectors and beam frames would shift the position of the Doppler reconstructed peaks. This impact has been studied on data peaks by artificially shifting the reference frame of the beam away from its nominal position along the Z-axis and looking at the position of the Doppler corrected peak in the data. In figure 3.21, the energy position of a peak in the MINIBALL detectors is plotted against a shift between the two frames (for a velocity $\beta = 0.6$). This shows a dependency of the central position of the reconstructed peak of about 2.5 keV/mm at low angles (MINIBALL). For the GRETINA-type detectors (high angles), the same effect leads to 5 keV/mm.

3.3.3 β determination

The event-by-event velocity at the vertex of the reaction is crucial for a good Doppler correction. Although it is not directly measured we are able to determine it from velocity measurements elsewhere in the spectrometers along with energy loss calculations. This section will describe the method to deduce it from ZeroDegree measurements.

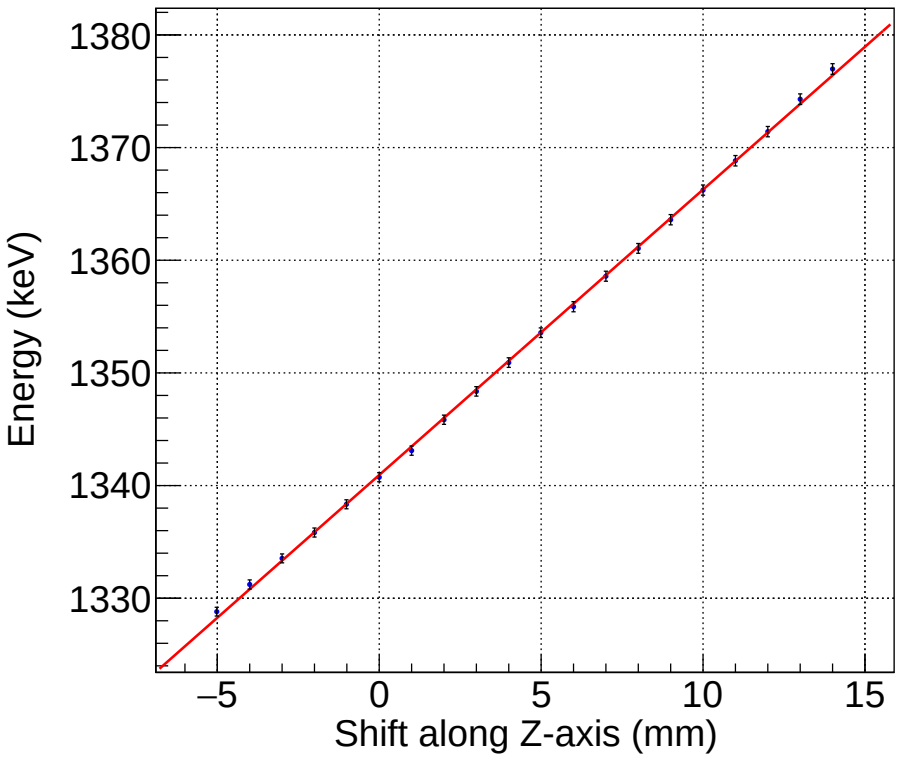

Figure 3.21 – Average energy shift dependency on an offset along the Z-axis between beam coordinates and γ-ray coordinates for MINIBALL detectors.

Verification of the procedure

For the determination of the beam's velocity at the middle of the target, energy loss calculations of the velocity measured in ZeroDegree (or in BigRIPS) can be performed in order to compensate for all the material along the beam's path. We used LISE++ physical calculator for energy loss evaluation.

A first step is to check the consistency of LISE++ energy loss calculations with the decreasing of beam energy (or β) in the spectrometers.

The velocity measured in a portion of a spectrometer corresponds to the mean velocity between the two plastic scintillators. In figure 3.22, the blue lines show the velocities between the detectors in the second part of BigRIPS (left) and ZeroDegree (right) assuming a reasonable starting velocity in F3. The green dotted line shows the average velocity in the portion of the spectrometer displayed. This shows that the velocities measured in the second part of BigRIPS and ZeroDegree can be reproduced by calculations of the beam's energy between F5PPAC-2 and F7PPAC-1, and between F9PPAC-2 and F11PPAC-1.

Using this knowledge we calculate the velocity between F9PPAC-2 and F11PPAC-1 by propagating energy loss in LISE++ to the velocity measured in BigRIPS. We can then compare it to ZeroDegree measurements using runs without reaction target.

In table 3.4 the comparison is presented between measured β in ZeroDegree and the one

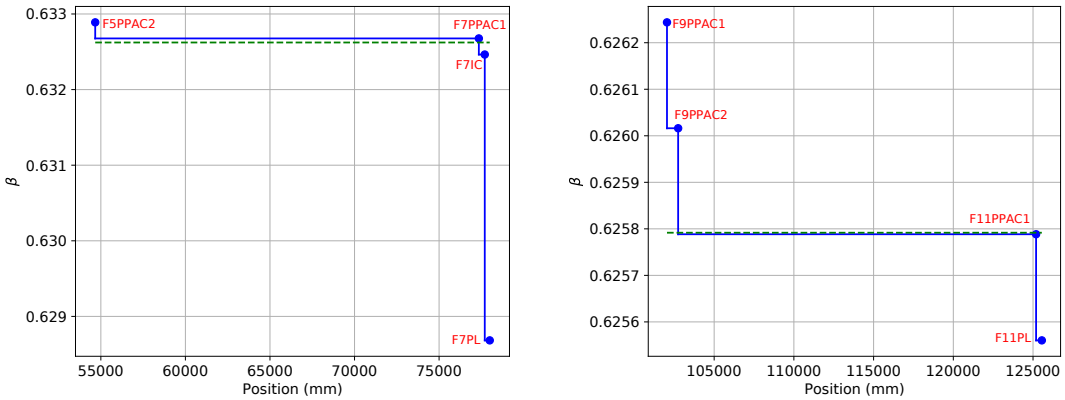

(a) Second part of BigRIPS **(b)** Second part of ZeroDegree

Figure 3.22 – Velocity determined *via* LISE++ energy loss calculations in parts of the spectrometers. On the left the results for the second part of BigRIPS, on the right results for the second part of ZeroDegree (used in two-fold β calculations). The green dotted line shows the average velocity in the corresponding portion of the spectrometer.

Beam nucleus	β_{ZD}^{Meas}	β_{ZD}^{Calc}	$\Delta\beta/\beta$
^{84}Ge	0.6257	0.6261	0.065%
^{83}Ga	0.6207	0.6213	0.101%
^{82}Ga	0.6269	0.6274	0.087%
^{83}Ge	0.6300	0.6308	0.114%

Table 3.4 – Comparison between velocity measured in ZeroDegree without a target (first column, noted β_{ZD}^{Meas}) and the velocity determined through energy loss calculations with LISE++ (second column, noted β_{ZD}^{Calc}). Last column shows the relative comparison: $(\beta_{ZD}^{Calc} - \beta_{ZD}^{Meas})/\beta_{ZD}^{Calc}$

determined though energy loss calculations applied to the velocity measured in BigRIPS. The difference obtained is of about 0.1% which gives an estimation of the systematic error on the velocity.

A second step of verification is to apply the same procedure taking into account the target. If there is a change of species, it is performed in the calculation at the middle of the target. The comparison between the velocity directly measured in ZeroDegree and the one deduced from BigRIPS measurement with energy loss calculations are shown in table 3.5 for three channels as an example. The difference obtained is of the same order as before.

Event-by-event β for the Doppler correction

As mentioned before, we perform the correction of the Doppler effect assuming the vertex position at the centre of the target. Therefore the velocity used has to correspond to the mean velocity of the beam at the middle of our 6 mm beryllium thick target.

The procedure described above also gives access to this mid-target velocity. It can

Channel	β_{ZD}^{Meas}	β_{ZD}^{Calc}	$\Delta\beta/\beta$
^{84}Ge$\rightarrow^{84}$Ge	0.5871	0.5871	¡0.001%
^{84}Ge$\rightarrow^{83}$Ge	0.5864	0.5868	0.077%
^{84}Ge$\rightarrow^{82}$Ge	0.5864	0.5870	0.010%

Table 3.5 – Comparison between velocity measured in ZeroDegree and the velocity determined through energy loss calculations with LISE++ from BigRIPS measurements.

be obtained by applying energy loss calculations either to the beam's energy measured in ZeroDegree or to the one measured in BigRIPS. Under the assumption of a conserved velocity at the reaction point, both methods should give similar results. The results for the main benchmark channel and the channel of interest are shown in table 3.6. The third column shows a marginal difference between the two approaches as expected. For our analysis we used the one determined from ZeroDegree measurements.

Channel	β_{ZD}^{Mid}	β_{BR}^{Mid}	$\Delta\beta/\beta$
^{84}Ge$\rightarrow^{83}$Ge	0.6086	0.6090	0.063%
^{84}Ge$\rightarrow^{82}$Ge	0.6089	0.6094	0.082%

Table 3.6 – Comparison between velocity determined at the middle of the target using ZeroDegree measurements (β_{ZD}^{Mid}) and using BigRIPS measurements (β_{BR}^{Mid}).

The β value is deduced at the centre of the target event-by-event using the following equation:

$$\beta_{doppler} = \beta_{ZD}^{Mid} \times \left(1 + \frac{\beta_{ZD}^{Meas} - \langle\beta_{ZD}^{Meas}\rangle}{\langle\beta_{ZD}^{Meas}\rangle}\right), \tag{3.18}$$

where β_{ZD}^{Meas} is the value measured event-by-event in ZeroDegree, $\langle\beta_{ZD}^{Meas}\rangle$ is the mean value of the overall distribution measured in ZeroDegree, β_{ZD}^{Mid} is the velocity at the centre of the target according to energy loss calculations described above. This gives event-by-event a β for the Doppler correction with a realistic deviation from the mean velocity.

3.3.4 Examples of resulting Doppler corrected spectra

Using the reconstructed scattering angle and the measured point of interaction of the γ ray in the detector, we have the angle θ_e at which the γ ray is emitted. The velocity is determined for each reaction channel individually and then used for the Doppler correction.

A comparison between the lab frame energy and the Doppler corrected energy as a function of the angle is shown for ^{82}Ge in figure 3.23. In the lab frame, one can clearly see the angular dependency of the two $2^+ \rightarrow 0^+$ and $4^+ \rightarrow 2^+$ transitions corrected when going to the centre-of-mass frame (right side panel).

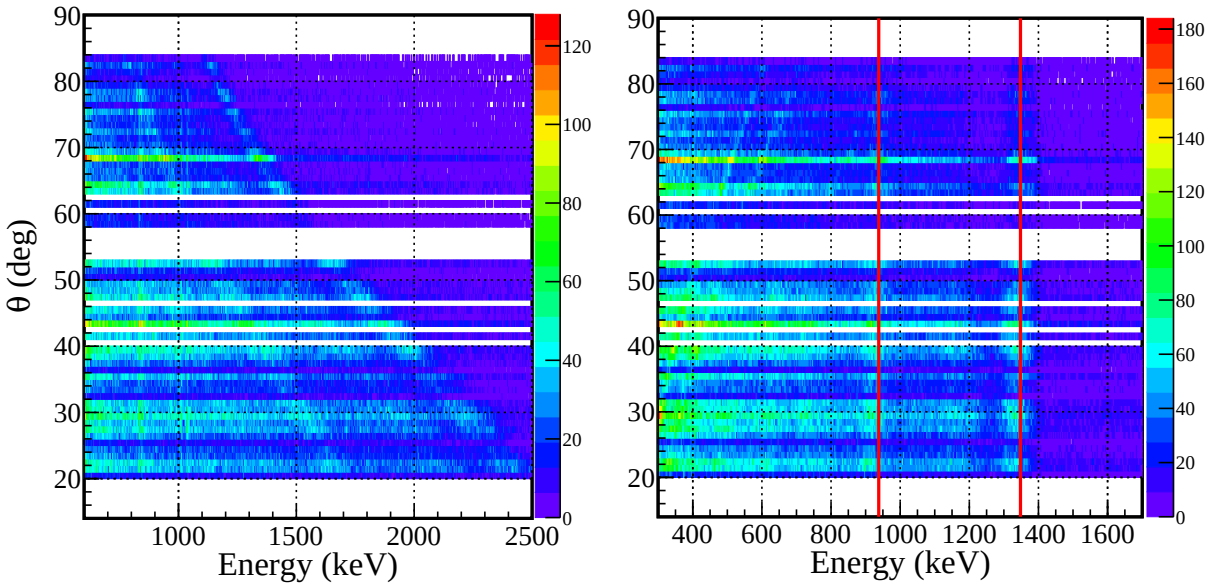

Figure 3.23 – Detector angle against energy compared in the lab frame (left) and in the centre-of-mass frame (right) for ^{82}Ge. Red lines indicate the expected 2^+ and 4^+ energies (respectively 1248 keV and 938 keV).

3.4 Simulation

The γ-ray analysis process discussed further requires GEANT4 simulations of the reaction target setup as accurate as possible. This section will describe the assumptions made for the simulation process and the tuning of the crucial parameters to match the data.

3.4.1 Resolution

For each individual detector in the simulation, the intrinsic resolution of the crystal is set manually. The energy dependence of the resolution is assumed to be of the form:

$$\sigma\left(E\right) = a \times \sqrt{1 + b \times E} \tag{3.19}$$

The a and b parameters are given to the simulation as inputs for each detector.

These parameters are extracted from data by fitting the resolution curve in the experimental data. An example of such a fit is given in figure 3.24.

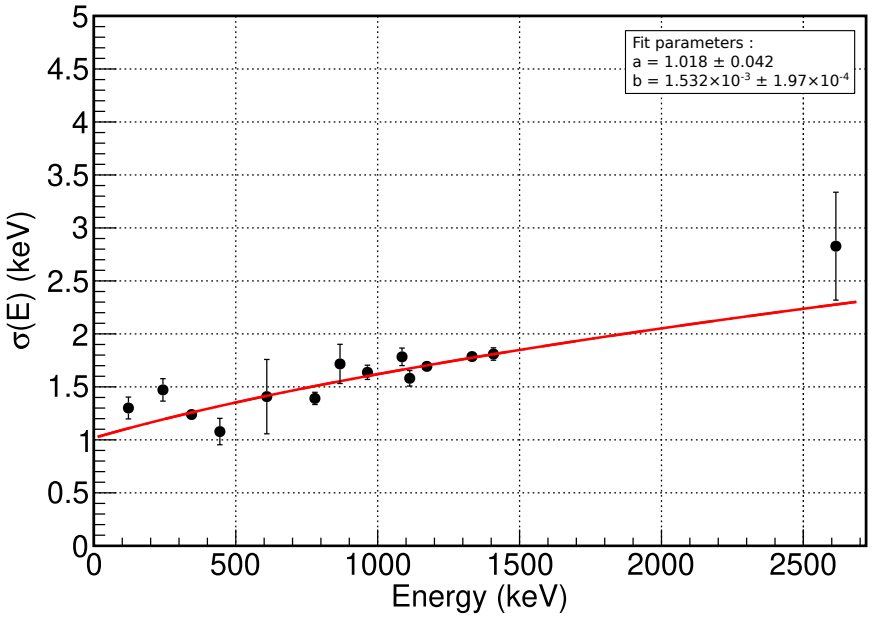

Figure 3.24 – Example of the extraction of the resolution parameters by fitting of a resolution curve for a crystal.

3.4.2 Threshold

The energy threshold also has to match with data. For this purpose we measured the threshold for each detector by fitting it with the following three-parameters function:

$$f(E) = p_0 \times \tanh\left(\frac{E - p_1}{p_2}\right) + p_3 \tag{3.20}$$

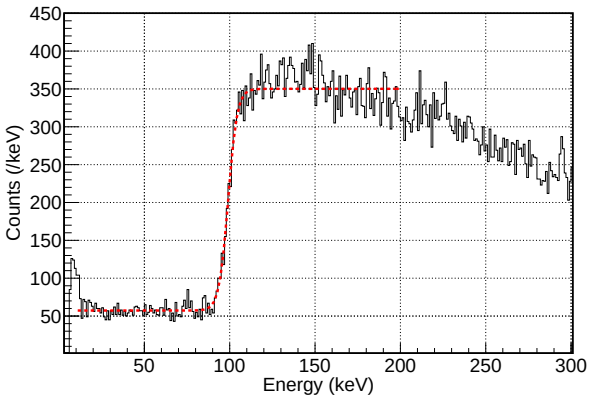

Figure 3.25 – Example of the threshold adjustment for a crystal in MINIBALL by fitting of the low energy part of the spectrum (in lab frame).

An example of the extraction of those parameters is shown in figure 3.25. Except for two MINIBALL crystals that have been dismissed in the analysis, all thresholds are around 100 keV.

3.4.3 Event generator

In order to match with our beam dynamics assumptions, the reaction mechanism is chosen to be a knockout reaction that conserves the velocity from the reacting beam to the reaction products: $\overrightarrow{v_i} = \overrightarrow{v_f}$. As discussed before, in the analysis, the assumption is made that the mean interaction point is the centre of the target, therefore a uniform distribution of interaction points within the target along the Z-axis is imposed in the simulation.

3.4.4 Geometry

The geometry of the detectors in the simulation is defined using the Computer Aided Design (CAD) drawings provided by the constructors of each type of detector (MINIBALL, Clover, GRETINA Quad, and P3). Knowing the relative positions of the detector capsules and their crystals, the CAD drawings are then transformed into GEANT4 geometries and placed in coordinates that match with the photogrammetry measurements mentioned in section 2.3.3.

The relative placements of the F8 focus, the target, and HiCARI are also reproduced in the simulation.

3.4.5 Consistency of the simulation with the data analysis

Once the events are generated by the simulation, they are analysed as in the data analysis. The kinematic variables need to be tuned for consistency with the data.

Beam trajectory

The scattering angle being a critical parameter for the Doppler correction, we need a match between simulated and observed distributions. Our GEANT4 simulation has two parameters that affect the scattering angle distribution: the angular spread along X and Y (A and B angle dispersions), and the momentum spread ΔP.

The experimental distribution width of an observable is a result of the "real" spread and the measurement uncertainty. The latter is calculated for our setup for different observables, and is simulated *via* a randomisation around a gaussian. The "real" spread is simulated by distributions in entry variables with arbitrary shapes and width that match the best our experimental distributions.

For the measurement uncertainty calculation, the position resolution of the PPAC detectors is taken to be 0.5 mm [43] (used for uncertainties of position and angles). The uncertainty propagation gives a 2.4 mm resolution for the position of the beam on the target, a 3.057 mrad resolution for the angle measurement.

A comparison between simulation and measurements for positions and angles is shown in figure 3.26b. The shape of the measured position and angle distributions is quite challenging to reproduce by analytical distributions. We obtain a good agreement nevertheless. In addition, the parameter that needs a close match with experimental data is the scattering angle. A comparison is shown in figure 3.26a showing good agreement. Such comparisons are checked for each studied reaction channel since the input spread to simulate might change.

Velocity

The other crucial parameter for the Doppler correction is the mean velocity at the reaction point. The simulation parameters are tuned so that the mean velocity at the exit of the target matches between the simulation and the energy loss calculations from ZeroDegree measurements. The shift of the distribution to centre it on the velocity at the middle of the target is then applied to the simulated β (the same procedure that is performed with the measured β described in the previous section). In figure 3.27, the comparison between simulated velocities and measured ones is shown. One can observe a slight difference between the mean velocity values used for Doppler correction in data analysis and simulation analysis. This is due to differences between energy loss tables in GEANT4 and in LISE++.

γ-ray interaction vertex

The GEANT4 simulation offers the possibility to register the average coordinates of the γ-ray interaction vertex for each segment. This procedure is realised for a simulation with a null lifetime. The obtained mean coordinates for the interaction vertices are then used for the Doppler correction in all the other simulations. A comparison between the centre of each segment and the average interaction points from the simulation is shown in figure 3.28. The main difference for ~ 1 MeV γ-rays is along the radial direction (~ 10 mm) which is mainly due to the fact that the average interaction point is closer to the front-end according to GEANT4.

A way to improve the Doppler corrected energy resolution would be to use the simulated average points of interaction for the Doppler correction in the data analysis. For schedule reasons it has not been done here. The improvement should not be very significant since the difference with the direct photogrammetry input is mainly radial (which doesn't change Doppler correction).

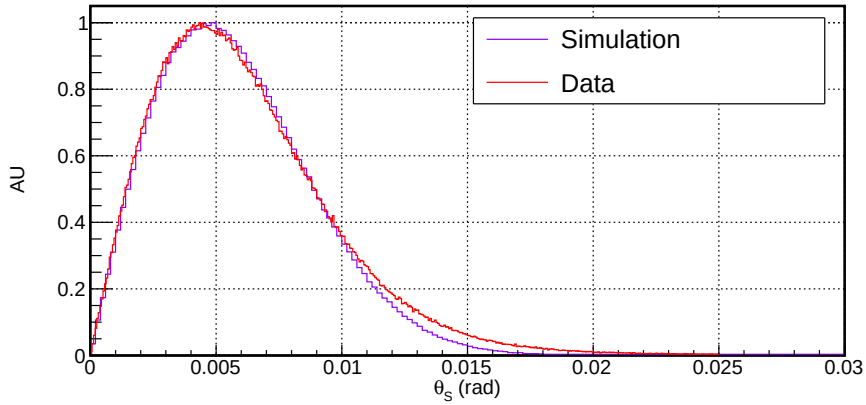

(a) Scattering angles

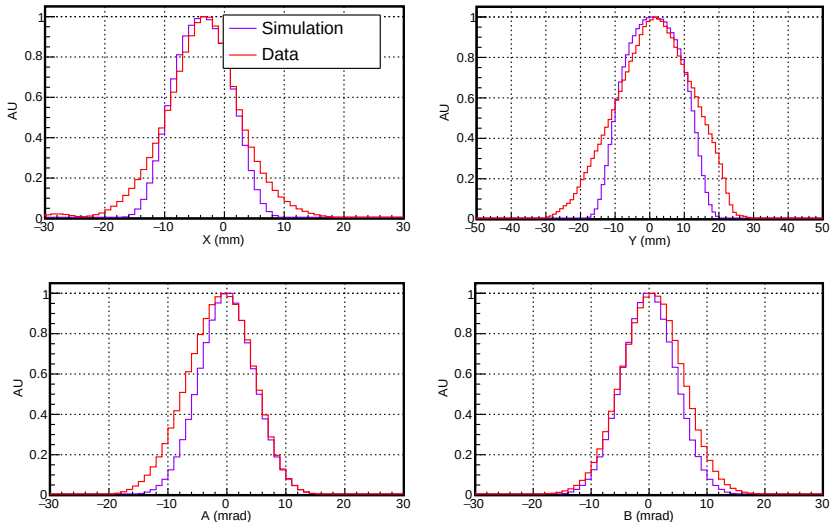

(b) Position in F8

Figure 3.26 – (a) Comparison between measured scattering angles for a given channel after the target, and the simulated ones after adjustment of the relevant parameters (see text for details). (b) Comparison between simulated positions and angles in F8 and measured ones. This is shown for the ^{84}Ge$\rightarrow^{82}$Ge channel as an example.

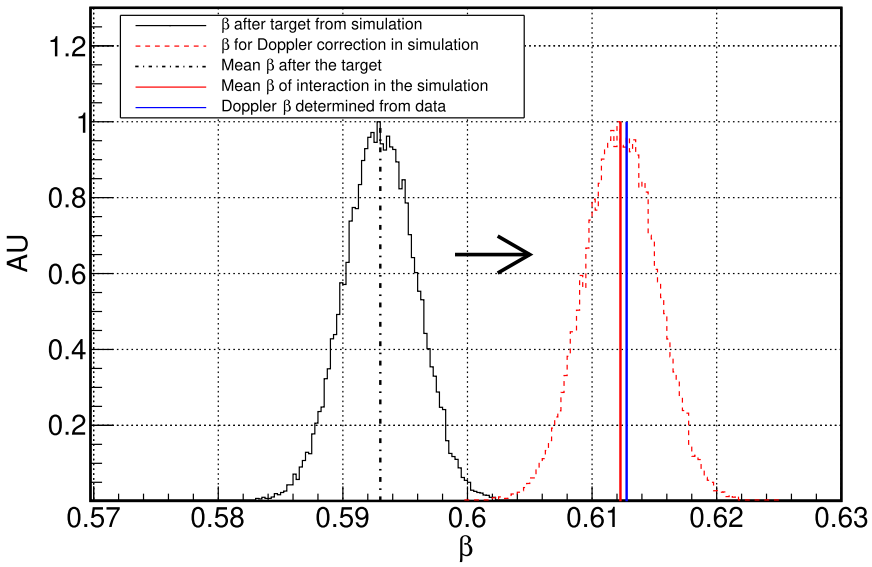

Figure 3.27 – Comparison between simulated velocities and measured ones. The black distribution is simulated by GEANT4 and set to be centred on the velocity after the target deduced from measurements. The red line shows the average velocity at which the nuclei interact in the target in the simulation, the blue line shows the mean velocity at which the reaction takes place deduced from measurements.

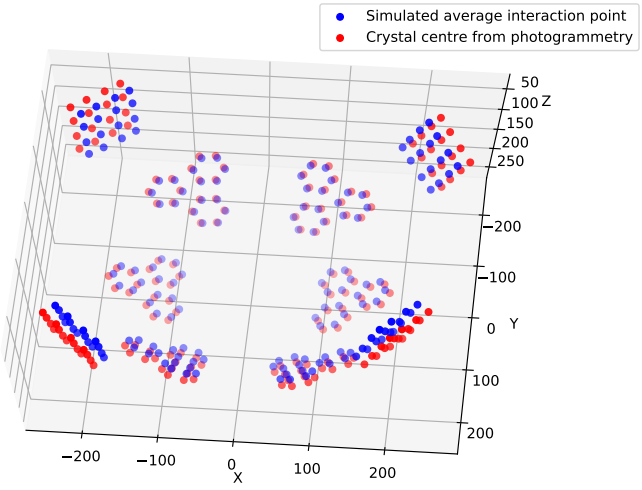

Figure 3.28 – Comparison, for MINIBALL and Clover detectors, between the simulated average position of the interaction in each segment (in blue) and the segment centre determined through photogrammetry (in red).

Chapter 4

Benchmark on ^{82}Ge and spectrum fitting procedure

The spectra in the centre of mass frame of the emitting nuclei are obtained *via* the analysis steps described in the previous chapter. Before tackling the reaction channel of interest leading to ^{83}Ge, a significant fraction of this thesis work is devoted to benchmark the Doppler correction and lifetime extraction methodology on a known case present in our data set. This chapter will describe the benchmark analysis on the low-lying transitions of ^{82}Ge produced after two-nucleon knockout from ^{84}Ge on a ^{9}Be target. This channel was chosen due to transitions at energies in the same range as the expected transitions of interest in ^{83}Ge (around 1 MeV) and its rather high statistics.

4.1 Presentation of the benchmark case

The level scheme of ^{82}Ge has been already explored in experiments for example *via* β-decay spectroscopy of ^{82}Ga [62, 63], β-n decay of ^{83}Ga [64], Coulomb excitation [65], transfer reaction [66], or knockout reactions at RIKEN with DALI2 [67]. This benchmark bears similarities with our main channel of interest in the sense that energies of the main transitions are already known with a precision below 1 keV mainly from beta decay at rest, and can be used as inputs for lifetime analysis. A reduced level scheme is shown in figure 4.1 with only the transitions relevant for this study.

The Doppler corrected energy spectra obtained through the analysis described in the previous chapter for ^{84}Ge(p, p2n)^{82}Ge are presented in figure 4.2 for each type of detector (MINIBALL, SuperClovers, and GRETINA-like) between 500 keV and 3000 keV. For every class of detector, two clear intense peaks close to 1348 keV and 938 keV are identifiable respectively with the $2^+ \rightarrow 0^+$ transition at 1348 keV [62] and the $4^+ \rightarrow 2^+$ / $6^+ \rightarrow 4^+$ doublet at 938/940 keV [62]. The transition from the 6^+ state (3225 keV) to the 4^+ state is

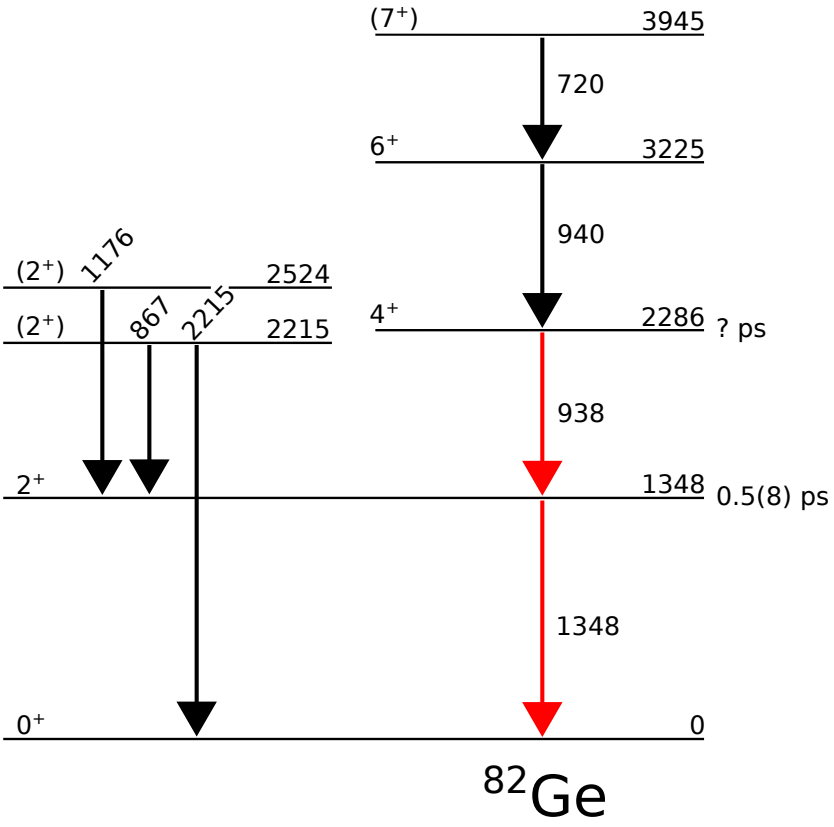

Figure 4.1 – Summary of the observed transitions in ^{82}Ge placed in the level scheme according to previous studies [62–68].

expected at 940 keV and therefore is not resolved by our detector setup and is superimposed with the 938 keV $4^+ \rightarrow 2^+$ transition. A part of this work will be dedicated to measuring the half-life of the 4^+ state by fitting this transition, which ultimately will result in an effective half-life of the $4^+ \rightarrow 2^+$ / $6^+ \rightarrow 4^+$ doublet peak.

Although we will focus on these two main transitions in the next sections, we also identified 4 other peaks in the experimental spectra corresponding to:

— 1176-keV transition from a state at 2524 keV to the 2_1^+ state [63, 66].

— 2215-keV and 867-keV from a state at 2215 keV to the ground and 2_1^+ state, respectively [63].

— a 720-keV peak matching with a transition recently observed in the work of D. Thisse [68, 69], assigned to a 7^+ state feeding into the main cascade being a candidate for a 1 particle-2 holes intruder structure.

The superior Doppler corrected energy resolution in GRETINA-like detectors helped identify without ambiguity some of those additional peaks. The consideration of those peaks also improves our spectrum fitting in the other detectors.

In order to study the cascades a coincidence spectrum is built from HiCARI events of multiplicity greater than 1 (same timestamped event but several crystals hit). Gamma-

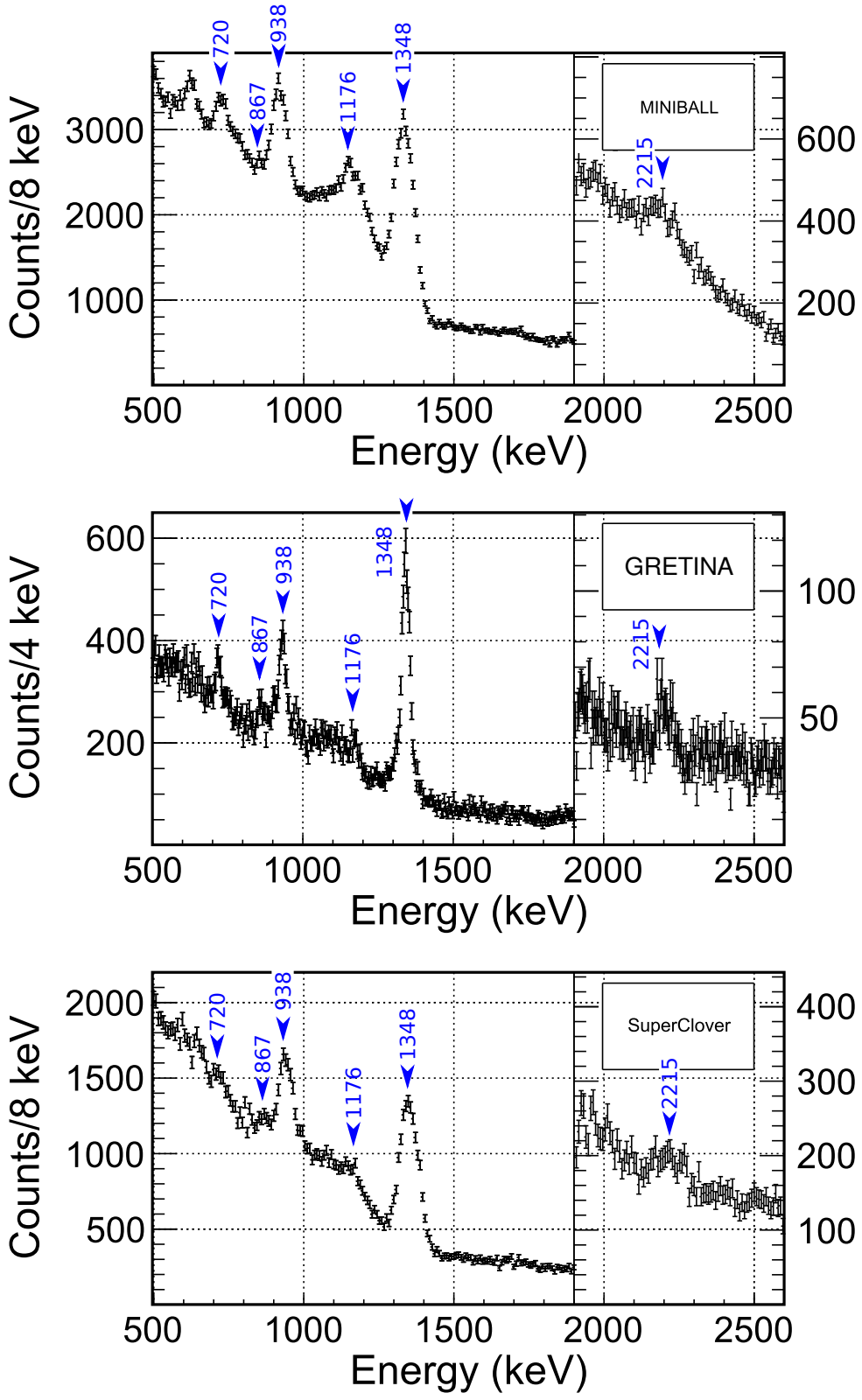

Figure 4.2 – Doppler-corrected γ-ray spectra for the channel ^{84}Ge(^{9}Be, X)^{82}Ge for each type of detectors separately. Observed transitions are described in the text and marked with arrows.

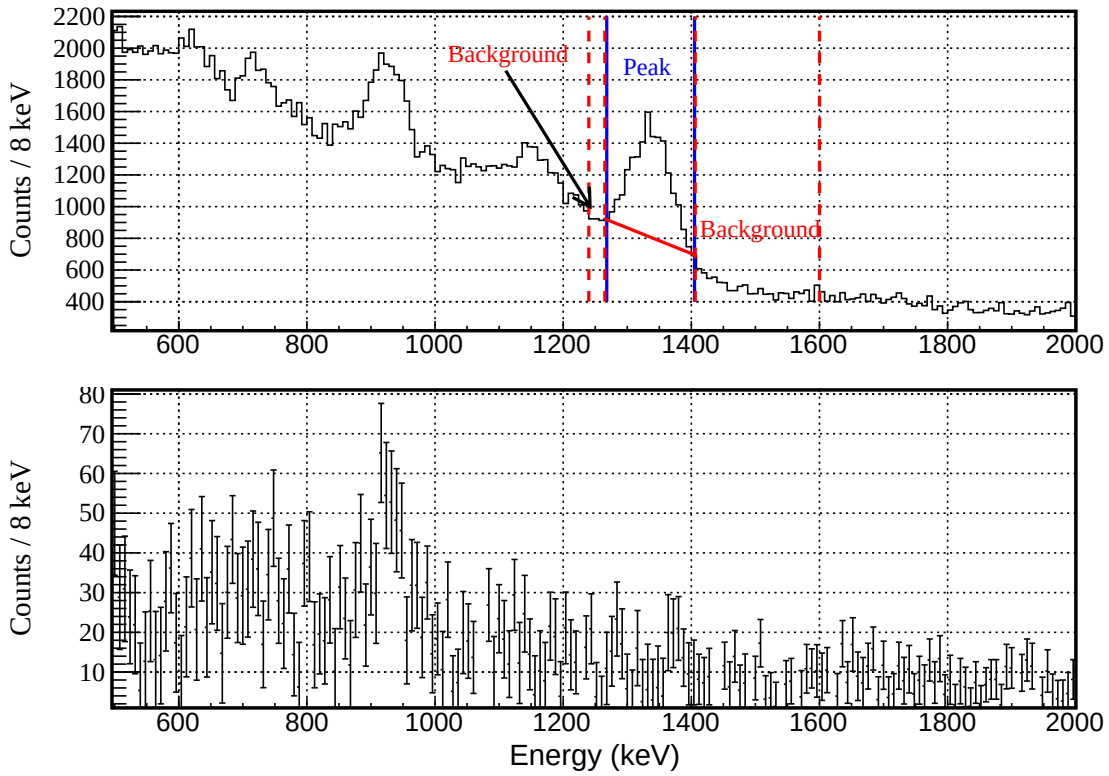

Figure 4.3 – On top: ^{82}Ge γ-ray spectrum with multiplicity superior to 1. In blue lines the gate around the peak used for γ-γ coincidences, in red dashed lines the gates for evaluating the background, in red solid line the evaluation of the background contribution under the peak. On the bottom: Gamma-gamma coincidence spectrum with a gate on the 1348 keV transition (MINIBALL and SuperClover data).

gamma coincidences are challenging with this setup due to the poor efficiency and high background level. On the bottom part of figure 4.3, the coincidence spectrum for a gate on the transition at 1348 keV in MINIBALL and Clover spectra (GRETINA-like detectors put aside) is presented (gates used are illustrated on the top part of figure 4.3) and we identify a strong coincidence with the 938/940 keV transition. Using a gaussian fit, we evaluate the number of hits in the peak in both the top and bottom spectra (integral above the red line and between the blue vertical lines). This results in 10360($\pm$275) hits in the 1348 keV peak. With an efficiency at this energy $\epsilon_\gamma = 1.84(15)\%$, we expect 191($\pm$9) detected hits in coincidence in the 938 keV doublet peak assuming no other branches feeding the 2^+ state. By integrating the 938 keV peak in the coincident spectrum we obtain 410($\pm$126) counts. The excessive amount of counts in the 938 keV doublet peak could be explained by a direct population of the 6^+ state (940 keV transition included in this coincident peak) but the large uncertainties from statistics and the integration procedure (background hypothesis) prevent us from further interpretation.

The half-life of the 2^+ state (1348 keV) is known ($T_{1/2} = 0.50(8)$ ps [65]) mainly from $B(E2)$ value measured from intermediate energy Coulomb excitation. Since it is the only known half-life in this nucleus, we will apply our half-life determination procedure to this state in the next section.

4.2 Spectrum fitting algorithm

This section will describe the method used to fit the γ-ray spectrum with a sum of simulated response functions for the transitions observed and an empirical background shape.

4.2.1 Background

In our experimental spectra, background contributions essentially arise from atomic processes producing low-energy γ rays (bremsstrahlung, radiative electron capture) or from unresolved transitions or γ-ray hits with partial energy deposit in the detector (Compton scattering or pair creation). The relative amount of these contributions and their exact sources cannot be precisely predicted or simulated. Instead, an effective and analytical shape for this background (equation 4.1) is assumed and used in the spectrum fit (details below).

The first step of our approach is to fit the background shape on a large portion of the spectrum going from 200 keV to 3000 keV. The high energy part is taken to be linear and is adjusted independently first between 2500 keV and 3000 keV.

The low energy part is modelled as the sum of two exponential functions. One of them

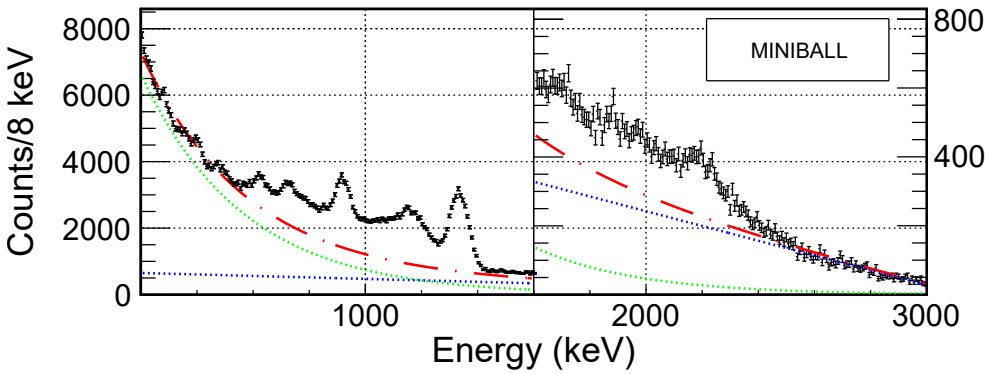

Figure 4.4 – First background estimation example for MINIBALL. Dash-dotted red line: the estimation of the background prior to transition fitting, blue dotted line: the linear contribution, green dotted line: the double exponential contribution.

has a large negative argument and accounts for the steep increase at low energy, and the other one is mainly relevant at intermediate energies in our spectrum (above 500 keV or below the peaks at about 1 MeV). This contribution to the background is adjusted between 200 keV and 500 keV.

In total the background function has seven parameters and writes as follow:

$$f_{bg} = \underbrace{p_0 + p_1 E}_{\text{linear}} + \underbrace{p_2 e^{p_3(E-p_4)}}_{\text{steep exponential}} + \underbrace{p_5 e^{p_6 E}}_{\text{slow exponential}} \tag{4.1}$$

The first estimation of the background can be seen in figure 4.4 for MINIBALL as an example. The Compton background present in the simulated response functions of the transitions will contribute to events outside of the peaks, hence the background estimated here must be modelled and refined progressively during the fit procedure when adding explicitly response functions of observed transitions.

4.2.2 Peak fitting procedure

Once the starting parameters for the background detailed above are found, we proceed to add simulated response functions of individual transitions. We treat separately the three groups of detectors MINIBALL, GRETINA-like and Clovers since they have very different sensitivity to lifetime effects, as it was mentioned in section 2.3.2 and will be shown in this section.

First of all, a new fitting function is created by adding to the background function the simulated response functions corresponding to the most intense transitions (here decay of the 1348 and 2286 keV states) and when possible going from higher to lower transition energies. All the parameters of the background are let free within 10% when adding the peaks since the Compton background also significantly contributes to the counts outside of

the peaks.

This step is done before adding less intense peaks to ensure that the background parameters are adapting to the additional contribution of the Compton background in a minimisation that doesn't involve too many parameters.

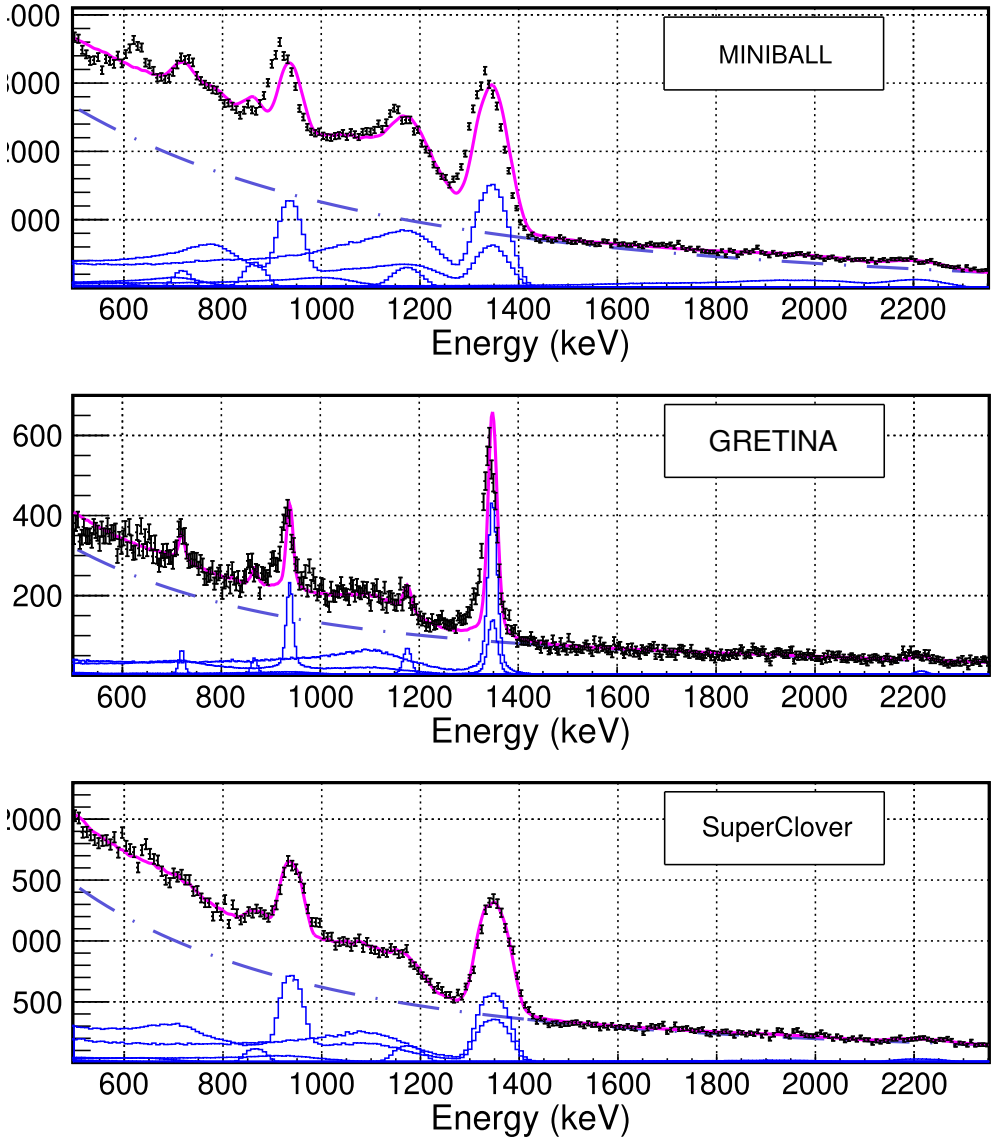

Figure 4.5 – Fits of the Doppler corrected γ-ray spectra in the range [500-2500] keV with response functions from simulations assuming $T_{1/2} = 0$ ps for all transitions. The pink line is the total fit function, the blue dashed-dotted line indicates the background contribution, and the blue histograms are the contributions of each transition to the total.

A least-square fit of the spectrum is then performed with the addition of all the simulated response functions of the transitions observed (listed previously) at their tabulated energies. An example of the resulting fit while considering every lifetime to be zero is shown in figure 4.5 (the addition of the lifetime will be discussed later).

At this stage, it is worth pointing that we only include the main $4^+ \rightarrow 2^+ \rightarrow 0^+$

cascade in the fit explicitly and all other transitions are simulated individually. This is why in figure 4.5 the $2^+ \rightarrow 0^+$ peak region around 1350 keV is fitted with components of two different response functions: (i) the direct component assuming that the reaction feeds the 2_1^+ state and (ii) the indirect component assuming feeding of the 4_1^+ state and a subsequent cascade *via* the 2_1^+ state.

The three groups of detectors are separated to highlight their different sensitivities to the lifetime. For the MINIBALL detectors, as it was discussed in section 2.3.2, an energy offset between the fit function and the data indicates a lifetime effect that is not (yet) reproduced by the simulated response functions. For the GRETINA detectors a tail on the low-energy side of the peaks is not reproduced by the response function which matches our expectations as well on how a significant lifetime affects this spectrum. The Clover spectrum appears well reproduced to the eye by these no-lifetimes simulations. This is to be expected since they are placed at an angle where the energy shift caused by a lifetime is too small to be detected, and they don't have the resolution to show the formation of a tail for short lifetimes. The poor sensitivity of Clover detectors will be highlighted again when the procedure will be applied for the determination of a half-life.

4.2.3 Half-life determination for the 2_1^+ and 4_1^+ states

This section will present the method used to determine the half-lives of the 2_1^+ and 4_1^+ states and compare the result obtained for the 2_1^+ state to the literature value of 0.5(8) ps.

In order to determine the half-life of a state, successive fits are performed while varying only the simulated half-life of the studied state. The transition energy in the simulation is kept fixed at the tabulated energy. A graph of the χ^2 values obtained from the minimisation as a function of the half-life shall show a minimum for the half-life that reproduces the observed peak shape best. To ensure that the χ^2 profile has a maximal sensitivity to the lifetime of the state studied, these successive fits are performed in a reduced region around the peak of interest. This is done while fixing the intensities of other transitions outside this range from the global fit, and letting the background fluctuate within 10%.

Procedure for the 4_1^+ state

As mentioned previously, there is a feeding essentially from the 4^+ state to the 2^+ state. Therefore if we had applied the lifetime determination procedure directly to the $2^+ \rightarrow 0^+$ transition we would observe an effective lifetime due to cascade events. Inevitably, one has to determine first the lifetime of the 4^+ state. In this specific case, the fact that the $6^+ \rightarrow 4^+$ and $4^+ \rightarrow 2^+$ transition can't be resolved presents an additional difficulty. We decided to fit the 938/940 keV doublet peak with only a single simulated response function for the $4^+ \rightarrow 2^+$ transition. By doing so, we know that the lifetime we will extract from

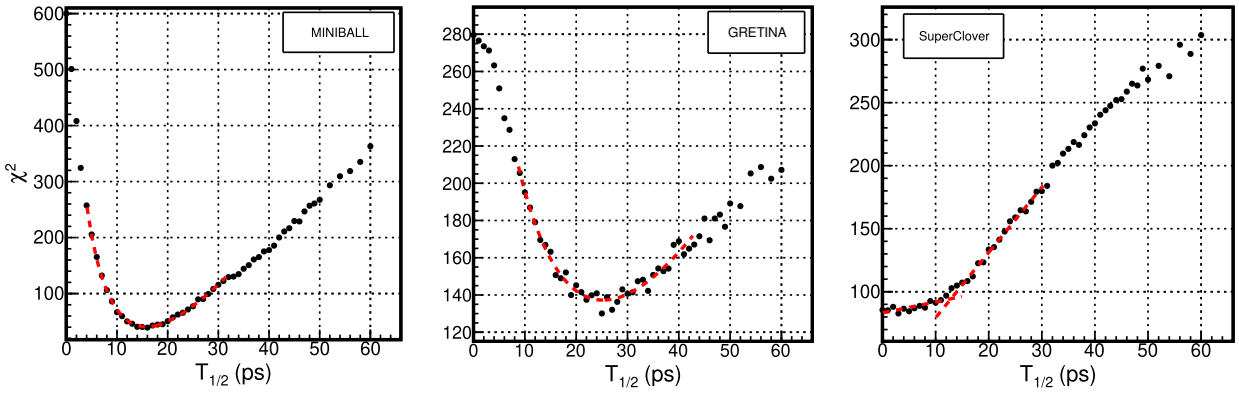

Figure 4.6 – χ^2 obtained against the simulated half-life of the 4^+ state for each detector. The fit is performed in a restricted range around the 938-keV peak: [750-1100] keV. The red line shows the function used for determining the minimum position. Due to the Clover's rather poor sensitivity for lifetimes in the 0-15 ps range, we propose two linear fits in order to evaluate an upper boundary (see text for details).

the χ^2 procedure is effective and includes also the indirect lifetime effect of the 6^+ state. However this 6^+ contribution is anticipated to be smaller than that of the 4^+ because past knockout reaction studies of neighbouring nuclei ([70–73]) showed no or very small direct population of 6^+ states and higher spins in even-even nuclei compared to $4^+/2^+$ states. Given that our gamma-gamma analysis presented before is not precise enough to conclude on the relative $6^+/4^+$ population, we relied on this previous feeding pattern and assume in the rest of this document that the 4^+ lifetime dominates the peak shape and position.

The resulting χ^2 profiles for each detector group separately are shown in figure 4.6 for the 938-keV transition fitted in the range [750, 1100] keV. The seemingly random jittering of the χ^2 points for GRETINA detectors is due to limited statistics in the response function. This should be improved later by increasing the number of simulated events [1] and when P3 signals from detectors will be decomposed as well and added to the analysis. As expected (see section 2.3.2), Clover detectors are mostly insensitive to low lifetimes due to the angle at which they are positioned.

In order to determine the minimal χ^2, the asymmetric profiles obtained for MINIBALL and GRETINA are fitted around their minimum using an asymmetric polynomial function:

$$f(\chi^2) = \frac{1}{2}\frac{(\chi^2 - T_{1/2}^{min})^2}{p_1 p_2 + (p_1 - p_2)(\chi^2 - T_{1/2}^{min})} + \chi^2_{min}\,, \tag{4.2}$$

where p_1 and p_2 are coefficients characterising each side of the function around the minimum, $T_{1/2}^{min}$ is the position of the minimum, and χ^2_{min} is the χ^2 achieved at the minimum.

With this method we obtain a half-life for the 4^+ state of 16(2) ps for the MINIBALL

1. Currently 10^7 events were generated in the simulation to produce each response function

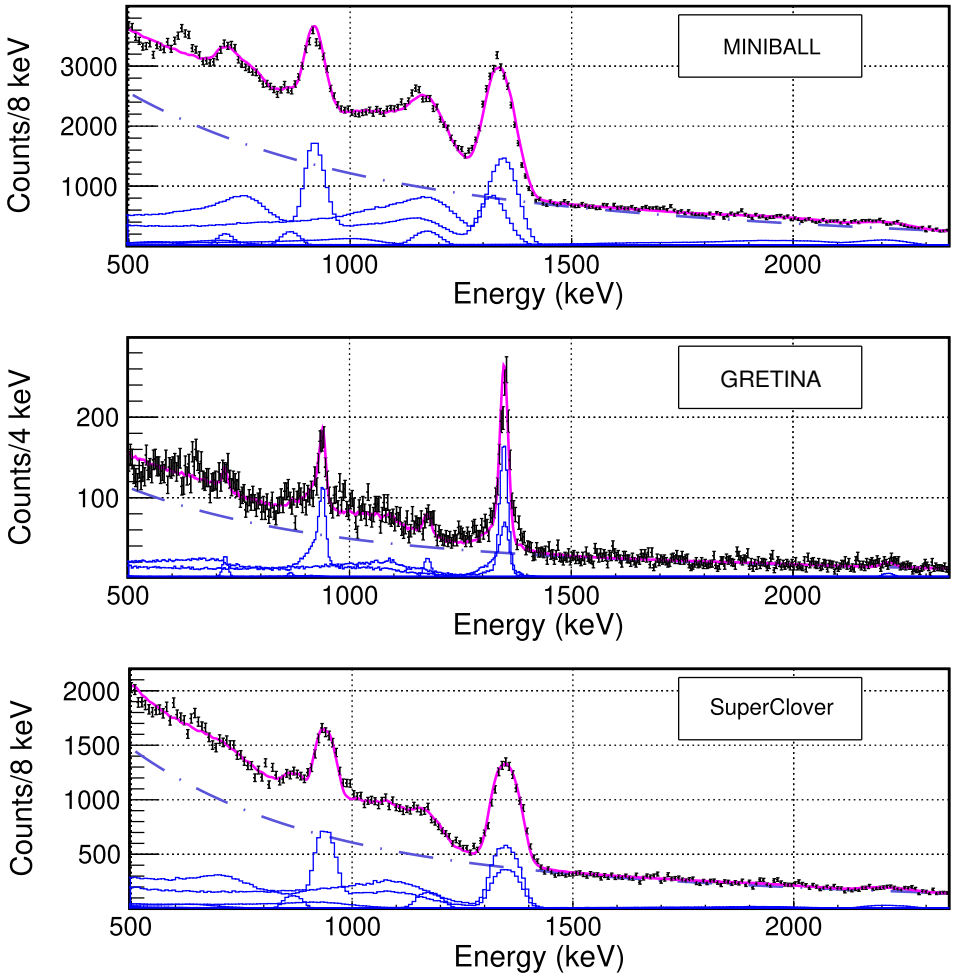

Figure 4.7 – Optimal fit on the range [500-2500] keV for each detector considering a half-life of the 4^+ state determined *via* the procedure described in the text.

group, 24(3) ps for the GRETINA quad. The fit of the spectrum using these half-lives on the 4^+ state in the simulation is presented in figure 4.7. At this stage of the discussion, the 1-σ uncertainties quoted here are purely statistical. They were determined by varying the $T_{1/2}$ away from the χ^2_{min} until it reaches $\chi^2_{min}+1$. This optimal $T_{1/2}$ value and this statistical error definition assume that the transition energy is known (fixed in the fit) and so the $T_{1/2}$ is a single independent parameter. Other prescriptions and systematic uncertainties which could explain the incompatibilities observed between the different detector groups will be addressed in detail later in section 4.3. Using equation 4.2 parameters in order to determine the $\chi^2_{min}+1$ error bars positions yields:

$$f(\chi^2) = \chi^2_{min} + 1 \implies (\chi^2 - T^{min}_{1/2}) = p_1 - p_2 \pm \sqrt{p_1^2 + p_2^2} \tag{4.3}$$

This $\chi^2_{min}+1$ method results in asymmetric errors around the $T_{1/2}\,(\chi^2_{min})$ value. For a simple representation we choose to make it symmetric by using the largest value.

For the SuperClover group, given its insensitivity to short $T_{1/2}$ depicted by the flatness of the profile below 13 ps in figure 4.6, we only determine a rough upper limit window for the moment.

Procedure for the 2_1^+ state

Using the determined half-life of the 4^+ state, we can now apply the fitting procedure to the $2^+ \rightarrow 0^+$ transition by iterating on the simulated half-life of the 2^+ state. This gives a χ^2 curve against the 2^+ state half-life presented in figure 4.8 with MINIBALL on the left and the GRETINA Quad result on the right. The minima of these curves are obtained using the function defined in equation 4.2 (in red in the graphs).

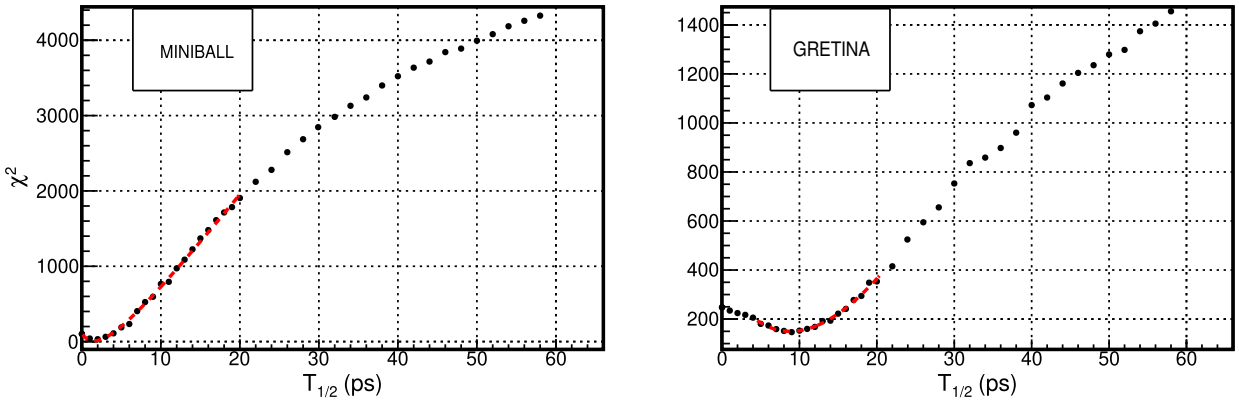

Figure 4.8 – χ^2 obtained against the simulated half-life of the 2^+ state for each detector. The fit is performed on a restricted range around the $2^+ \rightarrow 0^+$ peak: [1250-1400] keV. The red line shows the function used for determining the minimum position. For MINIBALL the response functions assume a half life of the 4^+ state of 16 ps, and for GRETINA they assume a half life of the 4^+ state of 24 ps.

This results in an optimal half-life of the 2^+ state of 1.5(2) ps with MINIBALL, and 8.8(7) ps with the GRETINA detectors. We ignored Clover detectors for sensitivity reasons highlighted before. All the determined $T_{1/2}$ values are summarised in table 4.1 below. The

	4^+	2^+
MINIBALL	16(2) ps	1.5(2) ps
GRETINA Quad	24(3) ps	8.8(7) ps
Difference (GR-MB)	8 ps	7.3 ps

Table 4.1 – Summary of the half-life measured on the 4^+ and 2^+ states using the procedure described in the text.

two groups of detectors measure half-life values that are incompatible, with a similar offset between the two states (respectively 8 and 7.3 ps). However the 2_1^+ half-life determined using MINIBALL detectors (1.5(2) ps) is much closer to the tabulated value of 0.5(8) ps. Additionally, the fit quality is also better for MINIBALL in general with lower minimal

χ^2/N values compared to GRETINA ones (χ^2/N of about 1.2 for MINIBALL against 1.75 for GRETINA-like).

These results indicate that the overall methodology (reconstruction, simulation, fit) is valid for MINIBALL data but the significant differences with other groups (GRETINA, Clovers) point to systematic errors or problems. Their possible origin is discussed in the following section.

4.3 Systematic uncertainties and incompatibilities

The half-life values measured by applying the method to data from different groups of detectors are 1σ incompatible considering only statistical uncertainty. In this section we will discuss the probable causes of such differences.

4.3.1 Tests related to the position systematic error

As discussed in section 2.3.2, the γ-ray angle determined for the Doppler correction is highly dependent on the positioning of the detectors with respect to the target. As briefly mentioned earlier, the photogrammetry measurement precisely determines the position of markers located on the outer shells of the Ge clusters (within $\sigma = 0.1$ mm [74]) but the transformation to actual crystal positions relative to the target centre leads to additional uncertainties:

— A 3D model or technical drawings of the cluster with the theoretical positions of the crystals within the shell is needed to go from the marker position to the crystal positions via a minimisation procedure (multidimensional χ^2). This theoretical crystal position in the cluster frame can be off from the true crystal centre because: (i) in reality the crystal is cooled at nitrogen temperature (modifying its dimensions), (ii) the drawings from companies are sometimes imprecise due to industrial confidentiality, (iii) the depletion volume (active) is not exactly the same as the full crystal volume, etc.

— The multi-dimensional fit between markers position and 3D model leads to additional uncertainties.

— The target frame was simply inserted manually inside the beam tube with a rod of known length and thus the relative position of the target centre to the reference beam tube is not as precise as marker positions.

These errors cannot be exactly quantified, but in our opinion, they could be of the order of a millimetre. To quantify the sensitivity of our extracted half-lives to such detector-target position uncertainty, we investigate in this section the impact of shifting the target along Z-axis in the analysis with respect to nominal values.

Such a shift in position would affect differently detectors placed at high angles and at low angles: the detectors at high angles are expected to be more impacted than the lower angle ones. We apply the same procedure as in the previous section to measure half-lives of both the 2^+ and 4^+ states assuming a shift of +1 mm of the position of the target along the Z-axis. The results are listed in table 4.2. Comparing the groups of detectors MINIBALL and GRETINA-like, the agreement between the two becomes significantly better as well as the agreement with the previously measured value of 0.5(8) ps for the 2^+.

	Target shifted: +1 mm		Nominal target position	
	4^+	2^+	4^+	2^+
MINIBALL	14(2) ps	1.0(2) ps	16(2) ps	1.5(2) ps
GRETINA Quad	17(3) ps	3.4(7) ps	24(3) ps	8.8(7) ps
Difference (GR-MB)	3 ps	2.4 ps	8 ps	7.3 ps

Table 4.2 – Summary of the half-lives measured for the 4^+ and 2^+ states assuming an shift of the position of the target of 1 mm along the Z axis.

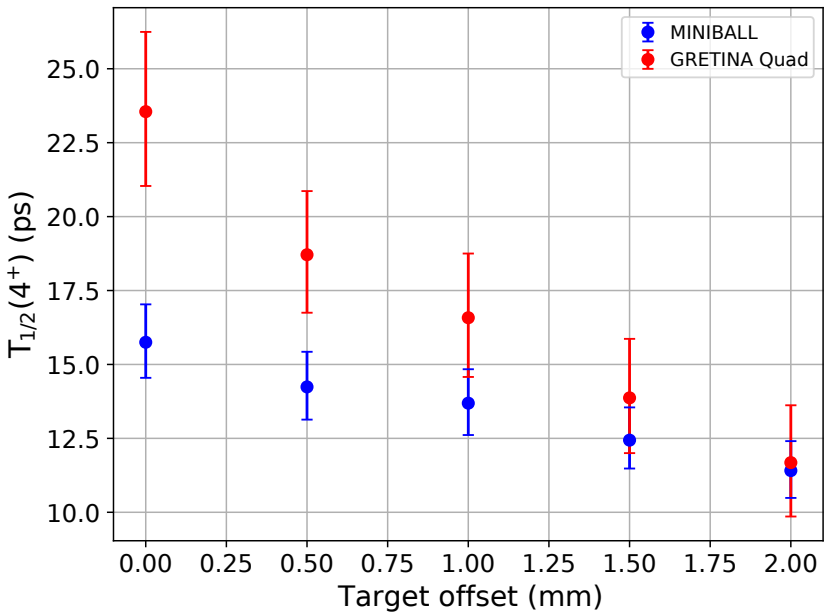

Figure 4.9 – Half-life of the 4^+ state in ^{82}Ge obtained through the analysis of data from MINIBALL detectors (in blue) and GRETINA detectors (in red), plotted against a shift of the target along the Z-axis.

In addition, figure 4.9 shows the 4^+ state's half-life measured using MINIBALL and GRETINA detectors against a shift of the target along the beam-line axis in steps of 0.5 mm. The values measured with the two types of detectors become 1-σ compatible at a shift of about +1 mm. It is also worth noting that while the absolute χ^2_{min} value reached for MINIBALL data is not much affected by these tests, it reaches a minimum at +1 mm

for the GRETINA detector (χ^2/N goes from 1.75 at the nominal position to 1.6 when offset by 1 mm).

This target shift along the Z-axis reduces the measured half-life especially for high angle detectors. The 2^+ half-life measured with GRETINA-like detectors is closer to the expected value, thus assuming a systematic error as we did seems to improve our benchmark results.

In order to explore further the impact of the shift along the Z-axis on the determined half-life, we separate the detectors further into subgroups: low angle MINIBALL ($\theta < 32\,\mathrm{deg}$), high angle MINIBALL, SuperClover, low angle GRETINA crystal, and high angle GRETINA crystal. The half-lives of both states are determined for each subgroup and presented in figure 4.10 where each point corresponds to a subgroup, and black dots are with nominal positions and red dots are with the +1 mm target shift assumption.

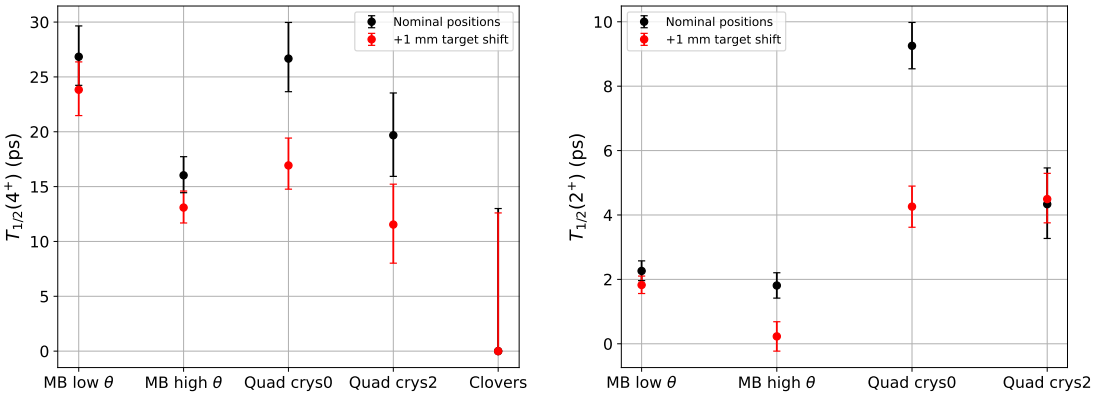

(a) 4^+ results **(b)** 2^+ results

Figure 4.10 – Half-lives and their uncertainties obtained for different groups of detectors: low angle MINIBALL ($\theta < 32.5\,\mathrm{deg}$), high angle MINIBALL ($\theta > 32.5\,\mathrm{deg}$), GRETINA quad crystal 0 ($\theta \approx 60\,\mathrm{deg}$), GRETINA quad crystal 2 ($\theta \approx 80\,\mathrm{deg}$), and SuperClover ($\theta \approx 70\,\mathrm{deg}$). In black results with the nominal relative positions of the target and the detectors, in red assuming a shift of the position of the target of 1 mm along the Z axis.

Separating the detectors as such shows differences within groups of detectors. Some of the observed effects can be understood but some remain unexplained. For example for the 2^+ state, low and high MINIBALL angle group are in agreement when using nominal positions but when a +1 mm offset is added, the higher angular group is more strongly affected for simple geometrical reasons. In contrast for the longer-lived 4^+, we still don't know the origin of the difference between low- and high-angle MB detectors already at nominal positions and they are similarly affected by the offset.

More generally speaking, the global target shift tends to reduce the difference between MINIBALL and GRETINA half-lives but the overall agreement between angular groups is not completely satisfactory.

4.3.2 Tests related to velocity systematic error

Another source of systematic uncertainties would be an error on the velocity. In order to test it, we offset the β used for the Doppler correction by +0.001 which corresponds to approximately 0.16% of the initial value (comparable to the 0.1% differences between values found using energy loss calculations and measured ones, see section 3.3.3).

	β shifted: +0.001		Previously determined β	
	4^+	2^+	4^+	2^+
MINIBALL	17(2) ps	2.2(2) ps	16(2) ps	1.5(2) ps
GRETINA Quad	22(3) ps	8.1(7) ps	24(3) ps	8.8(7) ps
Difference (GR-MB)	5 ps	5.9 ps	8 ps	7.3 ps

Table 4.3 – Summary of the half-lives measured for the 4^+ and 2^+ states assuming a shift of β of +0.001.

Table 4.3 shows the obtained half-lives assuming a systematic shift of +0.001 on the velocity β. While this makes the half-lives of the 4^+ state measured in each group of detector closer, it is marginal and would require a larger shift which would exceed what we can accept. On the other hand, the half-lives of the 2^+ state measured using MINIBALL detectors is slightly further away from the expected 0.5(8) ps while the one measured using the GRETINA Quad stays unchanged (considering the rather large error). While an acceptable systematic error on the velocity leads to a shift in the right direction, it does not solve the matter on its own and therefore is not the cause of the disagreement between data from different detectors. We hence decided not to shift the velocity in the further analysis.

4.4 Preliminary conclusions

This benchmark case put the spotlight on a disagreement between the two groups of detectors. A +1 mm shift of the target position (comparable to a shift of 1.2 mm found in the RIBF170 experiment with another method [75]) makes the two groups of detectors 1-σ compatible. It is worth noting that we did not investigate a possible position offset between the two groups of detectors. In the collaboration, MINIBALL detectors have been used with success in other benchmark cases, in this study they also give a benchmark result that is closer to the expected half-life of the 2^+ state, while being a lot less affected by an uncertainty of the position of the target. On the other hand, GRETINA-type detectors have been a lot more challenging to operate since the online decomposition faced some problems and has not been done again since (offline codes need to be adapted), and the positioning of those detectors in the simulation is lengthy and there is room for errors. Overall we have much more confidence in the half-lives measured using MINIBALL detectors and while

data from all types of detectors will still be analysed, this gives some arguments to base the discussion on MINIBALL results rather than those from GRETINA-like detectors.

The analysis being tested on the benchmark case, the next section will apply the same procedure to the main case of interest: the intruder candidates in ^{83}Ge.

Chapter 5

Analysis of the channel of interest ^{84}Ge→^{83}Ge

This chapter will apply the procedure described previously for the benchmark case to the ^{83}Ge channel. The main goal is to extract the half-lives and exclusive cross sections for the states populated by neutron removal, and identify from these observables possible intruder states.

5.1 Presentation of the spectrum and identification of the transitions

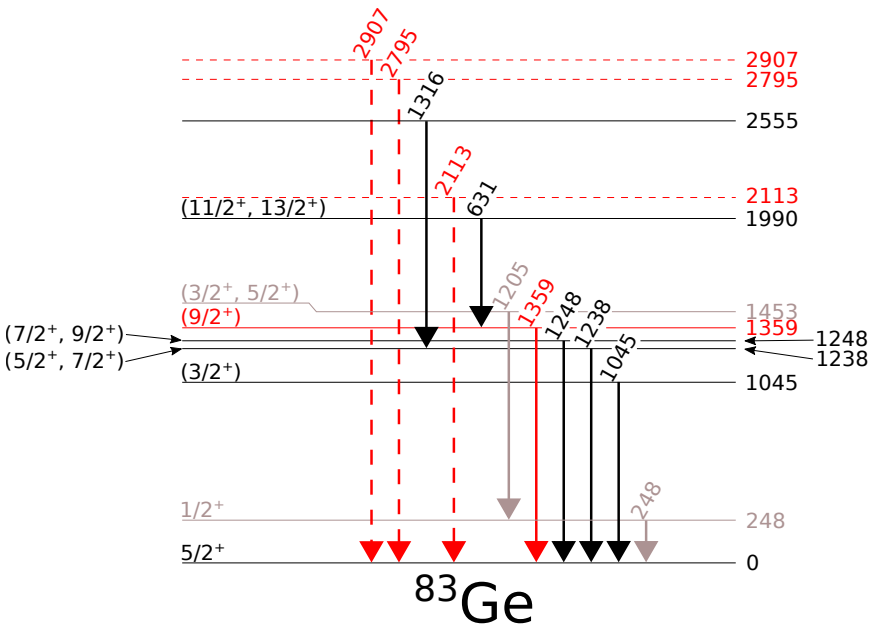

Figure 5.1 – Reduced level scheme showing the identified transitions in the ^{83}Ge spectra. Solid lines: previously observed transitions. Dashed lines: tentative placement of newly observed transitions. Red: intruder candidates considered from previous studies and theoretical calculations. Grey: known transitions not observed here.

As mentioned before, the γ-ray spectrum of ^{83}Ge has been studied through β-decay spectroscopy of ^{83}Ga [3, 76] giving us a set of transitions of very well known energies and decay pattern. In the level scheme (figure 5.1) we show transitions considered in this study with solid lines representing transitions already observed in β decay. The first excited $1/2^+$ state at 248 keV shown in grey on the level scheme is expected to be significantly populated in our experiment. However since its half-life is expected to be very long (several nanoseconds) it will decay mostly after the setup (at $\beta \approx 0.6$, $v \approx 18$ cm/ns) and we do not distinguish its decay from the background.

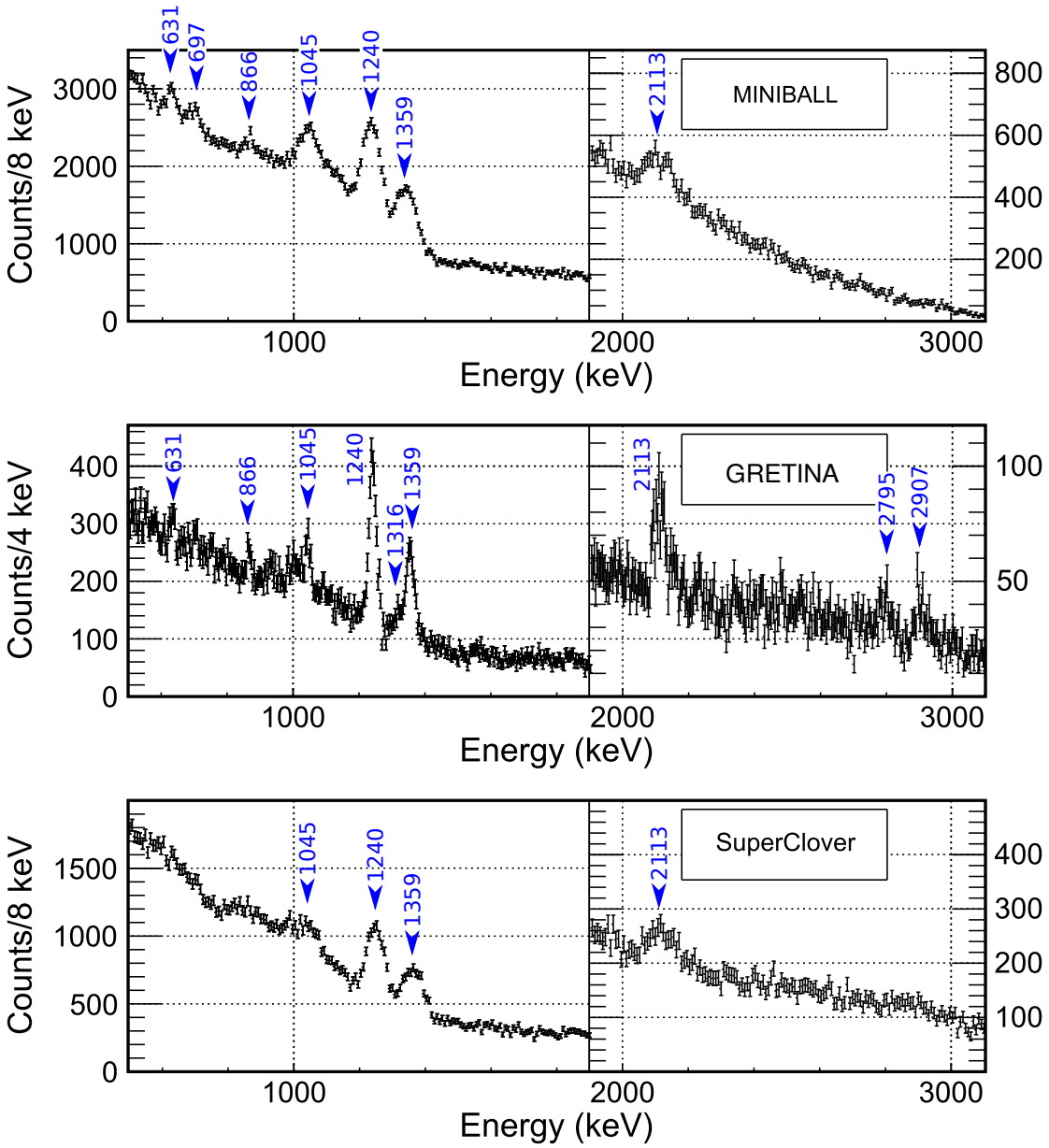

Figure 5.2 – Doppler corrected spectra for the ^{84}Ge(Be, X)^{83}Ge channel for each of the three groups of detectors separately. Observed transitions are marked with an arrow and described in the text.

In figure 5.2 we present the Doppler-corrected γ-ray spectra for each group of detectors. We observe a transition very close to the expected energy of the main intruder candidate (expected at 1359 keV according to the PhD work [3]). Despite the presence of the 1316-keV peak, one can identify a tail on the low energy end of the peak clearly indicating a lifetime effect.

In addition to the main intruder candidate at 1359 keV, some other peaks are present that we can associate with transitions observed in previous β-decay measurements:

— A transition at 1045 keV identified *via* both the β-decay of ^{83}Ga [3, 76] and β-n of ^{84}Ga [77].

— A peak at about 1240 keV matches two known transitions at 1238 keV and 1248 keV. Our energy resolution after Doppler correction does not allow the discrimination between the two.

— A peak at about 630 keV matches a 631 keV transition feeding the intruder candidate at 1359 keV measured in [3].

— A low-intensity peak at 1316 keV was measured in coincidence with the 1238 keV in [3] and can be observed at the edge of the 1359-peak in the GRETINA spectrum.

We also include in our analysis some weaker peaks that we did not assign to previously measured transitions. The energies of those peaks or half-lives of the corresponding states are not studied here and we include them mainly in the context of the discussion of the spectroscopic strength. Therefore we simulate the response function at energies that we measure using a simple gaussian (and linear background) fit, and the energies listed here should not in any way be considered final.

— A peak at 697 keV observed clearly in the MINIBALL spectrum (not placed in the level scheme).

— A clear peak at 866 keV in all spectra transition (not placed in the level scheme).

— A relatively intense peak at 2113 keV, clearly identifiable in all spectra.

— Two high energy transitions visible only in the GRETINA quad spectrum at 2795 keV and 2907 keV.

As previously discussed, theoretical calculations predict intruder strength at high excitation energies ($\approx$ 3 MeV). We choose here to present states with excitation energies $E > 2$ MeV and relative intensity greater than 5% as intruder candidates.

Due to the low statistics collected in the peaks expected to be in coincidence with one another, the low efficiency of HiCARI and the high background, gamma-gamma coincidences are still rather challenging to perform, and we do not realistically expect to observe the coincidence between two γ rays. In this case in particular, the peaks at 1238/1248 keV and 1359 keV are close to each other and gating on those transitions can be a stretch. Nevertheless spectra in coincidence with 1045-keV, 1238/1248-keV, and 1359-keV γ rays

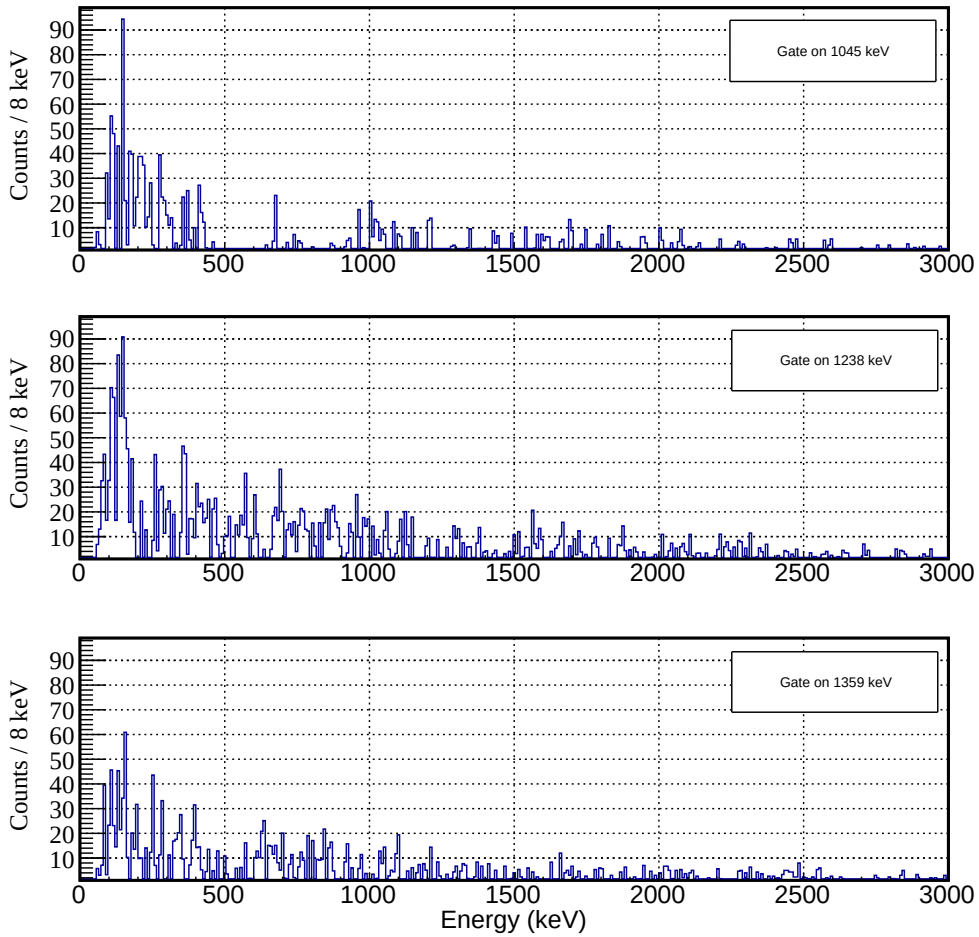

Figure 5.3 – ^{83}Ge spectra (all detectors apart from GRETINA-like detectors) gated on the three most intense transitions: 1045 keV, 1238/1248 keV, and 1359 keV.

are shown in figure 5.3 with background reduction. The figure highlights the difficulty to make conclusions from γ-γ coincidences in this experiment.

The analysis will therefore be performed by simulating all the transitions to the ground state. This works for most of the transitions according to the previous β-decay works in the region. For the half-life measurements, only a considerable half-life effect on the 631 keV peak would impact the study of the 1359 keV transition. Considering the low intensity of the 631-keV transition and the absence of a visible half-life effect on the corresponding peak shape, we neglect its impact.

5.2 Analysis of the spectra

5.2.1 Half-life determination for the main intruder candidate at 1359 keV

This section will show the results of the half-life determination procedure described in section 4.2.3, applied to the transition at 1359 keV.

The steps in the spectrum fit are the same as in the case of ^{82}Ge with a simplification that there is no intermediate feeding to take into account.

A first fit presented in figure 5.4 is performed assuming no lifetime effect for any of the states simulated. Most of the peaks are very well reproduced, which indicates that considering their negligibly short lifetimes is sufficient to reproduce the spectra. A closer look at the 1359-keV peak region shows that in MINIBALL the 1316-keV peak strength is overestimated in order to compensate a shift of the 1359-keV peak, and in the GRETINA detector, the same 1316-keV peak is overestimated by the minimisation in order to compensate for the visible tail of the 1359-keV peak. Both cases show a relatively bad reproduction of the transition at 1359 keV and strongly indicate lifetime effects as expected.

The iterative fitting procedure is hence applied to the 1359-keV peak, while assuming no lifetime effect on all the other peak shapes. The resulting χ^2 curves are shown in figure 5.5, and their minima correspond to a half-life of the 1359 keV state of 7.0(9) ps with MINIBALL and 22(2) ps with the GRETINA Quad. The upper limit provided by the SuperClover detectors is about 15 ps. The fitted spectra for these optimal chi-square results are presented in figure 5.6 and demonstrate that the data is much better reproduced than without taking state lifetime into account. As one can see, the fits clearly favour the presence of a strong 1359-keV peak shifted (and/or distorted) by the lifetime effect, and a very weak 1316-keV transition.

We provide in table 5.1 the relative intensities of each peak included in the fit with respect to the total intensity of all peaks. In the fit, the 1238-keV and 1248-keV transitions have been both included with a negligibly short lifetime, leading to a strong contribution of the 1238-keV transition. In section 5.2.3 we provide a discussion of the nature of this peak and the relative contributions of each transition.

5.2.2 Discussion of the lifetime incompatibilities

Target offset

The half-life values obtained for MINIBALL and GRETINA from the analysis of the 1359-keV transition are also 1-σ incompatible. In the ^{82}Ge benchmark case, an acceptable shift of the target along the beam-pipe axis offered a plausible solution of the issue. We

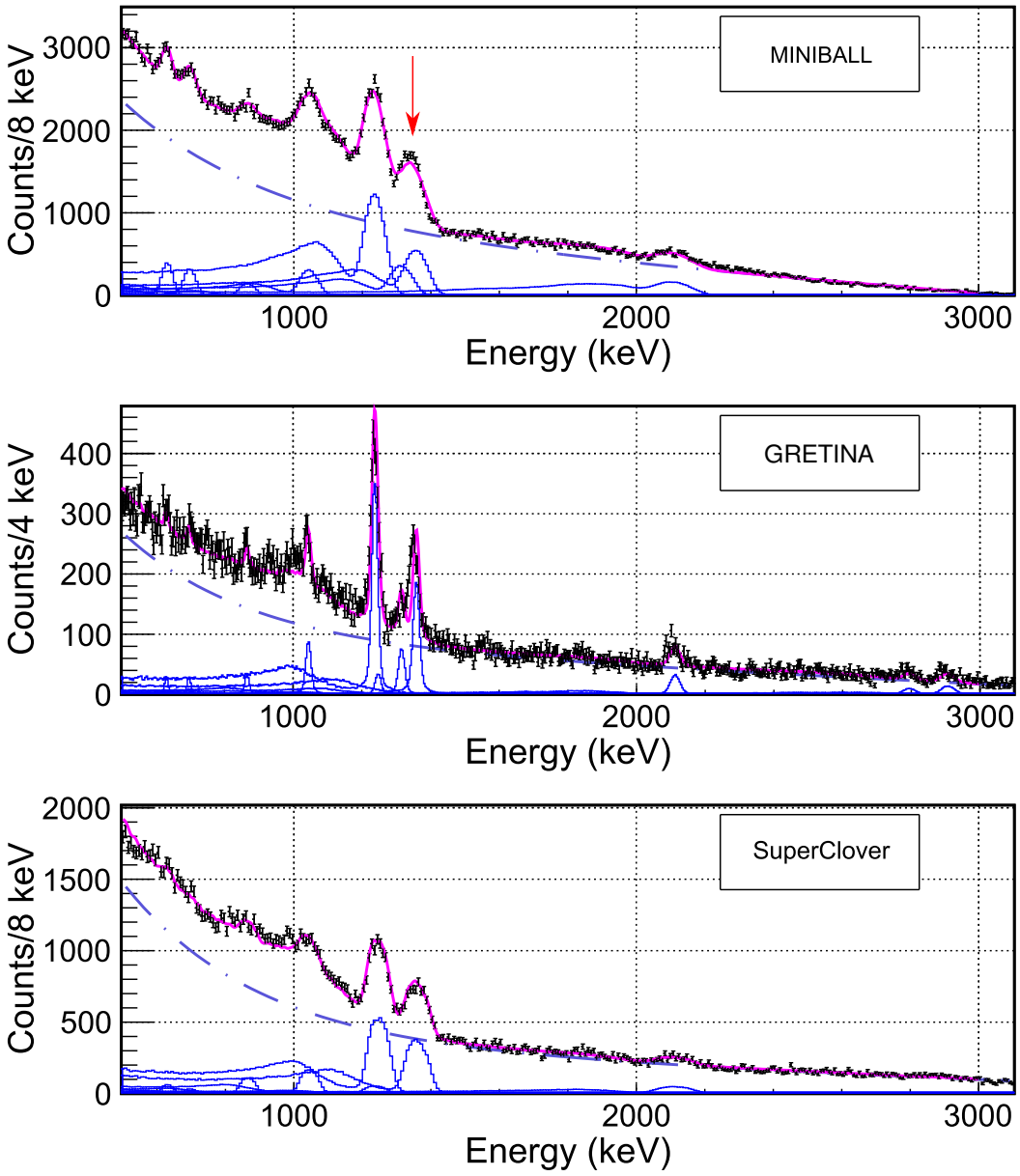

Figure 5.4 – Fit of the Doppler corrected γ-ray spectra in the range [500-3000] keV with response functions from simulations assuming $T_{1/2} = 0$ ps for all transitions. The pink line is the total fit function, the blue dashed-dotted line indicate the background contribution, and the blue histograms are the contributions of each transitions to the total.

therefore provide here a study of the effect of the target offset on the measured half-life of the 1359-keV state.

In figure 5.7 we show the half-lives measured for each group of detectors against the target offset with respect to the nominal position. In order to reach an agreement between the two groups of detectors by moving only the target, a considerable (and not conceivable) offset would need to be applied (more than 2 mm). We hence consider that the agreement

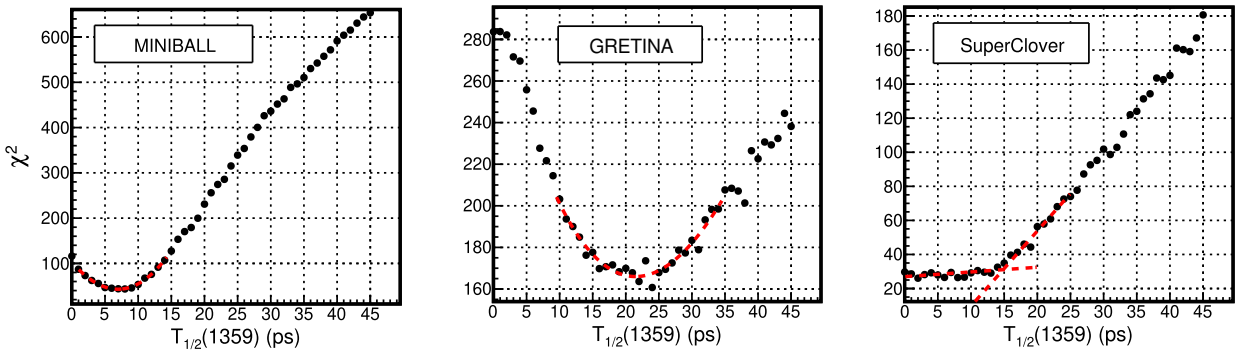

Figure 5.5 – χ^2 obtained against the simulated half-life of the 1359-keV state for each detector. The fit is performed in a restricted range around the peak of interest ([1200-1500] keV). The red line shows the function used to determine the minimum. For Clover detectors, since they are not much sensitive to lifetimes of the order of the ones we study here, we determine an upper limit from the crossing of the two lines shown here.

Energy (keV)	Relative intensity (%)	
	MB	GRETINA
631	4.5(4)	1.5(6)
697	4.2(4)	1.6(6)
866	2.5(4)	2.3(6)
1045	7.1(5)	6.9(7)
1238	33(2)	36(1)
1248	6.9(2.5)	2.5(1.3)
1316	<1	1.2(6)
1359	29(1)	32(1)
2113	12(1)	7.4(7)
2795	-	3.5(7)
2907	-	5.1(9)

Table 5.1 – Intensity of the simulated response functions in the optimal fit, relative to the total.

cannot be reached this way, thus indicating a non compensated effect between the detector types.

1316-keV peak

The presence or absence of a transition at 1316 keV can reasonably be discussed since it is hardly visible on the spectra. Here we discuss briefly its impact on lifetime measurements.

As pointed previously, an incompletely resolved transition at 1316 keV can mimic a lifetime effect on the 1359-keV peak by shifting its centroid or adding a tail. Because of their position and a better resolution, the GRETINA-like detectors are inevitably more sensitive to both these effects. Without considering the 1316-keV transition, the half-lives measured with MINIBALL are as large as 7.6 ps (0.6 ps increase) and 22.4 ps for

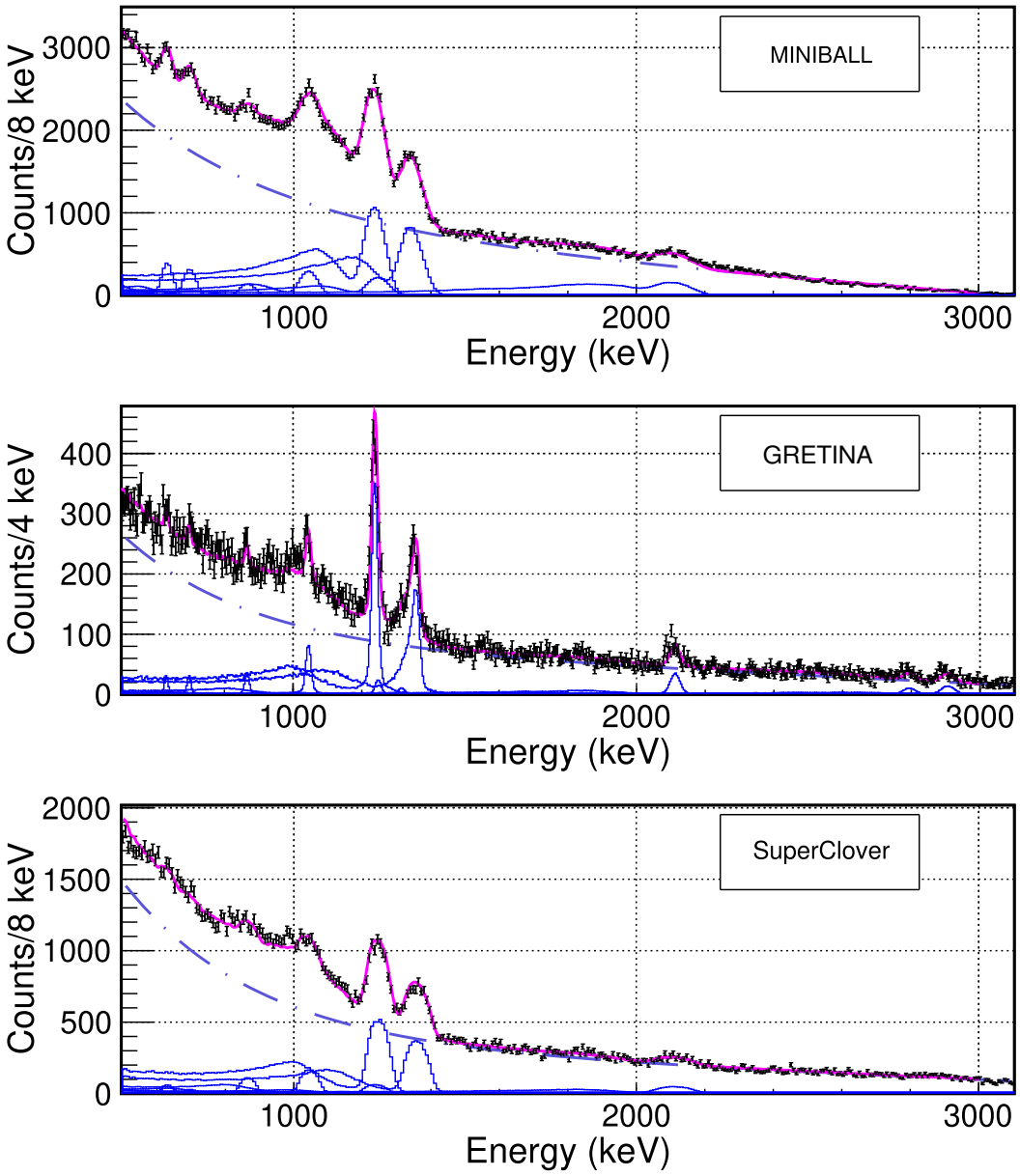

Figure 5.6 – Fit of the Doppler-corrected γ-ray spectra in the range [500-3000] keV. The lifetime simulated on the 1359 keV state is the one determined through the χ^2 minimisation procedure on the corresponding detector group. The pink line is the total fit function, the blue dashed-dotted line indicate the background contribution, and the blue histograms are the contributions of each transition to the total.

the GRETINA quad (0.9 ps increase). The analysis of GRETINA detectors data are more affected by the absence of a peak at 1316 keV, thus leading to an even stronger disagreement between the detector groups.

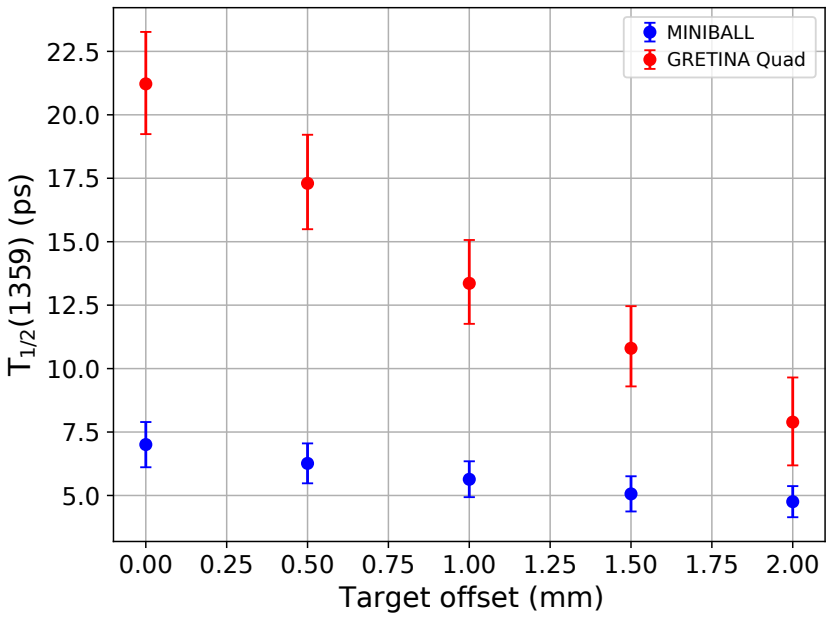

Figure 5.7 – Half-life of the 1359-keV state in ^{83}Ge obtained through the analysis of the data from the MINIBALL detectors (in blue) and the GRETINA detectors (in red), plotted against a shift of the target along the Z-axis.

Conclusion on the disagreements

In this PhD work, we did not succeed in pointing exactly to the source of the half-life mismatch between the detector groups. However, among our investigations of systematic errors, the positioning of the detectors was identified as the most probable cause. When available, the comparison with other experiments performed during the campaign should help us find the source of the disagreement.

Systematic effects such as position offsets tend to shift the reconstructed peak energy, and indirectly lead to a systematic offset of the lifetime extracted from the fit procedure assuming the true transition energy as input. A way to investigate this issue would be to let the simulated energy free, and fit the energy along with the half-life. This requires a lot more simulations (one for each ($T_{1/2}$, E_γ) pair) and would result in a χ^2 surface with a 2D-minimum corresponding to the optimal parameters. If the optimal energy determined in this approach for a given group of detectors is significantly away from the tabulated one, this could provide an additional clue that a systematic error exists for this group.

In figure 5.8, the preliminary results of such a study are presented for the nominal positions (top) and assuming a shift of +1 mm of the target (bottom). The χ^2 surfaces for the MINIBALL and GRETINA detectors show a minimum that is determined by a series of fits. The errors are defined by the portion of the surface containing the values below $\chi^2_{min} + 2.4$ (delimited by the red lines in the figure) which corresponds to a 1-σ error definition for the simultaneous minimisation of two parameters. For the MINIBALL

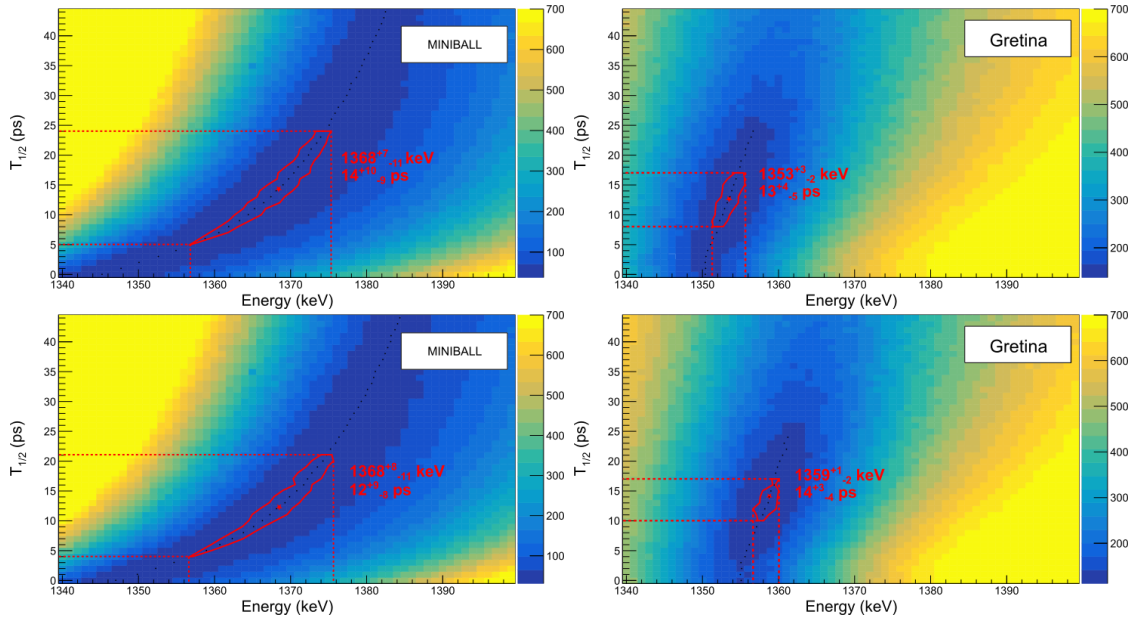

(a) MINIBALL **(b)** GRETINA

Figure 5.8 – Two-dimensional histogram on which each bin represents the χ^2 obtained through the fit of the 1359-keV peak using the corresponding energy and half-life in the simulation. (a) is from MINIBALL detectors data, (b) is from the GRETINA Quad data. Top shows the results with the nominal positions, bottom shows the result assuming a shift of $+1$ mm of the target along the beam axis.

detectors, a rather flat χ^2 valley is obtained demonstrating the direct correlation between a lifetime effect and an energy shift of the transition without distortion of the peak shape (as illustrated previously with simulations in section 2.3.2). As a consequence, the statistical errors determined with this 2D-profile increases significantly compared to the 1-dimensional case for which the transition energy was fixed. On the opposite for the GRETINA detectors, the better energy resolution and the peak shape sensitivity to the lifetime of the state leads to a better defined minimum region and error contours. The energies and half-lives of the minima for MINIBALL and GRETINA detectors are listed in table 5.2. Looking at the results, clearly the resulting half-lives determined using the two detector groups are brought closer using this 2-dimensional method, showing now a good agreement.

We find that the optimal energy for the MINIBALL group is 1368^{+7}_{-11} keV. While it is 9 keV away from the tabulated energy (1359 keV) for this transition, the values are still 1-σ compatible. The cause of this difference could be statistic (as implied here) but could also come from a systematic error, and remains to be clarified. On the other hand, the optimal energy of 1353^{+3}_{-2} keV found using GRETINA detectors is incompatible with the literature energy of 1359 keV for this transition. The tests presented in the table show that this incompatibility can be solved by the assumption of a $+1$ mm shift of the target without significantly affecting half-lives, or results using the MINIBALL detectors. Considering the

	Nominal positions		+1 mm shift	
	Energy (keV)	Half-life (ps)	Energy (keV)	Half-life (ps)
MINIBALL	1368^{+7}_{-11}	14^{+10}_{-9}	1368^{+8}_{-11}	12^{+9}_{-8}
GRETINA	1353^{+3}_{-2}	13^{+4}_{-5}	1359^{+1}_{-2}	14^{+3}_{-4}

Table 5.2 – Energy and half-life at the position of the minimum of the χ^2 surfaces in figure 5.8 for MINIBALL and GRETINA detectors using nominal positions and assuming a +1 mm shift.

benefits of this +1 mm target shift observed on the benchmark case, the values using this assumption will be preferred here.

Using the results from the minimisations of the half-life for both group of detectors with the +1 mm assumption on the target, we are able to calculated a variance-weighted mean value by considering symmetric errors (largest side): $T_{1/2} = 14(4)$ ps (all numbers rounded to unity).

While this value and the errorbars associated are susceptible to change with the advance of the analysis, we choose here to discuss it for the comparison with theoretical models in the next chapter.

5.2.3 1238/1248 keV doublet peak

As mentioned previously, the 1238- and 1248-keV states were expected to originate from core-excited configurations (^{82}Ge(2^+), and a single neutron in the $s_{1/2}$ or $d_{5/2}$ orbital) and by consequence they should be weakly populated by our direct reaction mechanism. The 1238/1248-keV doublet peak being the most intense in our spectra, we propose a list of tests in order to investigate the relative intensity of the 1238-keV and the 1248-keV contributions.

Fit scenario		χ^2/N	
1238 keV	1248 keV	MINIBALL	GRETINA
$T_{1/2} = 0$	$T_{1/2} = 0$	1.6	2.7
$T_{1/2} = 0$	Removed	1.8	2.7
Removed	$T_{1/2} = 0$	10.7	12.7
Removed	$T_{1/2} = 4$ ps (MB) $T_{1/2} = 22$ ps (Gr)	1.8	6.1
$T_{1/2} = 0$	$T_{1/2} = 4$ ps (MB) $T_{1/2} = 22$ ps (Gr)	1.6	2.2

Table 5.3 – χ^2 per number of degrees of freedom obtained from a fit in the range [1100-1350] keV for three different scenarios.

In table 5.3 we list the χ^2 per number of degrees of freedom obtained using four different assumptions when fitting the 1238/1248-keV peak:

— Both peaks are included in the fit, assuming no lifetime effect for both of them.
— Only the 1238-keV peak is included, assuming no lifetime effect.
— Only the 1248-keV peak is included, assuming no lifetime effect.
— Only the 1248-keV peak is included, and a half-life minimisation is performed. The shown χ^2/N corresponds to the value at its minimum.
— The 1248-keV peak is included with the half-life minimised in the previous case, and the 1238-keV peak is included without a lifetime effect. The shown χ^2/N corresponds to its value at the minimum.

Since the centroid of the peak in all detectors is at an energy slightly higher than the response function of the 1238-keV peaks, it is pointless to look for a lifetime effect for this transition.

We observe that removing the 1248-keV peak does not significantly affect the quality of the fit. On the other hand, the second test clearly rejects the hypothesis of populating only the 1248-keV state with a negligibly short lifetime. A possibility that still remains is that we populate mainly the 1248-keV state, but its position is affected by a lifetime effect. This is the point of the last two tests in table 5.3. The χ^2/N results for the fits seem to indicate that this doublet peak has either mostly the 1238-keV transition contribution (first two tests), or that both peaks are present with a relatively similar intensity, but the 1248-keV has a significant lifetime.

The nature of the states contributing to this doublet will be discussed in comparison with theoretical models and previous results in the next chapter.

5.3 Exclusive cross sections

This section aims at the determination of the exclusive cross sections leading to each state considered.

Using the amplitude factor of each transition minimised in the spectrum fit (figure 5.6) and the number of events simulated for each transition (10^7), we determine the number of events detected in each peak. For states that are not fed through a cascade this corresponds to the measured population of each state N_f. In the case of two states (1238 keV and 1359 keV) we need to account for indirect feeding, hence we subtract the events simulated for the higher excitation-energy states from the events simulated for the lower excitation-energy state:

$$\begin{cases} N_f(1238) = N_{fit}(1238) - N_{fit}(1316) \\ N_f(1359) = N_{fit}(1359) - N_{fit}(631) \end{cases} \tag{5.1}$$

The obtained numbers of events and percentages of the total are shown in the first two columns of table 5.4. While performing the tests presented in section 5.2.3, we observed that the relative population of the states at 1238 keV and 1248 keV depends rather strongly

State	N_f		Relative intensity (%)		σ_{exp} (mb)	
	MB	GRETINA	MB	GRETINA	MB	GRETINA
1045 keV	149376	185019	7.5	7	**5.0(4)**	6.2(7)
1238/1248 keV	835702	9910278	52	38	**28(4)**	33(3)
1359 keV	518348	825941	26	32	**17(1)**	28(1)
1990 keV	93886	39631	5	1.5	**3.1(3)**	1.3(5)
2113 keV	247042	198803	12	7.6	8.3(3)	**6.7(7)**
2555 keV	7486	32536	<1	1.25	<1	**1.1(6)**
2795 keV	0	92959	0	3.5	0	**3.1(7)**
2907 keV	0	136303	0	5.2	0	**4.6(8)**

Table 5.4 – For MINIBALL and GRETINA quad, and for each state considered in the spectrum fitting: (i) Number of events detected. (ii) The relative intensity. (iii) The exclusive cross section. The strengths for both 1238-keV and 1248-keV states are summed together (see text for details).

on the assumptions made on the nature of the observed peak. However the sum of both peaks is relatively independent of the hypothesis. In order to show results that do not depend too much on early assumptions we decide to show here the summed cross section to the doublet 1238/1248-keV peak.

The exclusive cross section is determined using the following formula:

$$\sigma_{exp} = \frac{N_f}{N_i N_c T}\,, \tag{5.2}$$

where:

— N_f is defined above.

— N_i is the number of ^{84}Ge nuclei impinging on the target. It is evaluated using the sum of all downscaled triggers (F7DS, see section 2.4) for all the runs with only a selection on the BigRIPS PID. We obtain here $N_i = 402\,988\,610$ particles.

— N_c is the surface density of reaction centres in a thickness $e = 6$ mm of solid ^{9}Be, calculated using the molar mass $M = 9.012$ g/mol, the volumic mass $\rho = 1.848$ g/cm^2, and the Avogadro number N_A: $N_c = \rho e N_A / M = 7.409225 \times 10^{22}$ particles per cm^2.

— T is a factor resulting from transmission losses (acceptance cuts due to settings in ZDS), efficiency losses (from detectors used to track/identify the product) and reaction losses (other reactions of the beam or fragments in the target, or with the beam line material). In this thesis we consider $T = 1$ and leave its determination for the future. The transmission loss shall be determined by comparing positions measured in BigRIPS with and without conditions on the outgoing nucleus. Because of this, the cross sections presented here are preliminary, and based on past experience we expect the cross sections for **all** states to be up to 20-30% larger when all effects are considered. Since this is not state dependent, it will not affect our discussion of the

relative spectroscopic factors in the next chapter.

The contributions to the uncertainty of the cross section are added in quadrature:

$$\left(\frac{\delta_\sigma}{\sigma}\right)^2 = \left(\frac{\delta_{N_f}}{N_f}\right)^2 + \left(\frac{\delta_{N_i}}{N_i}\right)^2 + \left(\frac{\delta_{N_c}}{N_c}\right)^2 , \tag{5.3}$$

where the uncertainty on N_f results from the error on the amplitude scaling parameter from the fit, and the uncertainty of N_i is calculated using $\delta_{N_i} = \sqrt{N_i}$. The uncertainty on N_c is considered to come overwhelmingly from the uncertainty on the target thickness δ_e. This uncertainty is unknown and considered to be of 1% in these calculations.

While the relative uncertainty is very high for sparsely populated states (up to 50% for the 2555-keV state in GRETINA type detectors) it remains around 10% for the three main states (5% for the 1359-keV state).

In addition to those statistical uncertainties, we can also discuss some sources of systematic uncertainties:

— Uncertainty on the lifetime: in section 2.3.2 we showed that a larger lifetime results in a response function that is more spread out in energy. Therefore an error on the lifetime would impact the cross section value.

— γ-ray efficiency: figure 3.18 showed a reasonable agreement between the simulated and measured efficiencies, however some minor differences remain and impact our cross-section measurements. It is rather nontrivial to evaluate the Doppler-corrected (centre-of-mass frame) efficiency errors from the lab frame efficiency discrepancies that we have between data and simulation. By looking at the extrema of the differences between the simulated and measured efficiencies, we can express its maximum impact on the cross sections to be [−8%, +1%] for the MINIBALL detectors and [−7%, +7%] for the GRETINA-like detectors (the reader should keep in mind that this is necessarily an overestimation).

In order to limit the impact of the lifetime uncertainty on the discussed cross sections, we use values measured using MINIBALL detectors in the next chapter for states below 2 MeV. For states above 2 MeV, the superior resolution of GRETINA allows to distinguish them significantly better from the background. Hence we decide to use the GRETINA detectors for them. The values that will be discussed in the next chapter are written in bold in table 5.4.

Chapter 6

Discussion

In this chapter we will interpret the experimental results for ^{83}Ge obtained in the previous chapter. They will be compared to calculations from two theoretical models: a phenomenological core-particle coupling model, and microscopic large-scale shell-model calculations. From the measured exclusive knockout cross sections and lifetime constraints for each state we shall clearly identify the 2p-1h intruder states, and the significant differences with theoretical models will give directions for new developments (experimental or theoretical).

6.1 General discussion of the ^{83}Ge results

6.1.1 Cross sections and spectroscopic factors

The measured cross sections presented in table 5.4 already provide information about the states favoured by the reaction mechanism, thus showing qualitatively which states are likely to have a non-negligible single-hole (1h) or 2 particles - 1 hole (2p-1h) component in their wave functions.

Theoretically, the single-particle (hole) nature of a state in a nucleus is quantified by a quantity called the "spectroscopic factor" (S). It is defined as the overlap between the wave function of a A-nucleons nucleus in an initial state $\left|\psi_0^A\right\rangle$, to which a nucleon is added (removed) *via* the creation (annihilation) operator $a^\dagger$ (a), and the wave function of a $A+1$ ($A-1$) nucleus in the considered particle (hole) state [78]:

$$S = \int \left| \left\langle \psi_{p(h)}^{A\pm1} \middle| a^{(\dagger)}(\vec{\mathbf{r}}) \middle| \psi_0^A \right\rangle \right|^2 d\vec{\mathbf{r}} \tag{6.1}$$

In practice, the spectroscopic factor is not strictly speaking an observable quantity and is commonly extracted from the exclusive nucleon removal cross section leading to a given final state. This is done under the hypothesis that the cross section for such a direct

process can be decomposed simply as $\sigma_{exp} = \sigma_{sp} \times C^2S$, where the first term σ_{sp} describes the dynamical part of the cross section (energy dependence, densities of the projectile, target, etc) and the second term C^2S describes the structural overlap between the initial and final states (experimental spectroscopic factor, C being an isospin coupling coefficient). When starting from a 0^+ ground state (even-even nuclei for the beam), only a single orbital nlj can contribute to the nucleon removal to a given state with angular momentum J. In this particular case the experimental spectroscopic factor is deduced from the ratio [79]:

$$C^2S = \frac{\sigma_{exp}}{\sigma_{th}^{sp}}, \tag{6.2}$$

where

— σ_{exp} is the measured cross section to the considered state of the reaction residue (calculated using equation 5.2).

— σ_{th}^{sp} is the theoretical cross section for a single-particle state calculated for the knock-out reaction (removal of a nlj nucleon) within the eikonal approximation.

The evaluation of this spectroscopic factor allows us to discuss a quantity that depends only on the internal structure of the nucleus, thus allowing a comparison with microscopic theories. It is worth noting that the extracted C^2S depends on the reaction model and therefore it is not fully an experimental quantity. In our experimental conditions, the typical approximations made in knockout reaction models (high energy) are fulfilled and therefore the comparison with the theoretical cross section should hold.

State	J^π	σ_{exp} (mb)		nlj	σ_{sp} (mb)	C^2S_{exp}
		MB	GRETINA			
1045 keV	$(3/2^+)$	**5.0(4)**	6.2(7)	–	–	–
1238/1248 keV	$(5/2^+,7/2^+,9/2^+)$	**28(4)**	33(3)	$1g_{9/2}$	7.7	3.6(5)
1359 keV	$(9/2^+)$	**17(1)**	28(1)	$1g_{9/2}$	7.6	2.3(1)
1990 keV	$(11/2^+,13/2^+)$	**3.1(3)**	1.3(5)	–	–	–
2113 keV	$(9/2^+)$	8.3(3)	**6.7(7)**	$1g_{9/2}$	7.3	0.9(1)
2555 keV	–	<1	**1.1(6)**	–	–	–
2795 keV	$(9/2^+)$	0	**3.1(7)**	$1g_{9/2}$	6.9	0.5(1)
2907 keV	$(9/2^+)$	0	**4.6(8)**	$1g_{9/2}$	6.9	0.7(1)

Table 6.1 – Exclusive cross sections σ_{exp} for each state in ^{83}Ge populated *via* the knockout of a neutron from ^{84}Ge. J^π is the tentative spin-parity of the state, nlj are the quantum numbers of the orbital from which we make the hypothesis that the neutron has been knocked out, σ_{sp} is the theoretical single particle cross section associated with the said hypothesis, and C^2S_{exp} is the spectroscopic factor obtained between the states concerned though the formula 6.2. For the unresolved 1238/1248-keV doublet, the C^2S_{exp} simply represents an upper limit for an single hypothesis of an angular momentum of the removed nucleon (see text for more details).

The determined spectroscopic factors are summarised in table 6.1. Both cross sections measured with MINIBALL and GRETINA Quad are listed. As mentioned in the previous chapter, for the spectroscopic factor calculation we use the ones measured with MINIBALL below 2 MeV and with GRETINA above 2 MeV (figures in bold). Starting with the clearest observations [1]:

— The state at 1359-keV, proposed as a $(9/2^+)$ intruder by C. Delafosse *et al.* [3] is strongly populated. With a cross section of 17(1) mb, it is the second of the most strongly populated states (behind the 1238/1248-keV doublet discussed below). Our $T_{1/2} = 14(4)$ ps value is compatible with, but close to the lower limit of the $\tau = 74^{+73}_{-67}$ ps lifetime measured by Delafosse *et al.*

— Three states with an excitation energy above 2 MeV have non-negligible inclusive cross sections. Hence they are identified as candidates for having contributions to the wave function coming from a hole in the $1g_{9/2}$. We tentatively assign them a spin parity of $(9/2^+)$. In this hypothesis those three states together would carry a spectroscopic factor of 2.1(3), which is almost as that of much as the 1359-keV state.

— The 1238/1248-keV doublet is the most populated. It is considerably more surprising since precedent studies (β-decay and plunger measurements [3]) are rather indicating states resulting from the coupling multiplet $[^{82}\mathrm{Ge}(2^+)\times\nu(\mathrm{d}_{5/2})^{+1}]$. Given the previously proposed spin parities being $(5/2^+, 7/2^+)$ and $(7/2^+, 9/2^+)$ respectively for the states at 1238 keV and 1248 keV, we cannot leave out the possibility that one of those two states carries a significant fraction of the spectroscopic strength coming from the $1g_{9/2}$, and that the other one contains a different contribution (such as $2d_{5/2}$ strength). One of the fit results for this doublet, in which the 1248-keV state has a half-life of about 4(1) ps (MINIBALL detectors) and dominates the total amplitude of the observed peak (see section 5.2.3), would be compatible with this hypothesis and the spin-parity $(7/2^+, 9/2^+)$ proposed by C. Delafosse *et al.*, and close (but not incompatible) with the upper limit obtained *via* their plunger measurement ($T_{1/2} < 3.5$ ps). At present, we are not able to firmly conclude experimentally on the relative contribution from each state, and the 3.6 spectroscopic factor presented in table 6.1 only represents an upper limit of the spectroscopic strength that this doublet can contain if we interpret it solely as a pure $g_{9/2}$ neutron knockout contribution.

6.2 Theoretical framework

The simultaneous calculation of the natural and intruder states for ^{83}Ge and the neighbouring $N = 51$ isotopes remains a theoretical challenge since it requires to allow multiple

1. unaffected by the differences observed between the detector groups

excitations of nucleons above the $N = 50$ and $Z = 28$ core while including all the necessary valence orbitals (sdg for neutrons and pf for protons). Only models having such extended valence spaces are able to reproduce reasonably the observations made during the last few years for example in ^{79}Zn and ^{78}Ni (see section 1.2.3). As of yet, very few shell-model calculations have been able to achieve this goal, and only for few nuclei: the LSSM calculation with the PFSDG-U interaction [18], and the Monte-Carlo approach (MCSM) with variations of the A3DA interaction [80]. We have collaborated with F. Nowacki to apply his calculations with the PFSDG-U interaction to ^{83}Ge, so that we are able to compare it with our results. Some details on this calculation will be given in the following section.

Given the high computing power required to perform shell model calculations with this extended valence space, simpler models of the core-particle (CP) coupling developed in [30] are valuable in order to identify the type of excitation for the expected states, the configuration mixing between single particle and core excitations, and the sensitivity of the energy of the states to some of the parameters. This approach has been driven in the $N = 50$ region for several years by D. Verney , notably in the PhD work of C. Delafosse [3]. Details on this calculations are available in the references [3, 30, 81] and only an overview will be given here.

6.2.1 Two Cores coupling model from the Core - Particle approach

The states resulting from this model result from the coupling of the even-even core at $N = 50$ with a single neutron, and from the even-even core at $N = 52$ with a single neutron hole: $(^{82}_{32}\mathrm{Ge}_{50} \otimes \nu) \otimes (^{84}_{32}\mathrm{Ge}_{52} \otimes \nu^{-1})$. In total the Hamiltonian writes as following [3]:

$$H = H_c + H_{sp} + H_{sh} + H_{cp} + H_{ch} + H_{cph} + V_{pp} + V_{ph}\,, \tag{6.3}$$

where:

- H_c describes the excitations of the even-even core (typically 2^+, 4^+ etc...). The eigenvalues are fixed at first to the experimental excitation energies.
- H_{sp} and H_{sh} describe the single-particle and single-hole energies in the mean-field potential created by the core.
- H_{cp}, H_{ch}, H_{cph} describe the interaction between the $N = 50$ core and the single-particle, single-hole, and particle-hole, respectively.
- V_{pp} and V_{ph} are the residual particle-particle and particle-hole interactions.

The single-particle energies are adjusted using the simpler Core-Particle approach. A more detailed description of this model can be found in references [8] and [81].

The unperturbed 2 particle - 1 hole energies are calculated using results of mass mea-

surements:

$$\epsilon_{2p-1h} = \epsilon(2d_{5/2}) - \epsilon(1g_{9/2}) + \Delta E_{pairing}\,, \tag{6.4}$$

where $\Delta E_{pairing} = 2S_n(Z, N = 51) - S_{2n}(Z, N = 52)$ is the gain in energy from creating a pair at $N = 51$.

The anharmonicity (static quadrupole moment of the core), that also intervenes in the interaction between the core and the particle/hole, is fitted by comparing predictions and data for the $2^+ \otimes \nu d_{5/2}$ in ^{89}Sr.

The coupling parameters between the core and the particle, core and the hole, and core and the particle-hole are fitted to the experimental values of the 2_1^+ and 3_1^- energies in ^{82}Ge (or in ^{84}Se if unknown).

More details on the full solving of the Schrödinger equation can be found in [3].

6.2.2 Shell model and PFSDG-U interaction

The shell-model calculations presented in this chapter are performed considering an inert core of ^{60}Ca leaving the full *sdg* neutron orbitals (for 11 particles) and *pf* proton orbitals (for 12 particles) as the valence space.

The PFSDG-U interaction is constructed by adjusting the effective single-particle energies (ESPE) to reproduce several phenomenological constraints such as: $B(E2; 2^+ \rightarrow 0^+)$ for the $Z = 28$ shell gap, binding energies and $N = 50$ energy gap measurements in the region for neutron ESPEs, or the energy systematics of several states ($9/2^+$, $5/2^+$, $1/2^+$) along N=49.

In our case, the configurations are restricted to 7p-7h maximum. In addition, only the first two states for each J^π have fully converged. More details on the parameters on this interaction and the solving of the Hartree-Fock equations can be found in [18].

6.3 Comparison with the models

At first, we compare in figure 6.1 the level scheme presenting the states populated in our experiment with the level schemes obtained through the two aforementioned theoretical models. In figure 6.2 we present as well the distribution of spectroscopic factors as a function of excitation energy (experimental first and for both theoretical calculations).

6.3.1 Ground and first excited states

The ground state and the first excited state are predicted to be of spin-parity $5/2^+$ and $1/2^+$, respectively, by both theoretical models. While those two states are predicted by

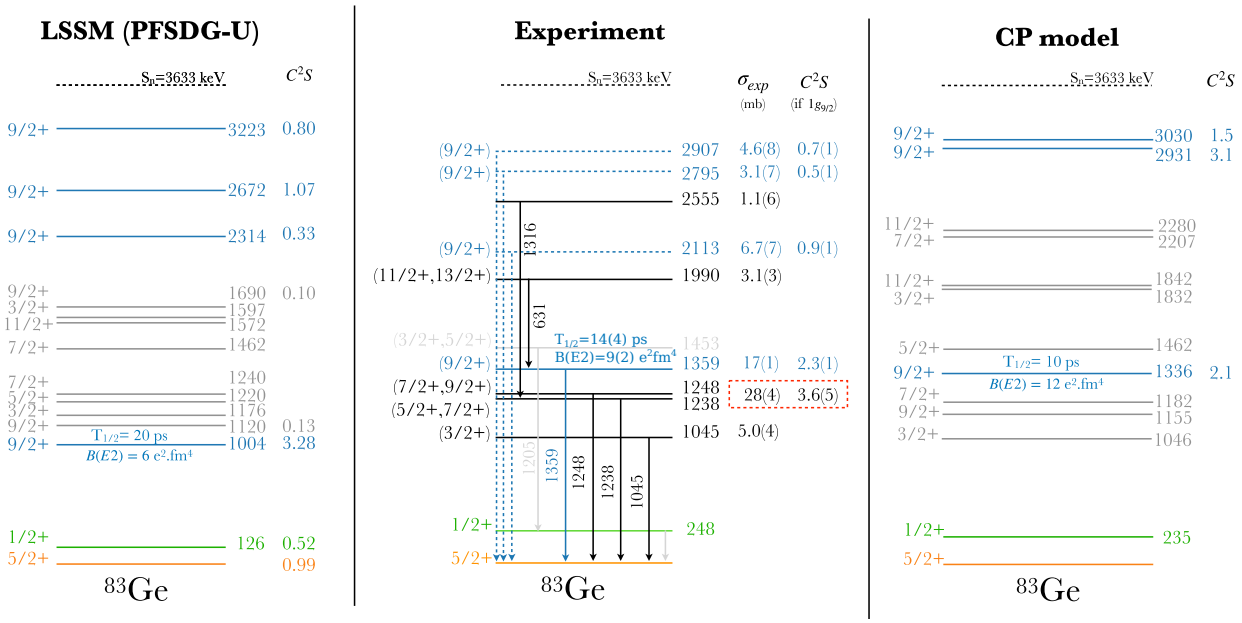

Figure 6.1 – Level schemes obtained within a Shell-Model calculation using the PFSDG-U interaction (left), within the Core-Particle coupling model (right), compared with the experimental level scheme (middle). In orange the $5/2^+$ ground state, and in green the first excited $1/2^+$ (not observed in the present data for reasons explained in the text). In blue we present the intruder candidates and with dashed lines the unconfirmed ones.

both calculations to be mainly of a single-particle nature, they are not completely pure and show non-negligible mixing with states resulting from the coupling with core excitations. Given its low energy and single-particle nature, the $1/2^+$ state (in green in figure 6.1) was anticipated to have a long lifetime ($\tau \approx 4$ ns) and consequently decays away from our setup, and we indeed did not observe associated gamma-ray transitions.

A way to study those states would be to measure the inclusive cross sections thus giving access (by subtraction) to the summed cross section for the ground and first excited states.

6.3.2 1359-keV state

The calculations do not give the half-life as a direct output, but instead predict the $B(E2)$ transition probability. The general relation between a $B(EL)$ transition probability and the half life is given by:

$$\frac{\ln(2)}{T_{1/2}} = 5.498 \times 10^{22} \frac{L+1}{L\left[(2L+1)!!\right]^2} \left(\frac{E_\gamma}{197.33}\right)^{2L+1} B(EL)\,, \tag{6.5}$$

where $T_{1/2}$ is in seconds, E_γ in MeV and $B(E2)$ in e^2fm^4. For $L = 2$ this reduces to:

$$\frac{\ln(2)}{T_{1/2}} = 1.225 \times 10^9 \times E_\gamma^5 \times B(E2)\,. \tag{6.6}$$

The theoretical models predict energies of 1004 keV (LSSM) and 1336 keV (CP) and $B(E2)$ of 6 e^2fm^4 and 12 e^2fm^4, respectively, leading to half-lives of 92 ps and 11 ps, respectively. However, the energy dependency is strong (E_γ^5) and we can adapt the predicted half-life to the experimental $E_\gamma = 1359$ keV, while still using the $B(E2)$ from the theory. This results in a predicted half-life of 20 ps for LSSM and 10 ps for CP. Those figures are summarised in table 6.2.

	E(keV)	J^π	$T_{1/2}$ (ps)	B(E2,↓) (e^2fm^4)	B(E2,↓) (W.u)
Exp.	1359	$(9/2_1^+)$	14(4)	9(2)	0.4(1)
LSSM	1004	$9/2_1^+$	92	6	0.27
	scaled to 1359	$9/2_1^+$	20	6	0.27
CP	1336	$9/2_1^+$	11	12	0.54
	scaled to 1359	$9/2_1^+$	10	12	0.54

Table 6.2 – Comparison between experiment and theory for the half-life of the $(9/2_1^+)$ state and associated transition probabilities. The rows labelled "scaled to 1359" correspond to the $T_{1/2}$ obtained by conserving the calculated transition probability but adapting the transition energy to the experimental value.

In this work, the first $9/2^+$ state was observed at 1359 keV with a half-life of 14(4) ps. While both models predict a longer half-life, they are reasonably close to the measured value and stay in the same order of magnitude. The experimental $B(E2)$ value for the transition is 0.4(1) Weisskopf units which is rather close to a single-particle excitation.

As seen in figure 6.2, the state at 1359 keV has a relatively large spectroscopic factor and can be identified with predicted states at 1004 keV (LSSM) and 1336 keV (CP), both having a $g_{9/2}$ strength largely dominant in the energy range below 2 MeV.

The LSSM calculation also provides the average occupation of the orbitals for each predicted state. Those occupations are presented in table 6.3 for the ground state of ^{84}Ge and the excited states of ^{83}Ge. For the first $9/2_1^+$ state predicted at 1004 keV, identified with our 1359 keV state, it appears clearly that the occupation of the $1g_{9/2}$ orbital decreases by one nucleon with respect to ^{84}Ge (9.41 $\longrightarrow$ 8.44) while all the other occupations remain the same. This indicates that the predicted state is a 2p-1h configuration, strongly supporting the hypothesis for the intruder nature of the 1359 keV state.

			Neutrons					Protons			
Nucleus	E(keV)	J^π	$1g_{9/2}$	$2d_{5/2}$	$3s_{1/2}$	$1g_{7/2}$	$2d_{3/2}$	$1f_{7/2}$	$2p_{3/2}$	$1f_{5/2}$	$2p_{1/2}$
^{84}Ge	0	0^+	9.41	1.55	0.62	0.28	0.14	7.45	1.68	2.44	0.43
^{83}Ge	126	$1/2^+$	9.33	**0.68**	0.69	0.21	0.08	7.55	1.58	2.52	0.35
	1004	$9/2^+$	**8.44**	1.45	0.67	0.26	0.18	7.48	1.73	2.30	0.50
	1120	$9/2^+$	9.25	1.28	**0.19**	0.21	0.07	7.60	1.34	2.66	0.40
	1176	$3/2^+$	9.27	**0.86**	0.37	0.24	0.26	7.58	1.45	2.55	0.42
	1219	$5/2^+$	9.16	**1.06**	0.50	0.21	0.07	7.58	1.52	2.56	0.35
	1240	$7/2^+$	9.17	1.35	**0.13**	0.28	0.07	7.54	1.43	2.67	0.36
	1462	$7/2^+$	9.27	**0.63**	**0.09**	**0.90**	0.10	7.56	1.48	2.57	0.38

Table 6.3 – Average orbital occupations for the ^{84}Ge ground state and low energy states in ^{83}Ge obtained in the LSSM calculations using the PFSDG-U interaction. Figures in bold indicate a change of occupation of more than 0.3 nucleons with respect to the ground state of ^{84}Ge.

6.3.3 States in the $[^{82}\mathrm{Ge}(2^+)\times\nu(\mathrm{d}_{5/2})^{+1}]$ multiplet

The states in the $[^{82}\mathrm{Ge}(2^+)\times\nu(\mathrm{d}_{5/2})^{+1}]$ multiplet predicted by the CP and LSSM models can be seen in figure 6.1. A $3/2^+$ state is predicted at 1046 keV, matching closely the observed state at 1045 keV. In LSSM, an equivalent $3/2^+$ state is predicted at 1176 keV with occupations corresponding to a full $1g_{9/2}$ orbital and a single neutron in the $2d_{5/2}$ orbital.

Two $7/2^+$ and $9/2^+$ states are predicted at 1182 keV and 1155 keV by CP, and of 1240 keV and 1120 keV by LSSM. Previous spin-parity assignments made by Delafosse *et al.* lead to identifying them with our measured states at 1238 keV and 1248 keV. However, as shown in figure 6.2, the spectroscopic strength of those states predicted by LSSM calculations is a lot lower than what we measure, leading to an important disagreement. In order to solve this conflict, several hypotheses can be made:

— The peak at 1238/1248 keV carries an important unpredicted $g_{9/2}$ strength.

— The ^{84}Ge nucleus already presents a significant amount of particle-hole excitations.

— Other unresolved transitions are present in the observed peak and are not taken into account, thus leading to the division of the total strength among more states.

A clear explanation why such important spectroscopic factors are measured for those states remains unsolved and will require further developments.

6.3.4 High-lying $9/2^+$ strength

Both models predict $9/2^+$ states at high energies (above 2 MeV). The LSSM calculation have not converged for the energy of those states, thus we propose to use here only the

total spectroscopic strength for comparison. For our three high-energy states the total spectroscopic factor is of 2.1(3). The CP model predicts two high energy $9/2^+$ states at 2931 keV and 3030 keV with a total spectroscopic strength of 4.6, which is about twice as much than we observed. As mentioned before, due to the correction of transmission loss to be performed in the future, we expect an increase of spectroscopic factors of about 20%, bringing the measured value closer to the CP predictions, but still incompatible.

On the other hand, the LSSM calculation predicts a $g_{9/2}$ strength above 2 MeV of 2.2, which compares very well with the experimental value of 2.1(3) presented here (see the C^2S values in figure 6.1, and the strength distribution against energy in figure 6.2). A more precise experimental analysis for those states will be performed in the future and shall lead to constraints on the energies of the transitions observed and the state lifetimes.

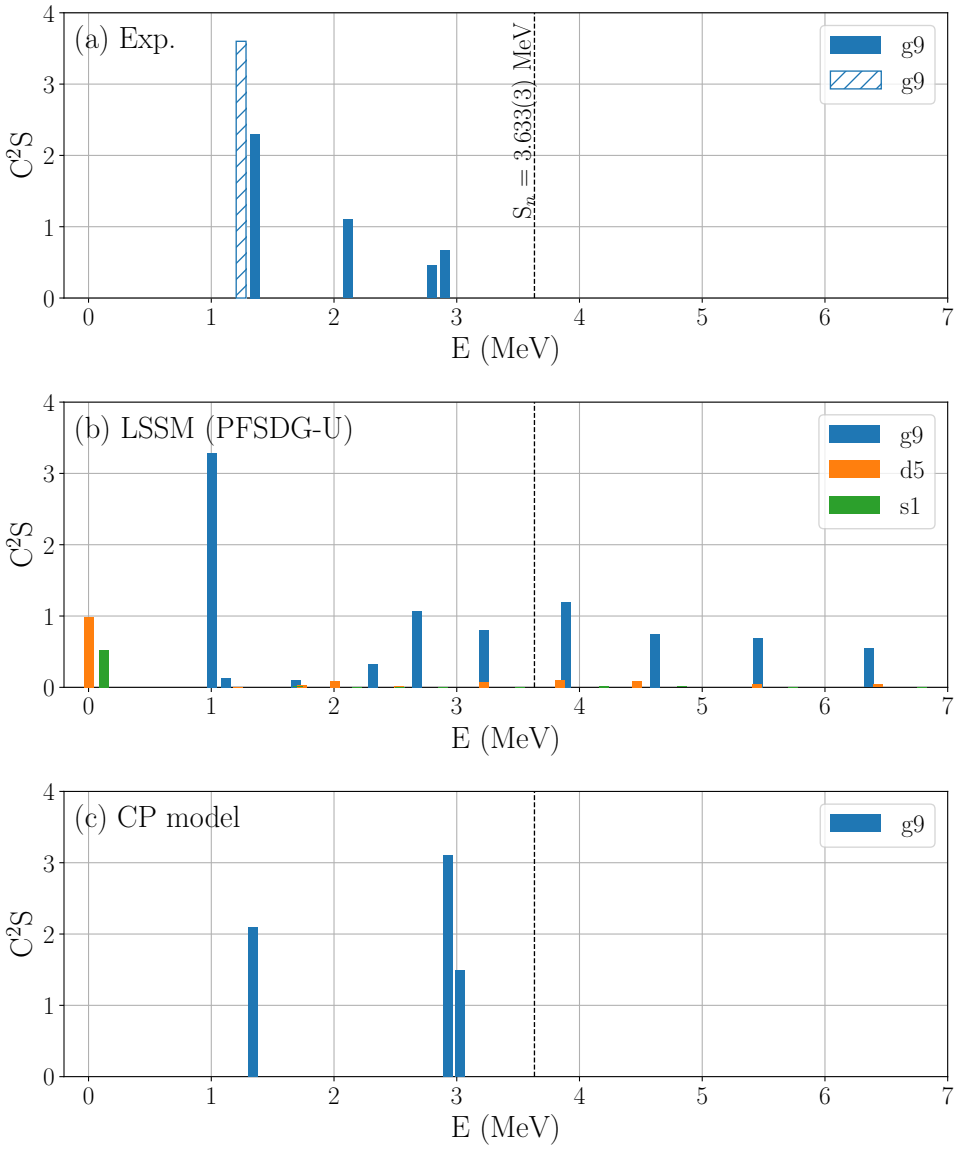

Figure 6.2 – Spectroscopic factors (a) obtained experimentally, (b) calculated *via* the LSSM model, (c) calculated *via* the CP model. We present in blue the strength from the $g_{9/2}$ orbital, in red from the $d_{5/2}$, and in green from the $s_{1/2}$. The shaded area in (a) corresponds to the total strength corresponding to the peak at 1240 keV under the hypothesis described in the text.

Chapter 7

Conclusion and perspectives

In this work we have performed the in-flight spectroscopy of ^{83}Ge targeted at characterising the 2p-1h intruder states dominated by a hole configuration in the $g_{9/2}$ orbital. Those configurations were probed at RIBF-RIKEN in 2020 using a neutron knockout reaction from the $N = 52$ nucleus ^{84}Ge. The beam identification and separation was done using the BigRIPS and ZeroDegree spectrometers while the γ rays were measured by the multidetector array HiCARI.

In particular, a state at 1359 keV, previously identified as a good intruder candidate, was extensively studied. For this state, a preliminary half-life of 14(4) ps was determined, using adjustments of the response functions deduced from GEANT4 Monte-Carlo simulations, and an experimental exclusive cross-section of 17(1) mb was measured leading to a spectroscopic factor of 2.3(1). This relatively long half-life (with respect to the other states) and high spectroscopic factor show a reasonably good agreement with theoretical predictions of 2p-1h intruder states predicted at 1336 keV and 1004 keV, respectively, by a phenomenological Core-Particle coupling model and Shell-Model calculations using the PFSDG-U interaction. This study provided the first measurements of the half-life and spectroscopic factor for this state strongly supporting its 2p-1h intruder nature. If the analysis of the parallel momentum distribution for the 1359-keV transition de-exciting this state shows that it is most compatible with a $L = 4$ neutron knockout, an additional argument will be obtained to support the 2p-1h intruder nature with a neutron knocked out from the $1g_{9/2}$ orbital.

We detected three new high-energy states above 2 MeV carrying a total spectroscopic factor of 2.1(3). This is in line with the fact that both models predict a $g_{9/2}$ intruder spectroscopic strength at high energy above 2 MeV. While the CP model predicts more strength in fewer states than we measured, a very good agreement is found with the Shell-Model calculations predicting the total strength of 2.1 above 2 MeV. A more precise nature of those states remains to be clarified using our data analysis procedure. An examination of how sensitive these high energy states are to each of the theoretical parameters could

give hints on the nature of those states (collective, particle-hole, ...).

A non-resolved doublet of 1238-keV and 1248-keV transitions is the most intense peak in our spectra with a total cross section of 28(4) mb. The summed spectroscopic strength present in this peak does not agree with any theory prediction. We cannot exclude the hypothesis of a strong intruder contribution in this peak as of yet. A momentum study of this peak could also exclude or support this hypothesis by verifying whether the knocked-out neutron momentum distribution is compatible with a $L = 4$ neutron.

During the HiCARI campaign, three other reaction channels were studied to further characterise the collectivity in the region: (i) Coulomb excitation of ^{82}Ge and ^{84}Ge that will determine the $B(E2; 4^+ \rightarrow 2^+)$ and $B(E2; 2^+ \rightarrow 0^+)$ transition probabilities and the corresponding 4^+ and 2^+ lifetimes, (ii) the proton knockout reaction ^{83}Ga(Be, X)^{82}Zn investigating the presence of a second band (0_2^+, 2_2^+) at low energy in ^{82}Zn, (iii) the low-statistics neutron knockout reaction ^{82}Zn(Be, X)^{81}Zn aiming at a direct study of intruder states at N=51 close to ^{79}Ni.

Additionally, future experiments such as the ^{82}Ge(d, p)^{83}Ge transfer reaction could be of interest to study single-particle states above $N = 50$ (in complement to previous results [82]). For example, one of the $7/2^+$ states predicted at 1462 keV by LSSM calculations with the PFSDG-U interaction is expected to have a significant $\nu(g_{7/2})^{+1}$ component, which could indicate the lowering of the $g_{7/2}$ orbital away from stability. This study should become possible at second generation ISOL facilities, such as SPES with the new silicon array GRIT and the AGATA setup, well suited to detect particle-γ coincidences in transfer reactions.

The remaining analysis of existing data, and future developments will provide a much clearer characterisation of shape coexistence and intruder configurations in the ^{78}Ni region.

Appendix A

Optical corrections results in F7 and F9

As a complementary information to the example given in the main content in figure 3.12, we present in figure A.1 and figure A.2 the results of the correction of the dependencies of the mass-to-charge ratio A/Q on kinematic variables X and A in F7 and F9.

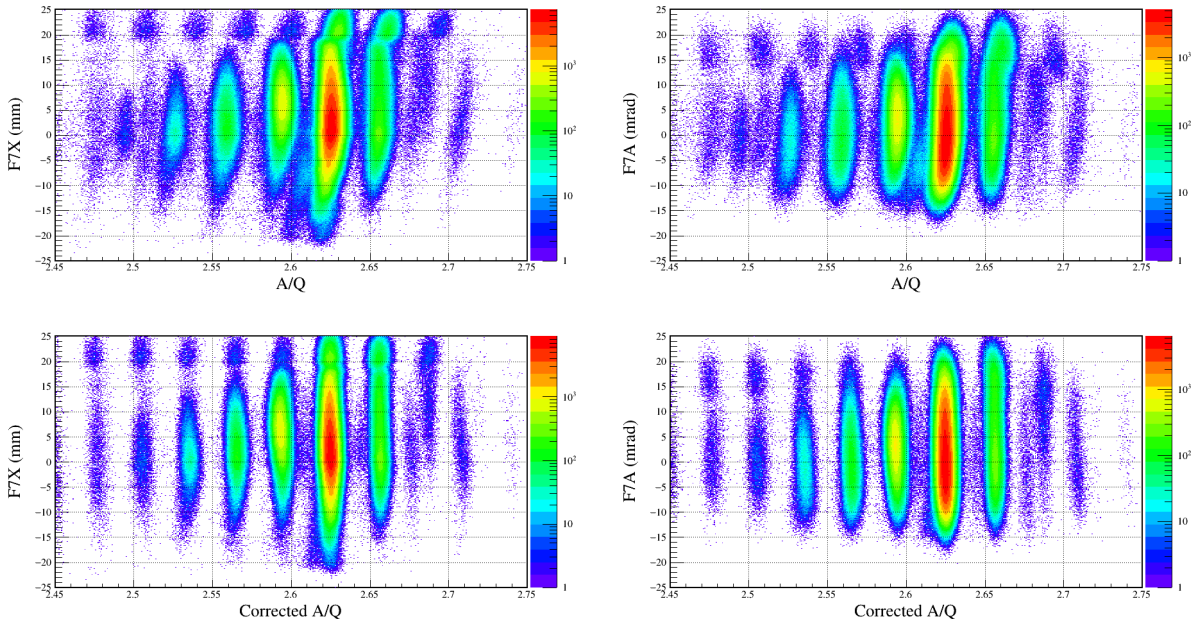

Figure A.1 – Optical correction of the dependencies between the A/Q measured in BigRIPS and the position X and angle A measured in F7. On top before correction, A/Q and kinematic variables in F7 are not independent. On the bottom after correction, most of the dependency is corrected for.

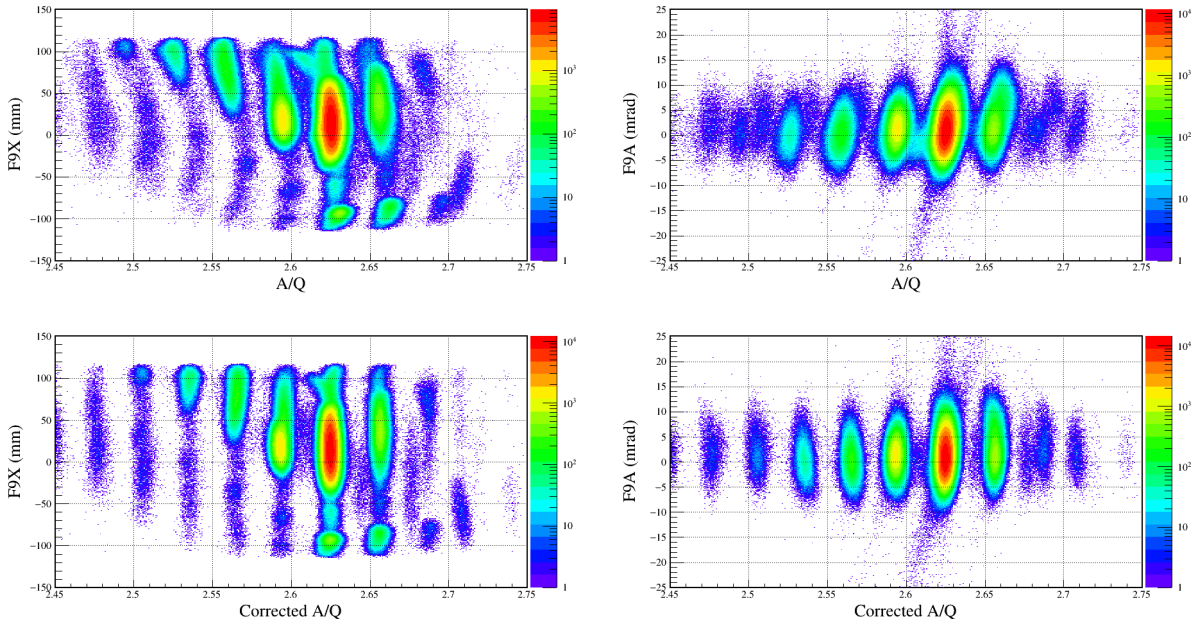

Figure A.2 – Optical correction of the dependencies between the A/Q measured in ZeroDegree and the position X and angle A measured in F9. On top before correction, A/Q and kinematic variables in F9 are not independent. On the bottom after correction, most of the dependency is corrected for.

Appendix B

Details on the HiCARI efficiency

In table B.1 we present, for each group of detectors, the parameters resulting from the fit of the experimental efficiency data points with the function defined by equation 3.13.

	a	b	c	d
MINIBALL	0.2265	-0.4479	167.6	-3.013
SuperClover	0.1607	-0.4399	139.8	-3.960
GRETINA Quad	0.0761	-0.4299	145.3	-3.068

Table B.1 – Parameters of the efficiency function (equation 3.13) fitted and presented in figure 3.18.

In table B.2 a summary of the number of crystal used in the analysis is presented. The last column briefly describes the reason for the discarded crystals.

Cluster ID number	Type	Crystals in the analysis	Remark
0	MINIBALL	0	Crystals #0 and #1 have unreasonably high thresholds, crystal #2 not functioning
1	MINIBALL	2	Crystal #0 not functioning
2	MINIBALL	3	
3	MINIBALL	2	Doubled peaks observed in crystal #0
4	MINIBALL	3	
5	MINIBALL	3	
6	SuperClover	4	
7	SuperClover	4	
8	SuperClover	3	Doubled peaks observed in crystal #2
9	SuperClover	3	Doubled peaks observed in crystal #3
10	GRETINA Quad	2	Crystal #1 has unreasonably large resolution, online decomposition of crystal #3 did not function
11	P3	0	Online decomposition not performed, and is to be done offline.

Table B.2 – Number of crystal used in each cluster and in the last column the reason for the unused crystals.

Bibliography

[1] W. Elsasser. "Sur le principe de Pauli dans les noyaux". In: *J. Phys. Radium* 4 (1933), pp. 549–556. DOI: 10.1051/jphysrad:01933004010054900. URL: https://jphysrad.journaldephysique.org/articles/jphysrad/abs/1933/10/jphysrad_1933__4_10_549_0/jphysrad_1933__4_10_549_0.html.

[2] K. Guggenheimer. "Remarques sur la constitution des noyaux atomiques - I." In: *J. Phys. Radium* 5.6 (1934), pp. 253–256. DOI: 10.1051/jphysrad:0193400506025300. URL: https://hal.science/jpa-00233232.

[3] C. Delafosse. "Study of neutron monopole drifts towards ^{78}Ni by gamma spectroscopie with BEDO at ALTO and AGATA at GANIL". Theses. Université Paris-Saclay, July 2018. URL: https://tel.archives-ouvertes.fr/tel-01848718.

[4] B. N. laboratory. *National Nuclear Data Center*. URL: www.nndc.bnl.gov (visited on 02/13/2020).

[5] M. G. Mayer. "On Closed Shells in Nuclei. II". In: *Phys. Rev.* 75 (12 June 1949), pp. 1969–1970. DOI: 10.1103/PhysRev.75.1969. URL: https://link.aps.org/doi/10.1103/PhysRev.75.1969.

[6] L. Olivier. "Nuclear structure in the vicinity of ^{78}Ni : in-beam gamma-ray spectroscopy of ^{79}Cu through proton knockout". Theses. Université Paris-Saclay, Sept. 2017. URL: https://tel.archives-ouvertes.fr/tel-01637435.

[7] D. Guillemaud-Mueller et al. "Beta -decay schemes of very neutron-rich sodium isotopes and their descendants". In: *Nuclear Physics A* 426 (1984), pp. 37–76. URL: http://hal.in2p3.fr/in2p3-00001393.

[8] D. Verney. "Etude de l'effet de couche N=50 en direction de ^{78}Ni : contribution des études de radioactivité auprèsdu séparateur en ligne PARRNe". Habilitation à diriger des recherches. Institut de Physique Nucléaire d'orsay, Université paris-sud XI, Nov. 2013. URL: https://tel.archives-ouvertes.fr/tel-01376570.

[9] O. Sorlin and M. Porquet. "Evolution of the N = 28 shell closure: A test bench for nuclear forces". In: *Physica Scripta Volume T* T152 (Sept. 2012). DOI: 10.1088/0031-8949/2013/T152/014003.

[10] F. Nowacki and A. Poves. "New effective interaction for $0\hbar\omega$ shell-model calculations in the $sd-pf$ valence space". In: *Phys. Rev. C* 79 (1 Jan. 2009), p. 014310. DOI: 10.1103/PhysRevC.79.014310. URL: https://link.aps.org/doi/10.1103/PhysRevC.79.014310.

[11] N. Smirnova. *Shell Structure Evolution and Effective In-Medium NN Interaction.* École Joliot-Curie. Sept. 2009.

[12] T. Otsuka et al. "Evolution of shell structure in exotic nuclei". In: *Rev. Mod. Phys.* 92 (1 Mar. 2020), p. 015002. DOI: 10.1103/RevModPhys.92.015002. URL: https://link.aps.org/doi/10.1103/RevModPhys.92.015002.

[13] F. Nowacki, A. Obertelli, and A. Poves. "The neutron-rich edge of the nuclear landscape: Experiment and theory." In: *Progress in Particle and Nuclear Physics* 120 (2021), p. 103866. ISSN: 0146-6410. DOI: https://doi.org/10.1016/j.ppnp.2021.103866. URL: https://www.sciencedirect.com/science/article/pii/S014664102100020X.

[14] K. Heyde and J. L. Wood. "Shape coexistence in atomic nuclei". In: *Rev. Mod. Phys.* 83 (4 Nov. 2011), pp. 1467–1521. DOI: 10.1103/RevModPhys.83.1467. URL: https://link.aps.org/doi/10.1103/RevModPhys.83.1467.

[15] C. Wraith et al. "Evolution of nuclear structure in neutron-rich odd-Zn isotopes and isomers". In: *Physics Letters B* 771 (2017), pp. 385–391. ISSN: 0370-2693. DOI: https://doi.org/10.1016/j.physletb.2017.05.085. URL: http://www.sciencedirect.com/science/article/pii/S0370269317304483.

[16] R. Taniuchi et al. "^{78}Ni revealed as a doubly magic stronghold against nuclear deformation". In: *Nature* 569 (May 2019), p. 53. DOI: 10.1038/s41586-019-1155-x.

[17] C. Santamaria et al. "Extension of the $N = 40$ Island of Inversion towards $N = 50$: Spectroscopy of ^{66}Cr, ^{70,72}Fe". In: *Phys. Rev. Lett.* 115 (19 Nov. 2015), p. 192501. DOI: 10.1103/PhysRevLett.115.192501. URL: https://link.aps.org/doi/10.1103/PhysRevLett.115.192501.

[18] F. Nowacki et al. "Shape Coexistence in ^{78}Ni as the Portal to the Fifth Island of Inversion". In: *Phys. Rev. Lett.* 117 (27 Dec. 2016), p. 272501. DOI: 10.1103/PhysRevLett.117.272501. URL: https://link.aps.org/doi/10.1103/PhysRevLett.117.272501.

[19] G. Hagen, G. R. Jansen, and T. Papenbrock. "Structure of ^{78}Ni from First-Principles Computations". In: *Phys. Rev. Lett.* 117 (17 Oct. 2016), p. 172501. DOI: 10.1103/PhysRevLett.117.172501. URL: https://link.aps.org/doi/10.1103/PhysRevLett.117.172501.

[20] L. Nies et al. "Further Evidence for Shape Coexistence in ^{79}Zn^{m} near Doubly Magic ^{78}Ni". In: *Phys. Rev. Lett.* 131 (22 Nov. 2023), p. 222503. DOI: 10.1103/PhysRevLett.131.222503. URL: https://link.aps.org/doi/10.1103/PhysRevLett.131.222503.

[21] F. Flavigny and M. Gorska. "Neutron intruder states and collectivity beyond N=50 towards ^{78}Ni". Slides for the RIKEN-RIBF 20th NP-PAC meeting. Dec. 2019.

[22] X. Yang et al. "Isomer shift and magnetic moment of the long-lived $1/2^+$ isomer in $^{79}_{30}$Zn$_{49}$: signature of shape coexistence near ^{78}Ni". In: *Physical Review Letters* 116 (Apr. 2016). DOI: 10.1103/PhysRevLett.116.182502.

[23] S. Ahn et al. "Direct neutron capture cross section on ^{80}Ge and probing shape coexistence in neutron-rich nuclei". In: *Phys. Rev. C* 100 (4 Oct. 2019), p. 044613. DOI: 10.1103/PhysRevC.100.044613. URL: https://link.aps.org/doi/10.1103/PhysRevC.100.044613.

[24] A. Gottardo et al. "First Evidence of Shape Coexistence in the ^{78}Ni Region: Intruder 0_2^+ State in ^{80}Ge". In: *Phys. Rev. Lett.* 116 (18 May 2016), p. 182501. DOI: 10.1103/PhysRevLett.116.182501. URL: https://link.aps.org/doi/10.1103/PhysRevLett.116.182501.

[25] F. H. Garcia et al. "Absence of Low-Energy Shape Coexistence in ^{80}Ge: The Nonobservation of a Proposed Excited 0_2^+ Level at 639 keV". In: *Phys. Rev. Lett.* 125 (17 Oct. 2020), p. 172501. DOI: 10.1103/PhysRevLett.125.172501. URL: https://link.aps.org/doi/10.1103/PhysRevLett.125.172501.

[26] S. Sekal et al. "Low-spin states in ^{80}Ge populated in the β decay of the ^{80}Ga 3^- isomer". In: *Phys. Rev. C* 104 (2 Aug. 2021), p. 024317. DOI: 10.1103/PhysRevC.104.024317. URL: https://link.aps.org/doi/10.1103/PhysRevC.104.024317.

[27] J. Dudouet et al. "Excitations of the magic $N = 50$ neutron-core revealed in ^{81}Ga". In: *Phys. Rev. C* 100 (1 July 2019), p. 011301. DOI: 10.1103/PhysRevC.100.011301. URL: https://link.aps.org/doi/10.1103/PhysRevC.100.011301.

[28] C. Delafosse et al. "Pseudospin Symmetry and Microscopic Origin of Shape Coexistence in the ^{78}Ni Region: A Hint from Lifetime Measurements". In: *Phys. Rev. Lett.* 121 (19 Nov. 2018), p. 192502. DOI: 10.1103/PhysRevLett.121.192502. URL: https://link.aps.org/doi/10.1103/PhysRevLett.121.192502.

[29] K. Rezynkina et al. "Structure of ^{83}As, ^{85}As, and ^{87}As: From semimagicity to γ softness". In: *Phys. Rev. C* 106 (1 July 2022), p. 014320. DOI: 10.1103/PhysRevC.106.014320. URL: https://link.aps.org/doi/10.1103/PhysRevC.106.014320.

[30] K. Heyde, M. Waroquier, and R. A. Meyer. "Unified description of odd-mass indium nuclei I. General theory and comparison to ^{113}In and ^{115}In levels populated in the decay of ^{113}Sn and ^{115}Cd^{m,g}". In: *Phys. Rev. C* 17 (3 Mar. 1978), pp. 1219–1243. DOI: 10.1103/PhysRevC.17.1219. URL: https://link.aps.org/doi/10.1103/PhysRevC.17.1219.

[31] F. Flavigny and M. Gorska. "Neutron intruder states and collectivity beyond N=50 towards ^{78}Ni". Note for the RIKEN-RIBF 20th NP-PAC meeting. Dec. 2019.

[32] A. Mueller. "AN OVERVIEW OF RADIOACTIVE BEAM FACILITIES". In: *7th European Particle Accelerator Conference*. June 2000. URL: https://accelconf.web.cern.ch/e00/PAPERS/TUZF201.pdf.

[33] Y. Blumenfeld, T. Nilsson, and P. V. Duppen. "Facilities and methods for radioactive ion beam production". In: *Physica Scripta* 2013.T152 (Jan. 2013), p. 014023. DOI: 10.1088/0031-8949/2013/T152/014023. URL: https://dx.doi.org/10.1088/0031-8949/2013/T152/014023.

[34] J. Cornell. "Radioactive beam facilities in Europe: current status and future development". In: *17th International Conference on Cyclotrons and their Applications*. 5 pages, 12 figures, to be appear in the proceedings of the 17th International Conference on Cyclotrons and their Applications. Tokyo, Japan, Oct. 2004, pp. 1–5. URL: https://hal.in2p3.fr/in2p3-00023671.

[35] H. Okuno, N. Fukunishi, and O. Kamigaito. "Progress of RIBF accelerators". In: *PTEP* 2012 (2012), p. 03C002. DOI: 10.1093/ptep/pts046.

[36] Y. Yano. "Status of the RIKEN RIB factory". In: *2007 IEEE Particle Accelerator Conference (PAC)*. 2007, pp. 700–702. DOI: 10.1109/PAC.2007.4441105.

[37] H. Ryuto et al. "Charge Stripping Plan of the RIKEN RI-beam factory". In: (Jan. 2004).

[38] N. Inabe et al. "Fixed-Frequency Ring Cyclotron (fRC) in RIBF". In: (2005). URL: https://cds.cern.ch/record/930763.

[39] K.-H. Schmidt et al. "The momentum-loss achromat — A new method for the isotopical separation of relativistic heavy ions". In: *Nuclear Instruments and Methods in Physics Research Section A: Accelerators, Spectrometers, Detectors and Associated Equipment* 260.2 (1987), pp. 287–303. ISSN: 0168-9002. DOI: https://doi.org/10.1016/0168-9002(87)90092-1. URL: https://www.sciencedirect.com/science/article/pii/0168900287900921.

[40] J. Dufour et al. "Projectile fragments isotopic separation: Application to the LISE spectrometer at GANIL". In: *Nuclear Instruments and Methods in Physics Research Section A: Accelerators, Spectrometers, Detectors and Associated Equipment* 248.2 (1986), pp. 267–281. ISSN: 0168-9002. DOI: https://doi.org/10.1016/0168-9002(86)91008-9. URL: https://www.sciencedirect.com/science/article/pii/0168900286910089.

[41] N. Fukuda et al. "Identification and separation of radioactive isotope beams by the BigRIPS separator at the RIKEN RI Beam Factory". In: *Nuclear Instruments and Methods in Physics Research Section B: Beam Interactions with Materials and Atoms* 317 (2013). XVIth International Conference on ElectroMagnetic Isotope Separators and Techniques Related to their Applications, December 2–7, 2012 at Matsue, Japan, pp. 323–332. ISSN: 0168-583X. DOI: https://doi.org/10.1016/j.nimb.2013.08.048. URL: https://www.sciencedirect.com/science/article/pii/S0168583X13009890.

[42] W. Mittig. *Spectromètres magnétiques et électriques comme détecteurs de haute résolution et comme filtres sélectifs*. École Joliot-Curie. 1994.

[43] H. Kumagai et al. "Development of Parallel Plate Avalanche Counter (PPAC) for BigRIPS fragment separator". In: *Nucl. Instrum. Meth. B* 317 (2013). Ed. by H. Sakurai et al., pp. 717–727. DOI: 10.1016/j.nimb.2013.08.050. arXiv: 1311.0215 [physics.ins-det].

[44] N. Paul. "First spectroscopy of ^{110}Zr with MINOS". PhD thesis. Institut de Recherches sur les lois Fondamentales de l'Univers, France, 2018.

[45] K. Kimura et al. "High-rate particle identification of high-energy heavy ions using a tilted electrode gas ionization chamber". In: *Nuclear Instruments and Methods in Physics Research Section A: Accelerators, Spectrometers, Detectors and Associated Equipment* 538.1 (2005), pp. 608–614. ISSN: 0168-9002. DOI: https://doi.org/10.1016/j.nima.2004.08.100. URL: https://www.sciencedirect.com/science/article/pii/S0168900204019953.

[46] P. Carnelli et al. "Multi-Sampling Ionization Chamber (MUSIC) for measurements of fusion reactions with radioactive beams". In: *Nuclear Instruments and Methods in Physics Research Section A: Accelerators, Spectrometers, Detectors and Associated Equipment* 799 (2015), pp. 197–202. ISSN: 0168-9002. DOI: https://doi.org/10.1016/j.nima.2015.07.030. URL: https://www.sciencedirect.com/science/article/pii/S0168900215008591.

[47] S. Takeuchi et al. “DALI2: A NaI(Tl) detector array for measurements of rays from fast nuclei”. In: *Nuclear Instruments and Methods in Physics Research Section A: Accelerators, Spectrometers, Detectors and Associated Equipment* 763 (2014), pp. 596–603. ISSN: 0168-9002. DOI: https://doi.org/10.1016/j.nima.2014.06.087. URL: https://www.sciencedirect.com/science/article/pii/S0168900214008419.

[48] C. Santamaria. “Quest for new nuclear magic numbers with MINOS”. Theses. Université Paris Sud - Paris XI, Sept. 2015. URL: https://tel.archives-ouvertes.fr/tel-01231191.

[49] J. Eberth et al. “MINIBALL A Ge detector array for radioactive ion beam facilities”. In: *Progress in Particle and Nuclear Physics* 46.1 (2001), pp. 389–398. ISSN: 0146-6410. DOI: https://doi.org/10.1016/S0146-6410(01)00145-4. URL: https://www.sciencedirect.com/science/article/pii/S0146641001001454.

[50] G. de France et al. “EXOGAM at the ILL: the EXILL campaign”. In: *Journal of Physics: Conference Series* 966 (Feb. 2018), p. 012012. DOI: 10.1088/1742-6596/966/1/012012.

[51] S. Paschalis et al. “The performance of the Gamma-Ray Energy Tracking In-beam Nuclear Array GRETINA”. English. In: *Nuclear instruments and methods in physics research section a-Accelerators spectrometers detectors and associated equipment* 709 (2013), pp. 44–55. ISSN: 0168-9002. DOI: 10.1016/j.nima.2013.01.009.

[52] V. T. Jordanov and G. F. Knoll. “Digital synthesis of pulse shapes in real time for high resolution radiation spectroscopy”. In: *Nuclear Instruments and Methods in Physics Research Section A: Accelerators, Spectrometers, Detectors and Associated Equipment* 345.2 (1994), pp. 337–345. ISSN: 0168-9002. DOI: https://doi.org/10.1016/0168-9002(94)91011-1. URL: https://www.sciencedirect.com/science/article/pii/0168900294910111.

[53] D. Radford. *The GRETINA Signal Decomposition Algorithm*. 2016. URL: https://indico.in2p3.fr/event/13409/contributions/14197/attachments/11814/14540/Radford_decomp_Dec2016.pdf.

[54] A. Korichi and T. Lauritsen. “Tracking gamma rays in highly segmented HPGe detectors: A review of AGATA and GRETINA”. In: *The European Physical Journal A* 55 (July 2019). Accepted: 29 May 2019 Published: 29 July 2019, p. 121. ISSN: 1434-6001. DOI: 10.1140/epja/i2019-12787-1. URL: http://link.springer.com/10.1140/epja/i2019-12787-1.

[55] J. T. Anderson et al. "Data acquisition and trigger system of the Gamma Ray Energy Tracking In-Beam Nuclear Array (GRETINA)". In: *2007 IEEE Nuclear Science Symposium Conference Record*. Vol. 3. 2007, pp. 1751–1756. DOI: 10.1109/NSSMIC.2007.4436499.

[56] F. Rademakers et al. *root-project/root: v6.20/06*. Version v6-20-06. June 2020. DOI: 10.5281/zenodo.3895852. URL: https://doi.org/10.5281/zenodo.3895852.

[57] G. F. Knoll. *Radiation detection and measurement / Glenn F. Knoll*. English. 2nd ed. Wiley New York, 1989, xix, 754 p. : ISBN: 0471815047.

[58] N. Abgrall et al. "ADC Nonlinearity Correction for the Majorana Demonstrator". In: *IEEE Trans. Nucl. Sci.* 68.3 (2021), pp. 359–367. DOI: 10.1109/TNS.2020.3043671. arXiv: 2003.04128 [physics.ins-det].

[59] S. Collaboration. *Source activities*. URL: https://www.nishina.riken.jp/collaboration/SUNFLOWER/misc/util/sources.php.

[60] A. Svec. "Analytical efficiency curve for coaxial germanium detectors". In: *Applied Radiation and Isotopes* 66 (Feb. 2008), pp. 786–791.

[61] L. Riley et al. "UCGRETINA geant4 simulation of the GRETINA Gamma-Ray Energy Tracking Array". In: *Nuclear Instruments and Methods in Physics Research Section A: Accelerators, Spectrometers, Detectors and Associated Equipment* 1003 (2021), p. 165305. ISSN: 0168-9002. DOI: https://doi.org/10.1016/j.nima.2021.165305. URL: https://www.sciencedirect.com/science/article/pii/S0168900221002898.

[62] D. Testov et al. "The 3He long-counter TETRA at the ALTO ISOL facility". In: *Nuclear Instruments and Methods in Physics Research Section A: Accelerators, Spectrometers, Detectors and Associated Equipment* 815 (2016), pp. 96–103. ISSN: 0168-9002. DOI: https://doi.org/10.1016/j.nima.2015.11.150. URL: https://www.sciencedirect.com/science/article/pii/S0168900215015697.

[63] M. F. Alshudifat et al. "Reexamining Gamow-Teller decays near ^{78}Ni". In: *Phys. Rev. C* 93 (4 Apr. 2016), p. 044325. DOI: 10.1103/PhysRevC.93.044325. URL: https://link.aps.org/doi/10.1103/PhysRevC.93.044325.

[64] J. A. Winger et al. "New subshell closure at $N = 58$ emerging in neutron-rich nuclei beyond ^{78}Ni". In: *Phys. Rev. C* 81 (4 Apr. 2010), p. 044303. DOI: 10.1103/PhysRevC.81.044303. URL: https://link.aps.org/doi/10.1103/PhysRevC.81.044303.

[65] A. Gade et al. "Collectivity at $N = 50$: ^{82}Ge and ^{84}Se". In: *Phys. Rev. C* 81 (6 June 2010), p. 064326. DOI: 10.1103/PhysRevC.81.064326. URL: https://link.aps.org/doi/10.1103/PhysRevC.81.064326.

[66] E. Sahin et al. "Structure of the N=50 As, Ge, Ga nuclei". In: *Nuclear Physics A* 893 (2012), pp. 1–12. ISSN: 0375-9474. DOI: https://doi.org/10.1016/j.nuclphysa.2012.08.007. URL: https://www.sciencedirect.com/science/article/pii/S0375947412002412.

[67] Y. Shiga et al. "Investigating nuclear shell structure in the vicinity of ^{78}Ni: Low-lying excited states in the neutron-rich isotopes ^{80,82}Zn". In: *Phys. Rev. C* 93 (2 Feb. 2016), p. 024320. DOI: 10.1103/PhysRevC.93.024320. URL: https://link.aps.org/doi/10.1103/PhysRevC.93.024320.

[68] D. Thisse et al. "Study of $N = 50$ gap evolution around $Z = 32$: new structure information for ^{82}Ge". In: *Eur. Phys. J. A* 59.7 (2023), p. 153. DOI: 10.1140/epja/s10050-023-01051-2.

[69] D. Thisse. "Étude des états particule-trou dans les noyaux de la région du Ni avec le spectromètre -Ball". 2021UPASP081. PhD thesis. 2021. URL: http://www.theses.fr/2021UPASP081/document.

[70] S. Chen et al. "Low-lying structure and shape evolution in neutron-rich Se isotopes". In: *Phys. Rev. C* 95 (4 Apr. 2017), p. 041302. DOI: 10.1103/PhysRevC.95.041302. URL: https://link.aps.org/doi/10.1103/PhysRevC.95.041302.

[71] M. Lettmann et al. "Triaxiality of neutron-rich ^{84,86,88}Ge from low-energy nuclear spectra". In: *Phys. Rev. C* 96 (1 July 2017), p. 011301. DOI: 10.1103/PhysRevC.96.011301. URL: https://link.aps.org/doi/10.1103/PhysRevC.96.011301.

[72] C. Shand et al. "Shell evolution beyond Z=28 and N=50: Spectroscopy of 81,82,83,84Zn". In: *Physics Letters B* 773 (2017), pp. 492–497. ISSN: 0370-2693. DOI: https://doi.org/10.1016/j.physletb.2017.09.001. URL: https://www.sciencedirect.com/science/article/pii/S0370269317306998.

[73] F. Flavigny et al. "Shape Evolution in Neutron-Rich Krypton Isotopes Beyond $N = 60$: First Spectroscopy of ^{98,100}Kr". In: *Phys. Rev. Lett.* 118 (24 June 2017), p. 242501. DOI: 10.1103/PhysRevLett.118.242501. URL: https://link.aps.org/doi/10.1103/PhysRevLett.118.242501.

[74] S. Iwazaki and N. Aoi. Collaboration meetings. June 3, 2021.

[75] R. Crane. Collaboration meetings. Dec. 14, 2022.

[76] D. Verney et al. "Pygmy Gamow-Teller resonance in the $N = 50$ region: New evidence from staggering of β-delayed neutron-emission probabilities". In: *Phys. Rev. C* 95 (5 May 2017), p. 054320. DOI: 10.1103/PhysRevC.95.054320. URL: https://link.aps.org/doi/10.1103/PhysRevC.95.054320.

[77] J. A. Winger et al. "New subshell closure at $N = 58$ emerging in neutron-rich nuclei beyond ^{78}Ni". In: *Phys. Rev. C* 81 (4 Apr. 2010), p. 044303. DOI: 10.1103/PhysRevC.81.044303. URL: https://link.aps.org/doi/10.1103/PhysRevC.81.044303.

[78] D. Jackson. *Nuclear Reactions*. Science paperbacks. John Wiley & Sons, Incorporated, 1975. ISBN: 9780470431863. URL: https://books.google.se/books?id=gKuIPwAACAAJ.

[79] P. Hansen and J. Tostevin. "DIRECT REACTIONS WITH EXOTIC NUCLEI". In: *Annual Review of Nuclear and Particle Science* 53.1 (2003), pp. 219–261. DOI: 10.1146/annurev.nucl.53.041002.110406. eprint: https://doi.org/10.1146/annurev.nucl.53.041002.110406. URL: https://doi.org/10.1146/annurev.nucl.53.041002.110406.

[80] Y. Tsunoda et al. "Novel shape evolution in exotic Ni isotopes and configuration-dependent shell structure". In: *Phys. Rev. C* 89 (3 Mar. 2014), p. 031301. DOI: 10.1103/PhysRevC.89.031301. URL: https://link.aps.org/doi/10.1103/PhysRevC.89.031301.

[81] M.-C. Delattre. "Étude de la structure à basse énergie de Zn par décroissance et -n de Cu et Cu". 2016SACLS369. PhD thesis. 2016. URL: http://www.theses.fr/2016SACLS369/document.

[82] J. S. Thomas et al. "Single-neutron excitations in neutron-rich ^{83}Ge and ^{85}Se". In: *Phys. Rev. C* 76 (4 Oct. 2007), p. 044302. DOI: 10.1103/PhysRevC.76.044302. URL: https://link.aps.org/doi/10.1103/PhysRevC.76.044302.

Intruder states and shape coexistence beyond N=50 close to ^{78}Ni studied by neutron knockout at RIBF-RIKEN

Abstract

The recent spectroscopy of ^{78}Ni together with indications of shape coexistence just below the N=50 shell closure for ^{79}Zn suggests that deformed intruder configurations could play a crucial role in low-energy structure properties in this region and towards the limits of the nuclear chart. Such configurations are predicted to originate from multiparticle-multihole excitations above the N=50 and Z=28 shell gaps pushed down in energy due to neutron-proton correlations which enhance quadrupole collectivity. Because these intruder states involve many-particle excitations more difficult to describe theoretically, their predicted energies vary more drastically between models than for yrast states originating from "normal" configurations on which they tend to agree.

This topic is the main goal of the experiment performed at the RIBF facility (RIKEN, Japan) in November 2020 to identify and characterise for the first time 2p-1h intruder states in ^{83}Ge. Neutron hole states in this N=51 nucleus were populated via neutron knockout reaction from the N=52 nucleus ^{84}Ge that has about two neutrons in the $s_{1/2}d_{5/2}$ valence space above N=50. This direct reaction allows in some cases to remove one of the neutrons from the quasi-full $g_{9/2}$ orbital below N=50 to selectively populate the $9/2^+$ intruder states based on a $\nu(g_{9/2})^{-1}(s_{1/2}d_{5/2})^{+2}$ configuration. In order to identify the populated states, gamma-rays from their in-flight decay were measured using the HiCARI Germanium array.

We are able to identify a state at 1359 keV as a 2p-1h intruder, in good agreement with phenomenological and shell model calculations. In line with predictions as well, we measure some candidate states at high energy that are still to be fully characterised. A transition at 1240 keV matches with previously identified states and was expected to come from the coupling of a neutron with the excited ^{82}Ge core. However the very high spectroscopic factor measured on this transition does not compare with any prediction and requires more development to be explained.

Résumé

La spectroscopie récente du ^{78}Ni, additionnée aux indications de coexistence de formes juste en dessous de la fermeture de couche N=50 pour le ^{79}Zn, suggère que les configurations intruses déformées pourraient jouer un rôle crucial dans les propriétés de la structure en couche à basse énergie dans la région, et aux abords de la limite du diagramme de Segré. Il est prédit que de telles configurations trouvent leurs origines dans les excitations multiparticules-multitrous au dessus des gaps N=50 et Z=28, réduits par les corrélations neutrons-protons qui renforcent la collectivité quadrupolaire. Ces états impliquant de multiples excitations particules-trous difficiles à décrire de manière théorique, les énergies prédites varient drastiquement plus selon les modèles que pour les états yrast provenant de configurations "normales" pour lesquelles ils tendent à être en accord.

Ce sujet est l'objectif principal de l'expérience effectuée en novembre 2020 à l'installation RIBF (RIKEN, Japon) pour identifier et caractériser pour la première fois des états intrus 2p-1t dans le ^{83}Ge. Les états trous neutrons dans ce noyau à N=51 ont été peuplés par une réaction d'arrachage de neutron depuis le noyau à N=52 ^{84}Ge possédant environ deux neutrons dans l'espace de valence $s_{1/2}d_{5/2}$ au dessus de N=50. Cette réaction directe permet dans certains cas de retirer un neutron de l'orbitale quasi-pleine $g_{9/2}$ en dessous de N=50 pour peupler de manière sélective l'état intrus $9/2^+$ en se basant sur une configuration $\nu(g_{9/2})^{-1}(s_{1/2}d_{5/2})^{+2}$. Afin d'identifier les états peuplés, les rayons gammas émis en vol sont mesurés à l'aide du multi-détecteur au Germanium HiCARI.

Nous identifions un état à 1359 keV comme un intrus 2p-1t, en bon accord avec les prédictions de phénoménologie et de calculs de modèle en couches. Aussi en accords avec les prédictions, nous mesurons des états intrus candidats à haute énergie nécessitant encore d'être totalement caractérisés. Une transition à 1240 keV correspond avec des états précédemment identifiés et il était anticipé qu'elle provienne du couplage d'un neutron avec le coeur excité de ^{82}Ge. Cependant le facteur spectroscopique très élevé mesuré pour cette transition est incomparable avec les prédictions théoriques et requiert plus de développement pour être expliqué.

Keywords— Nuclear structure, Exotic Nuclei, Shell Model, Secondary beams, Gamma spectroscopy, Germanium detectors, HiCARI, RIBF, Knockout reactions, 83Ge, Intruder states, Shape coexistence, Magic numbers, N=50.